ALMA MATER STUDIORUM - UNIVERSITÀ DI BOLOGNA

Scuola di Scienze
Dipartimento di Fisica e Astronomia

Master's degree in Physics

Particle Therapy: nuclear fragmentation study at the FOOT experiment

Thesis Advisor:
Prof. Mauro Villa
Research Supervisor:
Dott.ssa Sofia Colombi

Candidate:
Annamaria Rotondo

Academic Year 2020-2021

Abstract

This thesis work describes the main topics of the Charged Particle Therapy (CPT) concerning treatment of deep-seated tumors, exploiting the ions characteristic distribution of energy deposition in matter and their high biological effectiveness.

In this framework, FOOT (FragmentatiOn Of Target) is an experiment of applied nuclear physics, aiming to measure nuclear fragmentation cross sections relevant in particle therapy and also space radioprotection, for which the experimental panorama is very poor. In fact, these measurements are fundamental to improve the nuclear interactions description and the nuclear models used to calculate the dose in treatment planning, described in *Chapter 1*. To this purpose, two experimental setup have been developed, and this thesis focuses on the electronics apparatus, explained in *Chapter 2*, which aims to measure $Z \geq 3$ fragments, which are emitted at small angles with respect to the primary beam direction. By measuring momentum, time of flight, kinetic energy and energy loss in thin detectors, the FOOT apparatus will determine fragments charge and mass and thus, it will allow to uniquely identify them. In this thesis, the reconstruction and the analysis of the simulated FLUKA data are described. The expected resolutions of the different FOOT detectors have been applied to Monte Carlo samples in order to recreate experimental-like data. *Chapter 3* focuses on the identification of fragments and on minimization fitting methods, which provide the best determination of the mass number, allowing to discriminate events spoiled for istance by a kinetic energy underestimation, which is mainly due to the emission of neutrons.

Contents

Introduction

Hadrontherapy is an advanced cancer treatment that uses protons and carbon ions instead of X-rays to attack tumour cells, particularly radio-resistant tumours which do not respond to the traditional radiotherapy or surgically inoperable. The advantage of using these types of particles is their dose-depth profile characterized by the Bragg peak which allows to maximize damage in the tumor region by limiting damage to neighboring healthy tissues. Until now, however, a complete estimate of the therapy side effects caused by nuclear fragmentation events between particles beam and the human body has not been completely evaluated yet.

The FOOT experiment has the aim of measuring differential cross section of all products emitted in the nuclear fragmentation, thus main topic of this thesis is the identification of these fragments generated by the interaction of the therapy beam, in particular ^{16}O with kinetic energy of 200 MeV/n, with a target of C_2H_4, simulating the hadrontherapy treatment on the human body. The atomic number Z and the number of mass A of the most produced fragments (i.e. ^{1}H, ^{4}He, ^{7}Li, ^{9}Be, ^{11}B, ^{12}C, ^{14}N, ^{16}O) have been reconstruted exploiting FLUKA simulated data and applying the detector resolution of each FOOT subdetector, obtained in several test beam. In detail, the Z has been estimated through the Time of Flight and the energy loss of the fragments by means of the Bethe-Bloch formula; the performance achieved allows a complete separation of the elements. Concerning the A evaluation, a direct method has been used which makes use of three correlated relativistic formulas, this is possible thanks to the redundant subdetectors in the FOOT apparatus; then two different fit methods, the Augmented Lagrangian and the Minimum χ^2 Method, have been applied in order to better reconstruct the A values and improve the related resolutions. The latter show better results than the direct one because in the fit cases all the subdetectors are exploited in the estimate of A. Moreover, also the time of flight, momentum and total kinetic energy parameters have been obtained through the fit methods, which can be useful for a more accurate kinematic study to be used in the fragments nuclear cross sections measurements.

Chapter 1

Hadrontherapy

1.1 Introduction

Hadrontherapy is the medical use of charged particles (protons and other ions, such as carbon), called "hadrons", hence the name of the therapy, in order to treat deep-seated solid tumors that are often surgically inoperable or resistant to traditional radiotherapy and chemotherapy treatments [2].

This new increasingly used technique is based on the particular physical and radiobiological properties of protons/ions; unlike traditional radiotherapy based on X-rays or electrons, these heavy charged particles have a favorable depth-dose profile, characterized by low energy deposition in the entrance channel, followed by a maximum energy release at a certain depth just before stopping: the Bragg Peak. This allows a precise definition of the specific region to be irradiated and therefore, as a consequence, this behavior makes it possible to spare mostly healthy tissues, with respect to conventional X-rays, while delivering the highest dose to the cancer.

The idea of using protons for cancer treatment was first proposed in 1946 by the physicist Robert Wilson, who was one of the founder of the Fermi National Accelerator Laboratory (Fermilab). The first patients were treated in the 1950s in nuclear physics research facilities. Afterwards, improvements in accelerator technology, coupled with innovative techniques in medical imaging and computing, made hadrontherapy an advantageous option for medical applications. Globally there is a huge impulse in particle therapy, especially treatment with protons. Currently there are more than 100 centres around the world (with over 30 of these in Europe), but only six facilities are capable of delivering proton and carbon ion hadrontherapy, one of them, CNAO (National Center of Oncological Hadrontherapy) Foundation, is settled at Pavia in Italy [1].

Nevertheless, research is still ongoing to further improve the accuracy of the related Treatment Planning Systems, although it is a consolidated procedure in clinical practice, because in this particular therapy we have also to consider the contribution of nuclear fragmentation processes to the beam dose profiles; while in proton therapy the short-range recoil nuclei generated in target fragmentation processes could lead to an increased dose in the entrance window, in heavy ion therapy projectile fragments generate an additional dose tail behind the Bragg Peak, so they could pass the tumor region. Therefore, it is very important to take into account this kind of behaviour inside the patient's body in order to plan the right treatment.

However, it is difficult to exactly evaluate the contribution of these fragmentation products to total dose distributions because of the lack of experimental cross section data of the fragments in the energy range of the hadrontherapy. For this purpose, there are several experiments proposing different ways to definitively fill this data lack in the future and improve our knowledge in this field.

1.2 Interaction of charged particles with matter

When a charged particle travels through an absorbing medium, it is subject to various types of interactions. In the energy range of the hadrontherapy (up to 250 MeV for protons and up to 400 MeV/u for ^{12}C ions), the behavior of heavy charged particles (i.e. with mass much greater than electron) can be accurately described considering 3 main processes:

- Inelastic collisions with atomic electrons, which lead to energy loss and determine particles longitudinal energy deposition profile and range.
- Elastic scattering with nuclei of the medium, or Multiple Coulomb Scattering, which is the main responsible for the lateral spread of the beam around the longitudinal direction.
- Nuclear interactions with the material: both elastic or inelastic collisions between projectile and target nuclei.

The first two processes are the result of electromagnetic forces and will be explained below.

1.2.1 Electromagnetic energy loss

For a heavy charged particle, energy loss by ionization is the most commmon electromagnetic process that can happen passing through a medium. Since the nuclear cross section is extremely small compared to the atomic one: $\sigma_{atom} = 10^{10}\sigma_{nucl}$, interaction with electrons is therefore much more probable. During these interactions, electrons receive enough energy to escape the atoms of the material, which are thus ionized. Since ionization is intrinsically stochastic and occur with a certain probability, only an average value can be defined. Therefore, the mean energy loss through collisions for unit lenght of each particle with charge Z and mass M, inside an homogeneous material of density ρ_T, called the *Stopping Power* dE/dx, is given by *the Bethe-Bloch formula*[3]

$$-\left\langle \frac{dE}{dx} \right\rangle = K\frac{\rho_T Z_T}{A_T}\frac{Z^2}{\beta^2}\left[\frac{1}{2}log\left(\frac{2m_e c^2\beta^2\gamma^2 W_{max}}{I_T^2}\right) - \beta^2 - \frac{\delta}{2} - \frac{C}{Z}\right] \tag{1.1}$$

where

- K is a constant defined as $K = 4\pi r_e^2 N_A m_e c^2$, where $N_A = 6,0221 \times 10^{23}$ and r_e are respectively the Avogadro's number and the classical electron radius. Its value is 0.307075 $MeV cm^2/g$[4].

- Z_T, A_T and I_T are the atomic number, the mass number and the mean excitation potential of the absorber (target).
- $\beta = \frac{v}{c}$ is the velocity of the incident particles.
- $\gamma = \frac{1}{\sqrt{1-\beta^2}}$ is the Lorentz factor of the incident particles.
- m_e and c are the electron mass and the speed of light.
- W_{max} is the maximum energy transfer to an electron of the material with a single collision, given by

  $$W_{max} = \frac{2m_e c^2 \beta^2 \gamma^2}{1 + 2\gamma m_e/M + (m_e/M)^2}$$

  If the energy of the particle is low, i.e. $2\gamma m_e \ll M$, the expression becomes simply $W_{max} = 2m_e c^2 \beta^2 \gamma^2$. In the considered energy range this condition is always verified.
- δ represents the density correction, only significant for very high energies.
- C is the shell correction, relevant when the particle velocity is comparable with the one of orbital electrons.

The (1.1) formula has a minus sign to indicate a *loss* of energy and its validity is bound to the condition: $0.5 < \beta\gamma < 500$ and the electrons in the medium are considered at rest (stationary case). In this version of the Bethe-Bloch we can also note the density dependence, so this is the *stopping power per linear path* and it can be measured in MeV/cm. Otherwise, dividing dE/dx for the absorber density, we can obtain the energy loss as a function of *mass thickness* (ρdx), which can be measured in $MeV cm^2/g$. In this way we take into account the fact that for an higher mass thickness we have a higher number of interactions and, thus, a larger energy loss.

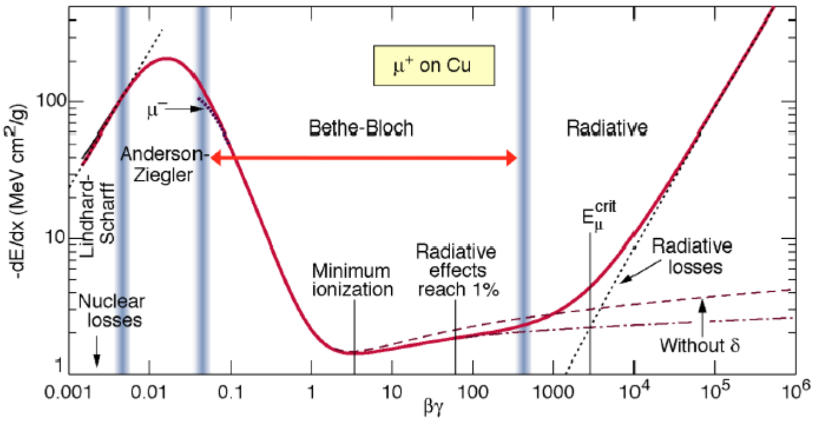

Figure 1.1: Example of mass stopping power $\left(\frac{1}{\rho_T}\frac{dE}{dx}\right)$ as a function of $\beta\gamma$ for a μ^+ beam on Cu target. [4]

As it can be seen in *Fig.1.1* , equation (1.1) has two main dependencies. The first one is approximately proportional to $1/\beta^2$, until a point called MIP (Minimum Ionizing Particle), the energy deposition has a minimum at $\beta\gamma \simeq 3$.

The second one is the logarithmic term which becomes dominant for high energies (exceeding the MIP point) and determines the relativistic rise up to the density correction plateau. The latter lowers the shape of the Bethe function and it is used in order to consider the polarization effect of the target atoms when the charged particles traversing the medium. Indeed, polarized atoms act as a shield for furthest atoms, thus, collisions with outer electrons will contribute less to the total energy loss than one predicted by the (1.1) formula. This effect becomes more important as energy increases and also depends on the density of the target, hence the name of "*density effect*", because the polarization will be greater in condensed material than in lighter one, as gases. In conclusion, for large $\beta\gamma$ value, it leads to saturation at high energy. On the other hand at very low energy, we have another correction when the velocity of the particle is comparable to the orbital velocity of the electrons and so, the stationary condition is not verified anymore and there may be capture effects, it is called the *shell correction.* Consequentially, the charge of the beam particles results partially neutralized by the electrons of the medium that bind to them. This phenomenon decreases the value of their effective charge, therefore Z must be substituted in (1.1) in order to extend the validity of Bethe's formula in the low energy region. Barkas proposes a parameterization of Z_{eff} as a function of Z and given by the following empirical expression [3]

$$Z_{eff} = Z\left(1 - e^{-125\beta Z^{-2/3}}\right) \tag{1.2}$$

Another important feature of the Bethe-Bloch is its small dependence on the atomic and mass number ratio of the absorber, for light nuclei is about 1/2, while for heavier nuclei it is approximately equal to 0.42, thus slightly smaller due to the neutrons increasing over protons.

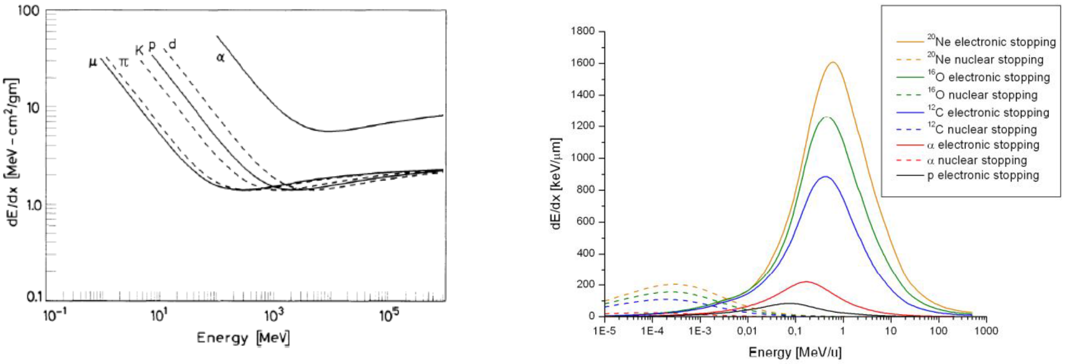

(a) **(b)**

Figure 1.2: (a) Mass stopping power as a function of the energy of the projectile for different heavy charged particles[3]. (b) Comparison of the stopping power of heavy charged particles in water [5].

The graph in *Fig.1.2(a)* shows different shapes, as a function of the energy, for particles with the same charge: this is because they can have different masses at a fixed energy but, most importantly, different β, therefore, since dE/dx depends on $1/\beta^2$, their energy loss will be different. Furthermore, for fixed energy and different charge, as the latter increases, the corresponding dE/dx will be greater due to the $\sim Z^2$ dependence.

Energy Straggling

The total energy loss ΔE in a track segment of lenght x is a stochastic quantity which means that we can obtain different values for repeated measurements with the same incident particle at the same kinetic energy beacause of statistical fluctuations. It can be expressed as [3]

$$\Delta E = \sum_{i=1}^{N} \delta E_i \tag{1.3}$$

where δE_i is the infinitesimal energy loss in a single i-th collision. Energy transfer δE_i can happen only above the *excitation threshold* and the probability is higher for smaller energy losses, so for distant collisions and decreases for low impact parameter values. The distribution is described in terms of a *straggling function* $f(\Delta/x)$[6], [7]which is not symmetrical around the *mean* energy loss (the Bethe-Bloch result), thus the latter is different from the most probable value. This phenomenon is called **energy loss straggling**. For a thin absorber or low density material the asymmetry is more evident because of few collisions, some with high energy transfer which leads to large fluctuations, represented by the Landau distribution, as in *Fig.1.3*.

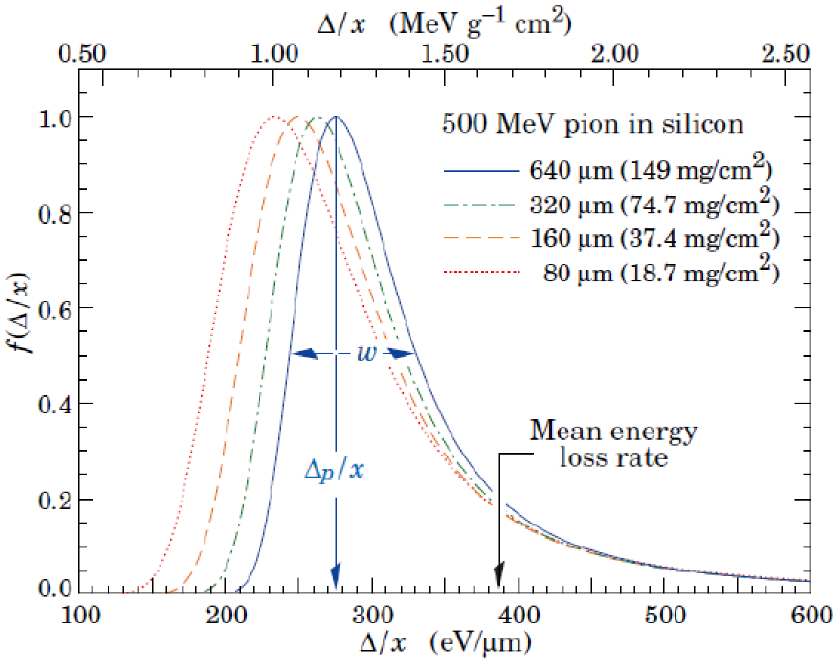

Figure 1.3: The probability distribution as a function of different thicknesses. It is slightly different from a Gaussian because of the Landau energy tail[3].

For thick or high density medium, in the limit of many interactions the straggling function can be approximated with a Gaussian model which is still quite accurate in this case[3]

$$f(\Delta E) = \frac{1}{\sqrt{2\pi\sigma_E}} exp\left(\frac{(\Delta E - < \Delta E >)^2}{2\sigma_E^2}\right) \tag{1.4}$$

with

$$\sigma_E = 4\pi Z_{eff} Z_T e^4 N \Delta x \left[\frac{1-\beta^2/2}{1-\beta^2}\right]. \tag{1.5}$$

1.2.2 Range

Heavy charged particles can only travel a finite distance inside the medium and this makes it possible to define an actual value for the range R of the beam, which represents an important parameter in hadrontherapy and, we will see, it depends on the type of material, the particle type and its energy . The most common definition of this fundamental quantity is obtained in the *Continuous-Slowing-Down Approximation (CSDA)*: it is an approximation of the effective length of the path traveled by the particle, taking into account the scattering inside the medium crossed. There is also another definition, *the Projected Range* which is the distance between the point where the particle enters the medium and the point where it is absorbed (or ends its energy), projected on the original "travel" direction. In hadrontherapy they are nearly the same thing because heavy ions are very little scattered and travel almost on a straight line, as in *Fig.1.4*.

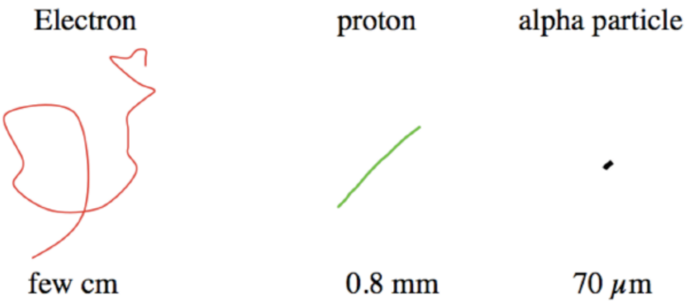

Figure 1.4: Example of different trajectories for 10 MeV charged particles. Note that the way of losing energy for the electron is different from the one described in the Bethe-Bloch. Furthemore, the track is not straight because of the dominant scattering effect against nuclei of the material[3].

Since the medium is often not homogeneous but a compound, we have also to consider various types of atoms, thus we need an approximation of the energy loss value given by *Bragg-Kleeman*, which assumes that the Mass Stopping Power for different materials is additive[**?**]knoll:knoll:

$$\left(\frac{dE}{d\chi}\right) = \sum_i w_i \left(\frac{dE}{d\chi}\right)_i \tag{1.6}$$

where w_i corresponds to the fraction of the atoms of the i-th constituent of the absorber.

Now, considering energy deposition in a portion of material dx, simply homogeneus, the range is obtainable integrating the stopping power (1.1):

$$R(E)_{CSDA} = \int_0^{L_{max}} dx = \int_{E_0}^{0} \left(\frac{dE}{dx}\right)^{-1} dE \tag{1.7}$$

with E_0, the initial kinetic energy of the beam. It is not easy to have an accurate result by integrating the Bethe-Bloch formula over all the released energy, thus there are some approximations that allow to simplify the calculation.

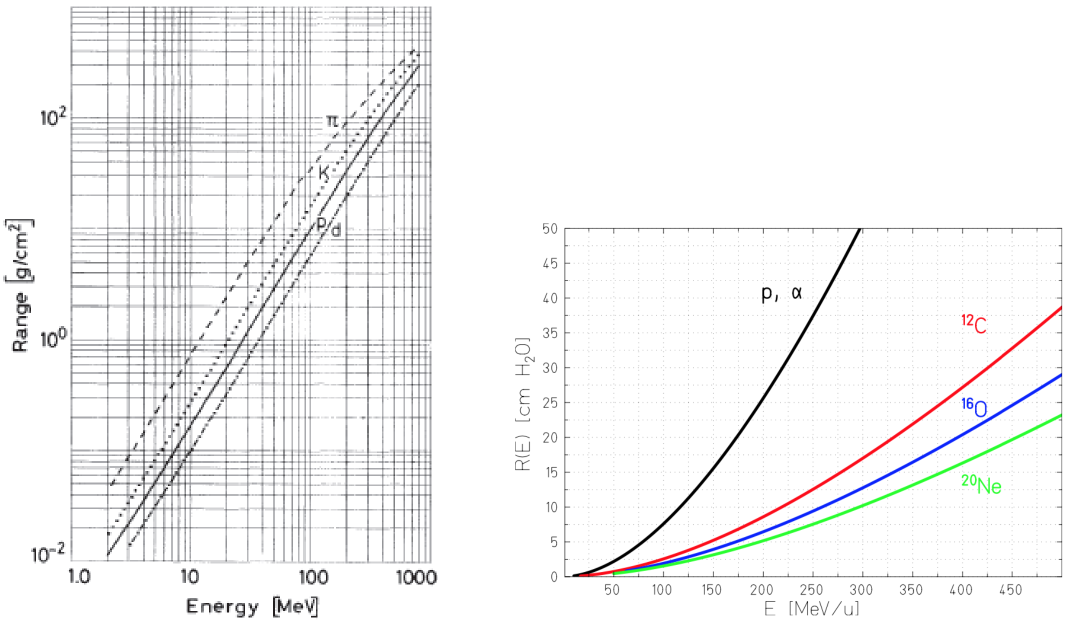

(a) **(b)**

Figure 1.5: (a) Range curves in log-log scale as a function of the initial energy of different heavy particles in aluminium [3]. (b) Mean range of heavy ions as a function of the initial energy in water[9].

Figure 1.5 (a) shows some typical range-energy curves on the log-log scale for different particles calculated by a numerical integration of the Bethe-Bloch formula. From its almost linear form, one can consider a relation of the type:

$$R \sim E^b. \tag{1.8}$$

This can also be seen from the stopping power, which at not too high energies, is dominated by the $1/\beta^2 \propto E^{-1}$ term, so from the dE/dx integration, we find[3]

$$R \propto E^2. \tag{1.9}$$

Through accurate measurements the power is actually about ~ 1.75, so it's almost proportional to the square of the initial kinetic energy. Therefore fixing this quantity, we have the possibility to know the range of the particles, this is very useful in hadrontherapy because deeper region of the human body can be reached just selecting the beam energy. A precise knowledge of the range is the main key to deliver the right amount of dose to the cancer volume while avoiding healthy tissues but this concept is further explored in Section 1.2.4 with the definition of the *Bragg Peak*.

We can also plot the transmitted fraction, i.e. the ratio between the number of particles exiting a layer of thickness x and the total number of particles hitting the absorber, as a function of the penetration depth. It should be a box function, but the real shape is shown in *Fig.1.6*.

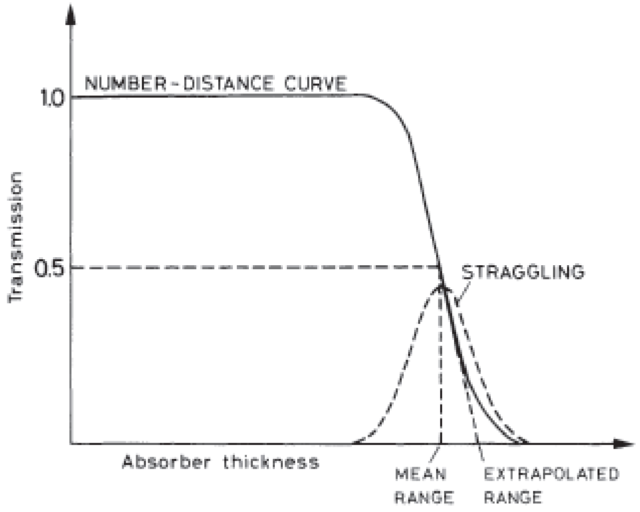

Figure 1.6: Transmission curve for an hadronic beam, showing two other possible definitions of particles range (mean and extrapolated range). The curve shows the relative intensity of the transmitted beam as a function of the thickness of the absorber.[3]

As can be seen, for small thicknesses, practically all the particles pass through the medium. However, the ratio does not drop immediately to the background level, as expected of a well defined quantity. This result is due to the fact that the energy loss is statistical in nature. Indeed, a beam of the same particles of the same kinetic energy does not imply the same release of dE. A measurement with an ensemble of identical particles, therefore, will show a statistical distribution of ranges centered about some mean value. This is known as **range straggling**. So, due to the energy loss fluctuations we have also range fluctuations which are distributed as a Gaussian in a first approximation. Its width depends on projectile and on material, the variance σ_R^2 of the range straggling is related to the variance σ_E^2 of the energy-loss straggling [9], expressed in (1.5), by

$$\sigma_R^2 = \int_{E_0}^{0} \left(\frac{d\sigma_E}{dx}\right)\left(\frac{dE}{dx}\right)^{-3} dE. \tag{1.10}$$

The mean value is known as the *mean range* and corresponds to the midpoint on the descending slope of *Fig.1.6.* This is the thickness at which roughly half the particles are absorbed. The ratio of straggling width σ_R and mean range R is nearby constant and can be described by the following relation[9]

$$\frac{\sigma_R}{R} = \frac{1}{\sqrt{M}} f\left(\frac{E_0}{Mc^2}\right) \tag{1.11}$$

where f is a slowly varying function depending on the absorber, E_0 and M which are the particle initial energy and mass respectively. Because of the $1/\sqrt{M}$ dependence, straggling is smaller for heavier ions than for protons.

More commonly, we need to know the thickness at which all the particles are absorbed. The point at which the curve drops to the background level should be taken, thus it is necessary to draw the tangent to the curve at the midpoint and extrapolate the value to the zero-level, hence the name of *extrapolated range* (see *Fig.1.6*).

Definitely, it is very important to take into account the range straggling because even small fluctuations can imply different depths of the delivered treatment dose.

1.2.3 Multiple Coulomb Scattering

In addition to the soft (excitation) and hard collisions (ionization) with atomic electrons of the medium, since protons, or ions, and target nuclei have the same charge sign, heavy charged particles are affected by a repulsive force passing through a material, thus they also suffers (less likely than an electron) the scattering effects with the nuclei. These are the main responsible for particles deflections from their initial trajectory, producing also the lateral widening of the beam, mostly in the Bragg Peak region, as can be seen in *Fig.1.7*.

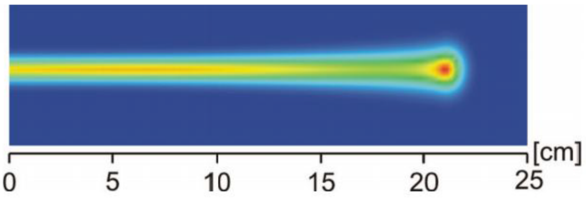

Figure 1.7: Lateral divergence of a proton pencil beam of 177 MeV in water due to multiple scattering effects. [10]

Unlike the case of the interactions with atomic electrons where the projectiles not only lose part of their energy, as already described, but also suffer from a slight deviation which, however, due of the great difference in mass, can be ignored, nuclei have much greater mass, therefore they can deflect them with larger angles.

This phenomenon is both due to the cumulative effect of many small deflections and to single large deflections of few particles. The first type of process is called *Multiple Coulomb Scattering (MCS)*, while the second is referred to as *Single Coulomb Scattering* and is usually negligible. Ignoring screening effects, the differential cross section for Coulomb scattering through a medium is described by the *Rutherford's formula*[3]

$$\frac{d\sigma}{d\Omega} = Z_T^2 Z^2 r_e \frac{(m_e c/\beta p)^2}{4sin^4(\theta/2)} \tag{1.12}$$

where p is the incident particle momentum and θ the scattering angle. Due to the $sin^{-4}(\theta/2)$ dependence, most of the particles are scattered at small angles. However, the cumulative effect is a change from the original track, since statistically the probability of relevant deviations increases event by event. The statistical distribution function $F(\theta, x)$ for the resulting scattering angle θ at penetration depth x

is described in the theory of Moliere (1948). For small angles ($\theta \simeq 0$) the higher order terms in Moliere's solution can be neglected and the angular distribution can be approximated by a Gaussian function whose standard deviation was calculated by Highland[11] as:

$$\sigma_\theta = \frac{13.6MeV}{pv} Z \sqrt{\frac{x}{X_0}} \left[1 + 0.038 log_{10} \left(\frac{x}{X_0} \right) \right] \tag{1.13}$$

with X_0 the radiation length, which is a characteristic strictly belonging to the material. Targets made of heavy elements cause a larger angular spread than targets composed of light elements with the same thickness. The angular distribution decreases as the particle momentum rises and therefore, for different ions at the same velocity, as the mass increases.

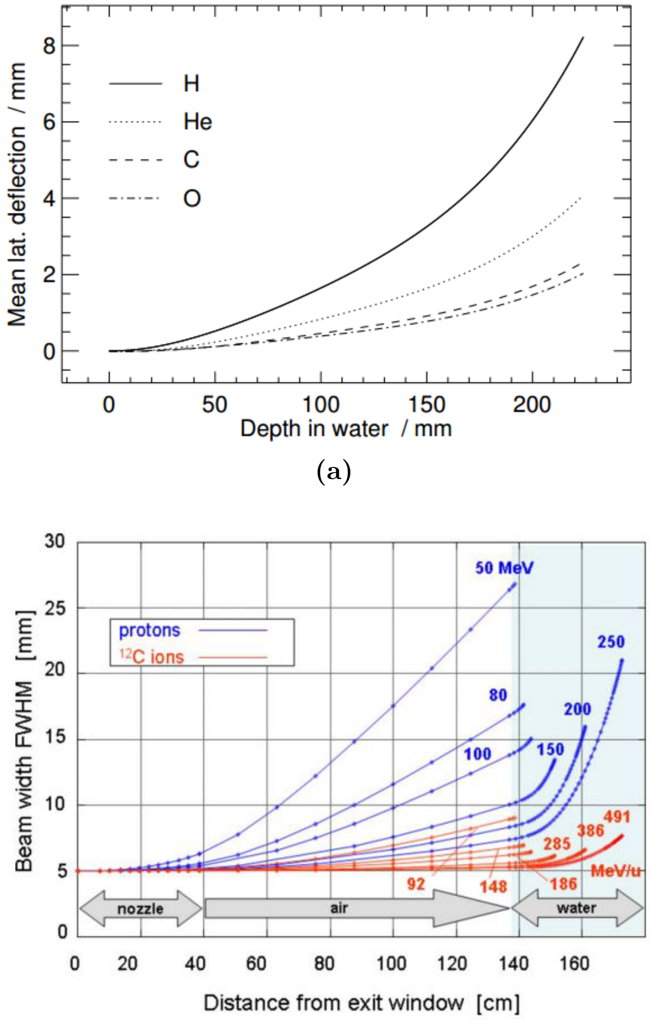

(a)

(b)

Figure 1.8: Lateral deflection of some ion beams as a function of the penetration depth.[12]

The small lateral spread of ions passing through a material is particularly advantageous compared to proton beams and it is of clinical relevance for treatments near organ at risk (OAR) area. Nevertheless, sometimes the lateral deflection of proton beams can be used in treatment plans to ensure full coverage of the tumor.

1.2.4 Bragg Peak and Dose deposition

When particles slows down, as $\beta\gamma$ goes below the MIP point because of the $1/\beta^2$ dependence of the dE/dx, they release all the energy at the end of their track in a particular point, called the *Bragg Peak (BP)* [3]. This property is a consequence of the dE/dx behaviour and it can be exploited to cure tumors: when the depth of the disease coincides with the position of the Bragg peak, it is possible to irradiate it with a large amount of energy. For this aim, considering a plot of deposited energy as a function of depth in the material, we can notice an important feature, i.e. the position of the BP depends on the initial energy of charged particles (*Fig.1.9*).

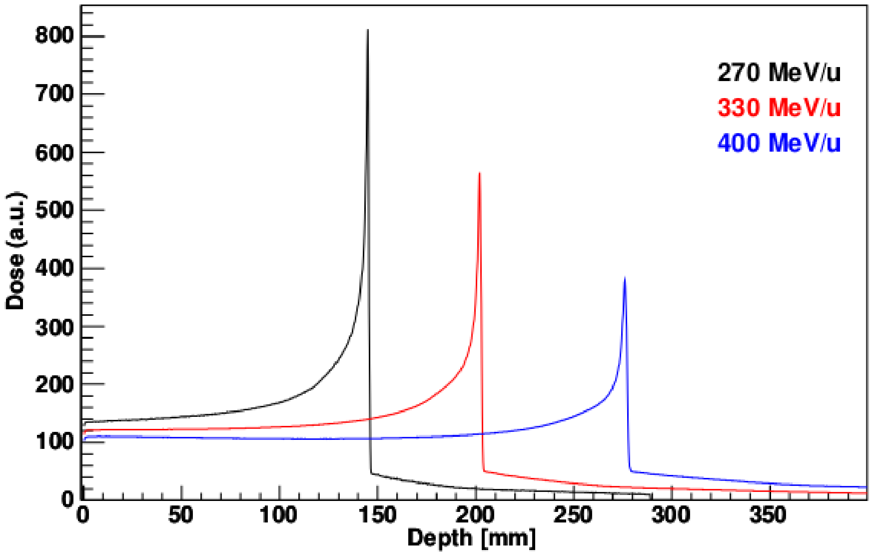

Figure 1.9: Depth-dose distributions in water with the characteristic *Pristine Bragg Peaks* for the same number of primary carbon ions at increasing energies. [13]

However, the cancer volume has a longitudinal extension, thus we have to widen the sharp BP, i.e. the highest dose region, in order to cover the tumor size. The technique employed to cover a region broader than the BP is shown in *Fig.1.10.* A series of beams (protons in the displayed case) with the same direction but different energies and intensities (the fluence [1] and the proton range are properly modulated) are delivered onto the patient, releasing a uniform total dose profile usually called *Spread-Out Bragg Peak (SOBP).* The physical processes governing the location of the peak are mainly the particle stopping power, the energy straggling, Multiple Coulomb Scattering and nuclear reactions to a much lesser extent [3].

---

[1] The *fluence* is defined as $\phi = \dfrac{dN}{dA}$ $[particles/cm^2]$, i.e. the number of particles traversing a unit area orthogonal to the beam direction.

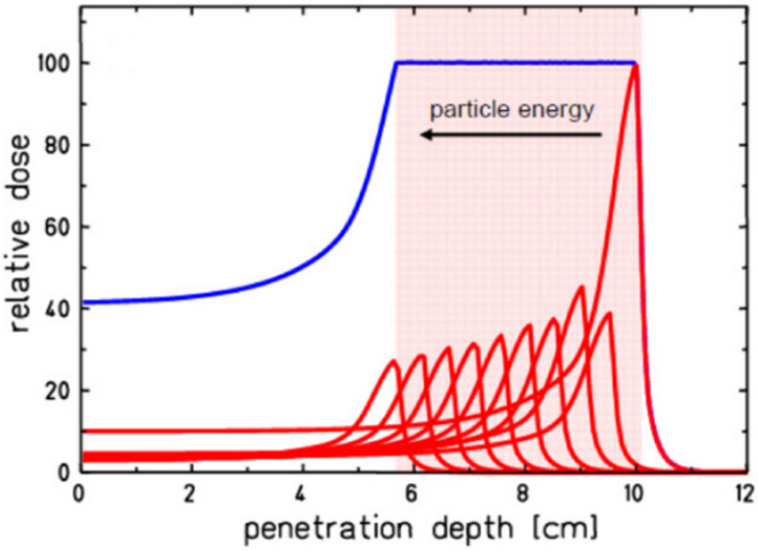

Figure 1.10: Example of the Spread-Out Bragg Peak. [14]

Obviously, this approach is based on a precise knowledge of the range of the particle fixed for the clinical treatment. Small modifications could either lead to an incomplete irradiation of the disease or move one of the BPs over a healthy region. As we have already said, the topic of *range uncertainty* is a major issue in hadrontherapy. It arises from different factors, such as the energy loss fluctuations, but also morphological changes in the patient (tumor shrinkage, cavity filling/emptying, inflamation, etc.), or patient mispositioning. In general, the range of therapeutic beams inside the patient is known with an uncertainty that goes up to 3% of the expected value[15]. In treatment plans additional safety margins are usually calculated through the range uncertainty, as: 3% of the range +3 mm, they are added to the cancerous region in order to avoid the delivery of beams in the direction of an *Organ at Risk (OAR)*.

Another fundamental parameter in hadrontherapy is the *absorbed dose* D, usually expressed in Gray ($1Gy = 1J/kg$)[17], which is defined as the quantity of energy dE released by ionizing radiation per mass unit dm:

$$D = \frac{dE}{dm}. \tag{1.14}$$

Nevertheless, it does not take into account the biological effects of the radiation. A comparison of the depth-dose profiles obtained from different types of ionizing radiation is shown in *Fig.1.11.* X-rays deliver higher doses in the entrance channel and they don't have a well defined range in the material. Even though at low doses, there is a significant exposition of healthy cells, tissue or organs to ionizing radiation before and after the "target" area and, consequently potential damage. This issue will be explored in detail in *Section 1.4.* On the contrary, hadronic beams show a favorable dose ratio between deep and shallow regions. Therefore, directing the BP on the tumor, healthy tissues receive a much lower amount of dose.

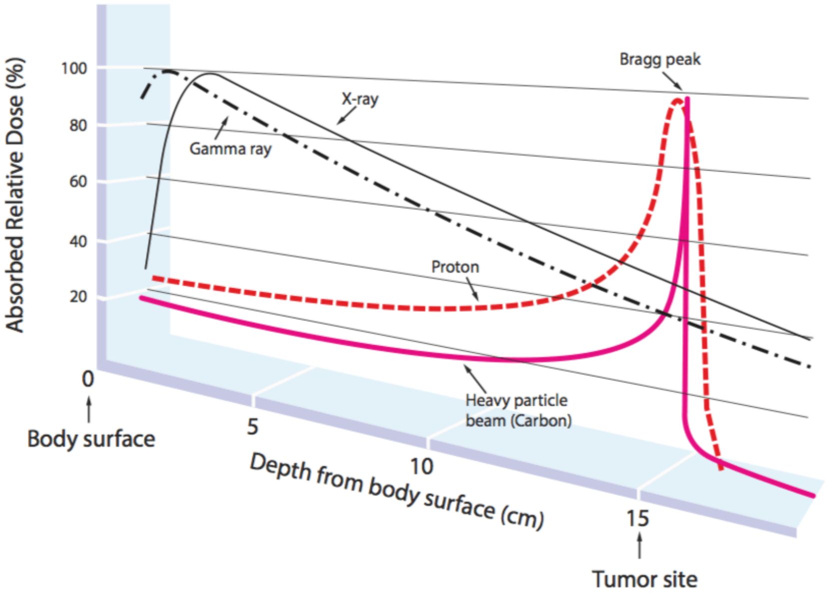

Figure 1.11: Schematic comparison of the dose of released radiation as a function of the penetration into the human body between different types of particles.[16]

Figure 1.11 also shows some important differences in dose deposition profiles of heavy ions with respect to protons:

- A narrower BP region and a lower dose in the entrance channel. This feature can be used to deliver less dose to healthy tissues before the tumor site and create a more precise profile of the BP over the disease. In effect, ions with higher atomic number Z produce a narrower and steeper BP.

- A dose tail after the BP, caused by projectile nuclear fragmentations. In particular, the contribution of nuclear fragmentation increases for heavier projectiles. Fragments have mostly the same velocity of the primary but lower charge and thus a longer range ($\propto Z^{-2}$) that exceeds the BP region. This effect is one of the main disadvantages of heavy ion beams and needs to be considered in *Treatment Planning System* since it delivers additional dangerous dose to healthy tissues.

In conclusion, the total dose deposited in healthy tissues is lower and more localized in carbon treatment, but the tails created by nuclear fragments can not be neglected. This issue represents the main reason why ^4He beams are currently under study as a possible solution, thanks to a higher binding energy between nucleons in α particles which should decrease the number of projectile fragmentations; on the other hand, the higher mass decreases the contribution of MCS with respect to protons.

The exact impact of nuclear processes is difficult to estimate because of missing cross section data. The latters are in fact fundamental to extract the characteristics of nuclear fragments (mass, charge, energy and direction) and calculate their energy deposition profiles. Analytical models, validated through MC simulations, are usually used for this goal. However, those currently employed are based on approximated calculations of nuclear reaction cross sections, which eventually introduce a source of dose uncertainty in clinical treatment plans, as will be explained in the next section.

1.2.5 Nuclear fragmentation

Heavy charged particles can also undergo *nuclear interactions* with the material nuclei. While the stopping process of high-energy ions slowing down in matter is dominated by the inelastic collisions with the atomic electrons, the probability of nuclear reactions, even if much smaller, leads to significant effects at large penetration depths. The interactions can be both elastic or inelastic. The first ones do not deposit energy in the medium and only account for an additional broadening of the beam, raising the tails of the angular distribution. The second ones are more violent collisions and can lead to nuclear fragmentation with the emission of lighter particles and/or nuclear excitation, with the consequent emission of prompt γ radiation $(0-10\ MeV)$[19]. Among these ones, the main process relevant for energy deposition calculations is nuclear fragmentation.

In proton therapy only target fragmentation is possible, generating secondary protons and neutrons; in heavy ion therapy, both target and projectile fragmentation can occur, strongly reducing the fluence of primaries as well as creating secondary fragments. The secondary (or higher-order) projectile-like fragments are moving with about the same velocity as the primary ions. They have in general longer ranges and produce a dose tail beyond the Bragg peak (*Fig.1.12)*.

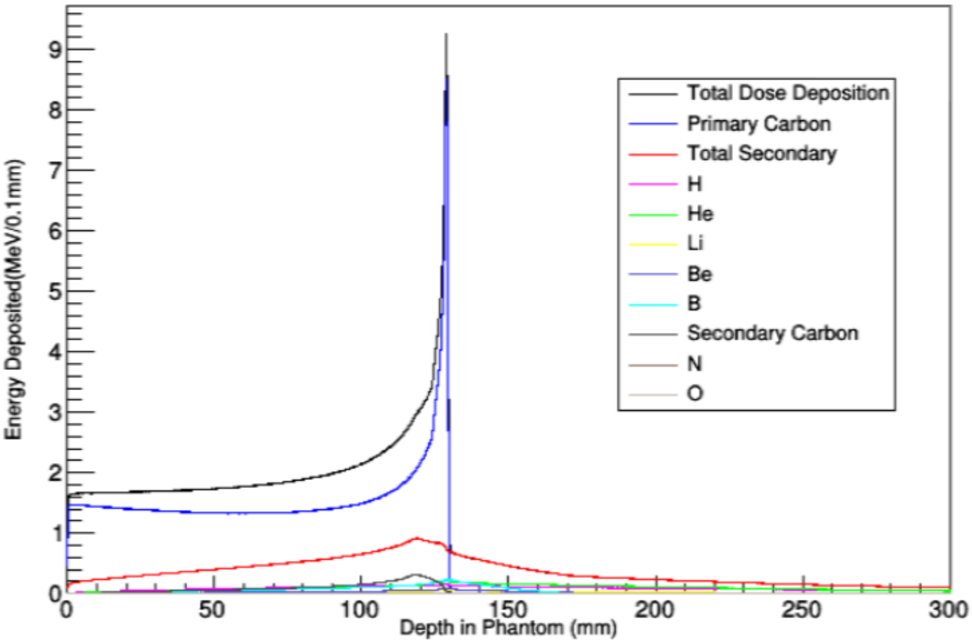

Figure 1.12: Contribution of projectile nuclear fragments to the depth-dose profile of a 330 MeV/u carbon ions beam impinging on a PMMA (PolyMethyl MethAcrylate) target.[20]

The effect is as much greater as the higher the mass of the ion beam. Their angular distributions are mainly determined by reaction kinematics, but much broader than the lateral spread of the primary ions caused by Multiple Coulomb Scattering. The target fragments and the decay and evaporation products (essentially protons, neutrons) are isotropically distributed in space and have a low kinetic energy and therefore small range, which is why they are not generally treated as a major problem in distributed dose in hadrotherapy treatment with ions with $Z > 1$.

Most of the nucleus-nucleus collision models describe the interaction as a two step process, called cascade-evaporation or, more frequently, *abrasion-ablation model*[21].

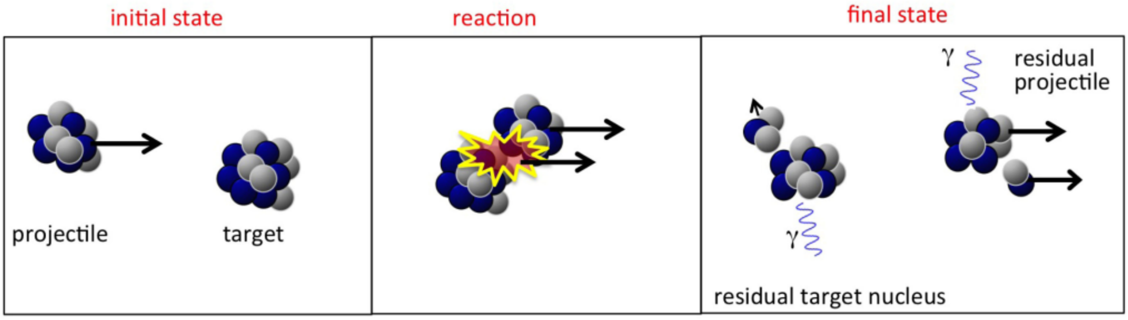

Figure 1.13: Visualization of the abrasion-ablation model for a nucleus-nucleus interaction. Note that target fragments have a much lower velocity than the projectile, therefore they will be emitted almost isotropically. Instead, projectile fragments are mainly emitted forward and can penetrate deeper inside the material with respect to the initial particle.[19]

As we can see in *Fig.1.13*, the first step is called *abrasion*: the projectile and target nuclei overlap, forming a hot reaction zone (fireball) that gets abraded. The fragment of the projectile nucleus continues with almost the same direction and velocity, while the remaining target fragment is just slightly affected by the interaction. The second one is the *ablation*: the two nuclei fragments and the fireball are initially in a highly excited state. In this case the decay of the residual particles into their ground state occurs, with possible emission of γ-rays or light particles, hence the name "evaporation". The abrasion-ablation model is sufficiently accurate in describing peripheral collisions between projectile and target, which constitute the majority of nuclear interactions in the energy range of the hadrontherapy.

A fundamental quantity that characterizes this kind of interaction is the *nuclear cross section*, since it links the probability that a nuclear reaction will occur with beam and target properties. The cross section [3] for a particular process can be defined as:

$$\sigma = \frac{N}{N_i}\frac{A}{\rho x N_A} \tag{1.15}$$

where N is the number of interactions and N_i is the number of incoming particles, while ρ, A and x are the target density, mass number and thickness, and $N_A = 6,0221 \times 10^{23}$ is the Avogadro's number. The conventional unit is the barn (b), where $1\ b = 10^{-28}\ m^2 = 100\ fm^2$. In this framework, an approximated expression for the cross section of inelastic nucleus-nucleus interactions can be obtained through the Bradt-Peters semiempirical formula[22]

$$\sigma_{inel} = \sigma_{tot} - \sigma_{el} = \pi r_0^2 (A_{proj}^{1/3} + A_T^{1/3} - b)^2 \tag{1.16}$$

where $r_0 \simeq 1.2\ fm$ is the nucleon radius, A_{proj} and A_T are the mass numbers of projectile and target nuclei and b is an overlapping factor. This expression is valid for proton with $E \geq 15\ MeV$ and nucleus with $E \geq 100\ MeV/u$. For high energy proton ($> 100\ MeV$) a typical parametrization is adopted concerning proton-nucleus interactions:

$$\sigma_{inel} \approx A_T^{2/3} mb. \tag{1.17}$$

In the energy range relevant for the hadrontherapy, experimental values for σ_{inel} are unfortunately poorly known, especially for light nuclei ($A < 20$). This makes it difficult to provide a sufficiently accurate model for particle transport and energy deposition. This is particularly true for double differential cross section ($d^2\sigma/dEd\Omega$) data, which should provide the probability of emitting a fragment in the energy range dE within the solid angle $d\Omega$.

Influence of nuclear reactions on delivered dose

- Protons

  The consequences of the nuclear reactions are shown in *Fig.1.14*.

  From GEANT4[2] simulations, one can note the ratio of projectiles which have not experienced a nuclear collision on a nucleus of the absorber as the penetration depth increases (left panel) and the corresponding Bragg Curve (the evolution of *Linear Energy Transfer (LET)* per incident proton with the penetration depth, right panel) for 150 MeV protons in liquid water. On both panels, the black curve corresponds to simulations in which there is only the electromagnetic interaction and the red curves to the case in which there are also the nuclear processes. The effect of the projectile consumption is clearly seen on the left graph.

---

[2] Geant4 is a toolkit for the simulation[24] of the passage of particles through matter. Its areas of application include high energy, nuclear and accelerator physics, as well as studies in medical and space science.[23]

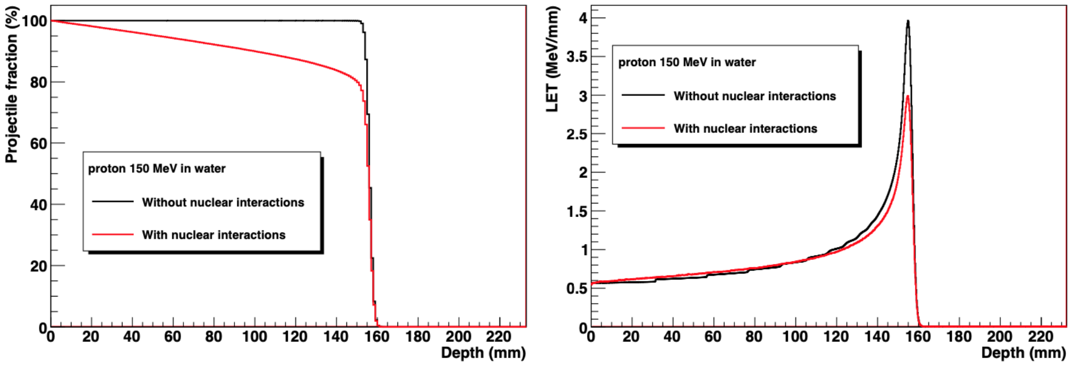

Figure 1.14: GEANT4 simulations of the primary protons ratio (left panel) and the mean LET for protons (right panel) as functions of the penetration depth for 150 MeV protons.[25]

Whereas all projectiles reach the Bragg Peak for electromagnetic interaction simulations, only 80% of them reach it for nuclear interaction simulations. As a consequence, the energy deposition at the Bragg Peak is reduced by 20% for nuclear collisions compared to electromagnetic case. We can note that nuclear collisions have no effect on the position of the Bragg Peak which is only driven by the BetheBloch equation. Since the simulation deals with proton beam, the related secondary fragments are only generated from the target. Thus, their velocity is very small and hence their range do not exceed few micrometers. They deposit their energy close to the collision location. For this reason, the integral of the Bragg Curve for nuclear interaction simulations is still $\sim$ 97% of the projectile total energy.

- Carbon ions

  The influence of the nucleus-nucleus reactions on the dose deposition for 290 MeV/u ^{12}C ions can be observed on *Fig.1.15* thanks to the GEANT4 simulation framework.

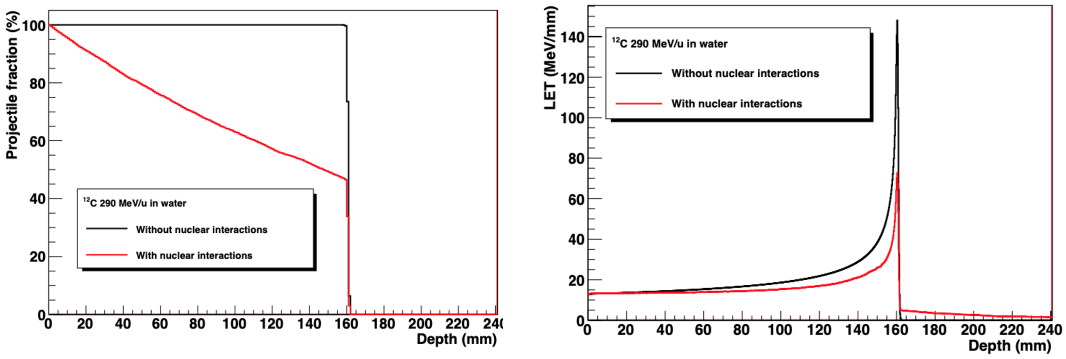

(a) **(b)**

Figure 1.15: (a) Evolution of the primary ^{12}C ions ratio [25] and (b) the mean LET for ^{12}C ions with the penetration depth[25].

> As we can see, only 50% of projectiles reach the Bragg Peak (*Fig.1.15(a)*), leading to a reduction of 50% on the energy deposition per incident carbon ions at the same point (*Fig.1.15(b)*). The ratio of ^{12}C ions decreases exponentially with respect to the penetration depth when nuclear reactions occur. As for protons, the locations of the Bragg Peaks are identical for electromagnetic and nuclear simulations and the related integral is $\geq 93\%$ of the incident energy for the second case. Also the target fragments have a very short range and deposit their energy close to the collision location. The difference compared to protons is, as expected, the energy deposition tail beyond the Bragg Peak due to projectile fragmentations whose fragments have a velocity close to the primary particles. Therefore, beacause of A/Z^2 scaling of the ranges, they will travel a longer path before stopping. In particular, the lighter fragments will have a much longer range with respect to the primary ions.

These simulations show clearly that the dose map is significantly changed when the nucleus-nucleus and proton-nucleus collisions are taken into account.

1.3 Biological response from charged particles

The ability of the hadrontherapy to defeat a tumor is closely linked to the biological damage caused to the human cells, thus DNA damage caused by radiation will be discussed in this Section.

Heavy charged particle treatments are mainly indicated for deep-seated, radioresistant, hypoxic tumors, which can be located near Organs At Risk (OAR). Moreover, hadrons show an enhanced biological effectiveness in cell killing with respect to photons, allowing for an even lower dose exposure. Still, there is ongoing research on factors such as *Relative Biological Effectiveness (RBE)* variability and nuclear fragmentation. These effects are currently not or only partially included in Treatment Planning Systems (TPS). The latters could be substantially improved if the calculations accurately take into account the biological effect of nuclear fragmentation and its influence on RBE.

1.3.1 Linear Energy Transfer (L.E.T.)

One of the fundamental quantities in radiobiology is the *Linear Energy Transfer (LET)*[18]. It is similar to the stopping power defined in Equation (1.1), but with an important distinction. While dE/dx includes all the electromagnetic losses of the particles, LET is defined as the energy released inside a medium per unit path length near the primary particles tracks excluding interactions that produce δ-rays with energy greater than a certain threshold Δ, as in the following relation:

$$LET = \left(\frac{dE}{dx}\right)_{\Delta} \tag{1.18}$$

It is expressed in $KeV/\mu m$. When considering indirectly ionizing radiation beams (photons or neutrons), LET refers to the stopping power of secondary particles.

In clinical practice, radiations are usually characterized through their LET and divided in *sparsely ionizing* (low-LET, $\sim 1\ KeV/\mu m$) and *densely ionizing* (high-LET, $\sim 10 - 100\ keV/\mu m$).

In particular heavy charged particles have very large values of *LET* (see *Fig.1.16*) and consequently they are more harmful, since they ionize a high number of atomic electrons along their track and have a very short mean free path inside a medium. This means that hadrons produced a much higher ionization density and have better chances of interacting multiple times with the same DNA molecule. Therefore, they are considered *high-LET* particles. On the other hand, photons have lower values (see *Fig.1.16*), even secondary electrons have low LET. This means that the number of ionizations produced inside a cell per incident particle is relatively small. They are usually referred to as *low-LET* particles.

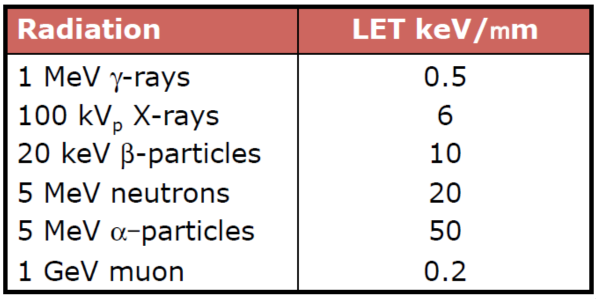

Radiation	LET keV/mm
1 MeV γ-rays	0.5
100 kV$_p$ X-rays	6
20 keV β-particles	10
5 MeV neutrons	20
5 MeV α-particles	50
1 GeV muon	0.2

Figure 1.16: Some tabulated LET values for high and low-LET particles.[26]

As shown in *Fig.1.17*, higher is the projectile charge higher will be its LET, the number of ionizations and as a consequence, more biological damages occur in the human cell.

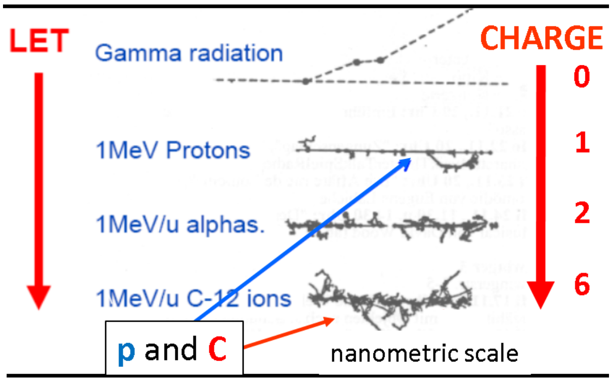

Figure 1.17: Sketch of the number of ionizations along the path for different particles at 1 MeV/u in nanometric scale.[26]

Summing up, this quantity makes it possible to evaluate the biological damage (we will see in the next subsections) because it reflects the ability of the radiation to produce ionization and therefore the effectiveness of this damage.

1.3.2 DNA damage and cell survival

The basic aim of any type of radiotherapy is to use ionizing radiation to kill tumor cell or, at least, interrupt their ability to reproduce. Thus, the actual target is the DNA inside the cell nuclei. Its damage is usually referred to as:

- *Direct* when particles break one or both of its chains. High-LET particles are the main responsible for this kind of events.
- *Indirect* when DNA gets damaged by chemical reactions with very reactive molecules, called free radicals[3], generated by the ionization of the water molecules[27]. It is mostly observed in low-LET particles case.

The ionizing radiation effects depends mostly on the LET values (see *Fig.1.18* and *1.19*), as we have already said. In general the ionization events generated by low LET radiations, such as particles with a LET value around 0.2 $-0.5\ KeV/\mu m$, for example photons, are quite separate from each other.

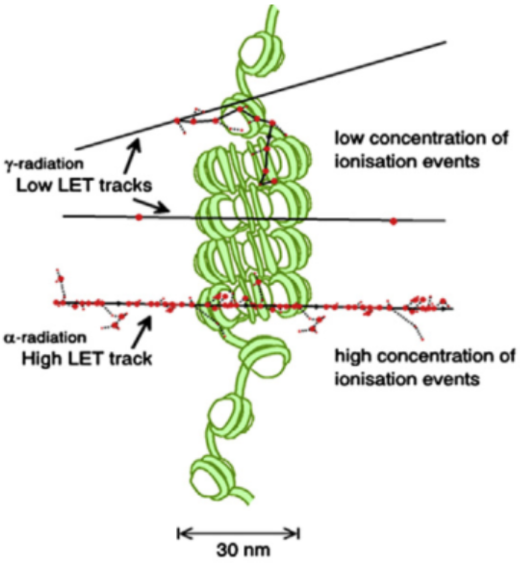

Figure 1.18: Example of low/high LET interactions.[28]

---

[3] In detail the ionized water molecules split into a hydroxyl group OH^- and hydrogen H^+. The group OH^- is a free radical that diffuses into tissues and contributes to DNA damage.

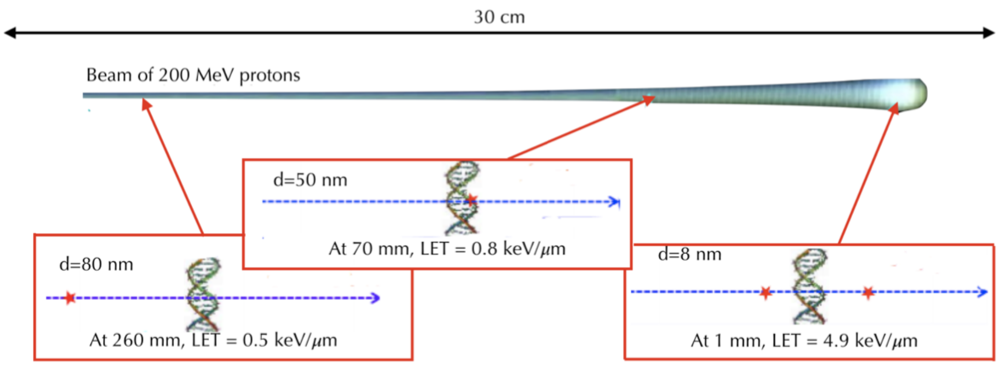

Figure 1.19: Ionization density of proton ion beam at 200 MeV for different distance from the Bragg Peak placed at 30 cm of penetration depth. The data are obtained considering a water target. The parameter d represents the distance between two consecutive ionization events.

In the process of DNA damage, the geometry of its molecule plays a key role. The DNA double helix in fact has lengths of the order of meters, thicknesses of the nanometer and it is located inside the core ($\approx 5 - 10 \mu m$) of the cell. The types of lesion induced by the particles on its helix are usually classified as:

- *Single Strand Break (**SSB**)*: it is confined to only one of the two strands, breaking it into two pieces. This type of damage has low biological impact because cells are able to repair most of these fractures without consequences. SSBs are the main kind of breaks induced by X-rays.
- *Double Strand Break (**DSB**)*: in this case both of the DNA strands are broken, either at the same level or at a distance of few DNA base pairs. These type of lesions are very difficult to repair and usually result in cell death. Heavy charged particles mainly cause DSBs when interacting with cells.

However, even though DNA is protected by a repair system so it can recover its functionality even after damage to single or double strand (the latter with less probability), when it is exposed to concentrated and very high doses, the injuries to the molecules are assembled in clusters and the repair system fails in restoring the cell. Damaged DNA reaches *apoptosis* (programmed cell death). After that, the cell is unable to repair itself on a time scale of minutes / hours[29].

In particular for low-LET particles the contribution of indirect damages is about 65%, which is larger than the direct ones (about 30%), and only $\sim$ 30% of DSB are clustered, while for high-LET ions, the contribution of direct hits is higher and the clustered damages rise to about 70% [30]. We can note that healthy tissue are much more efficient than cancer in this self-repair process. Therefore, the effectiveness of the radiotherapy and the hadrontherapy for treatment and control of tumors is specially based on this feature.

The main potential consequences on DNA are summarized in *Figure 1.20.*

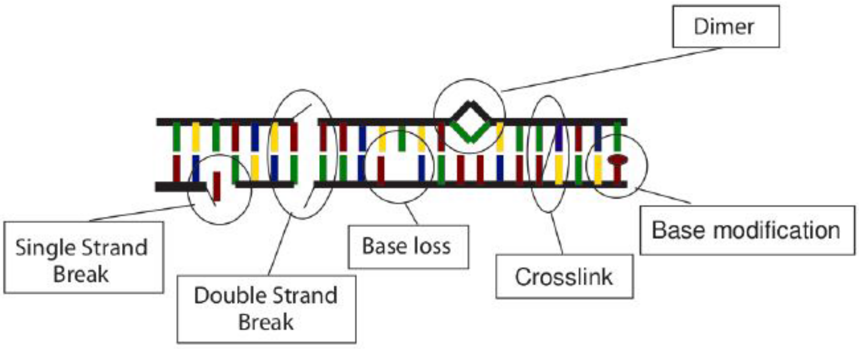

Figure 1.20: The main DNA damages are schematized: gene mutations, alteration of the DNA chemical structure and chromosomal aberrations.[27]

The link between radiation dose and cell survival has been studied for many years through *"in vitro"* experiments. In these studies, the "death" of a cell can be reached in different ways. For non-reproductive differentiated cells (like neurons), it usually implies the loss of a specific function while for reproductive and less differentiated cells (e.g. stem cells, bone marrow, etc.), death is normally represented by the loss of reproductive capabilities.

The different behaviour in response to photons and heavy ions can be achieved by cell survival curves (see *Fig.1.21*) which are currently defined through one of the most common models used in clinical radiation therapy to link dose and cell damage, i.e. **the linear-quadratic model** (LQ):

$$S(D) = e^{-\alpha D - \beta D^2} \tag{1.19}$$

where S is the surviving fraction, D is the absorbed dose and α and β are experimentally determined parameters that characterize the behaviour of cells when irradiated. The latters can vary depending on targeted tissue and type of radiation and in particular their ratio $R = \alpha/\beta$ is used to define the radiosensitivity of the exposed region: conventionally, high R value is typical of *early responders tissues* (such as most tumors, $7 < R < 20$ Gy), thus related to high reproduction activity, whereas a low ratio is common in *late reactive cells* (e.g. normal tissues, $0.5 < R < 6$ Gy), which corresponds to a low reproduction rate[31]. Furthermore radiosensitivity differs from cell line (i.e. the particular type of cell) to cell line and it is also influenced by the cell cycle phase.

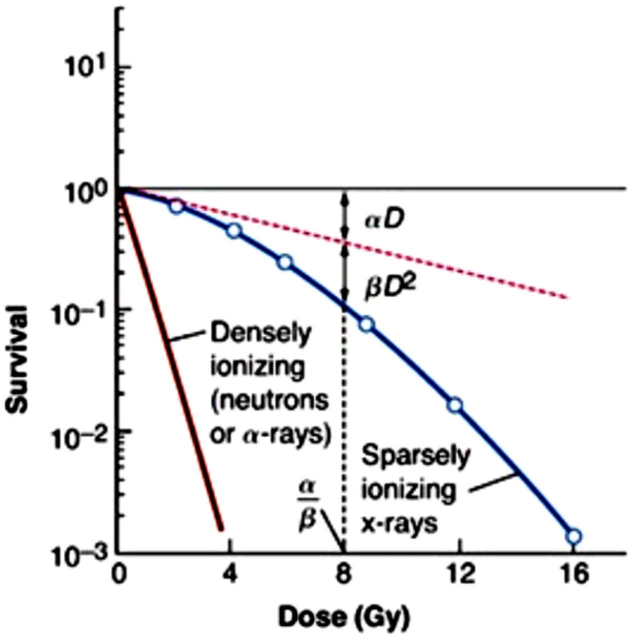

Figure 1.21: Example of cell survival curves for different types of radiation. The quadratic "shoulder" depends on α/β value and it is evident in the X-ray curve and negligible for high-LET radiations. This ratio represents the dose for which the linear and quadratic damage give the same effect.[31]

The linear-quadratic model shows to be quite effective in reproducing the experimental data up to a few decades of S.

As shown in *Fig.1.21* the behavior of the survival curves strongly changes between low-LET and high-LET radiations. This is mainly due to the fact that the α and β parameters are linked respectively to DSB and SSB damage. Since this last one is almost absent for heavy charged particles, the linear term is always dominant and the curve can be approximated to a single exponential as:

$$S(D) = e^{-\alpha D} \tag{1.20}$$

When the radiation LET increases, in fact, the slope becomes steeper because of the more severe damages produced by high LET radiation. Therefore, the survival curve shows a purely exponential behaviour, described by the *linear model* which obviously differs from the previous one since in this case the quadratic term of the exponential can be neglected. This is also a reflection of the higher effectiveness of hadrons in cell killing, hence a significant biological advantage. The damage induced in DNA by high-LET radiation is much harder to repair, meaning that hadrons beams have higher chances of killing the cells, especially in the BP region. Otherwise, having lower LET in the entrance channel they produce less severe lesions and higher cell survival rates.

Since empirical tests determine that DNA repair mechanisms of tumor cells are significantly less effective than those of normal healthy cells (i.e. tumor cells exhibit low values of β) it is very useful exploiting this effect by *fractionating* the total radiation treatment into a succession of small doses at different times, typically one dose-fraction (< 2 Gy) a day for 6–7 weeks, as in *Fig.1.22*.

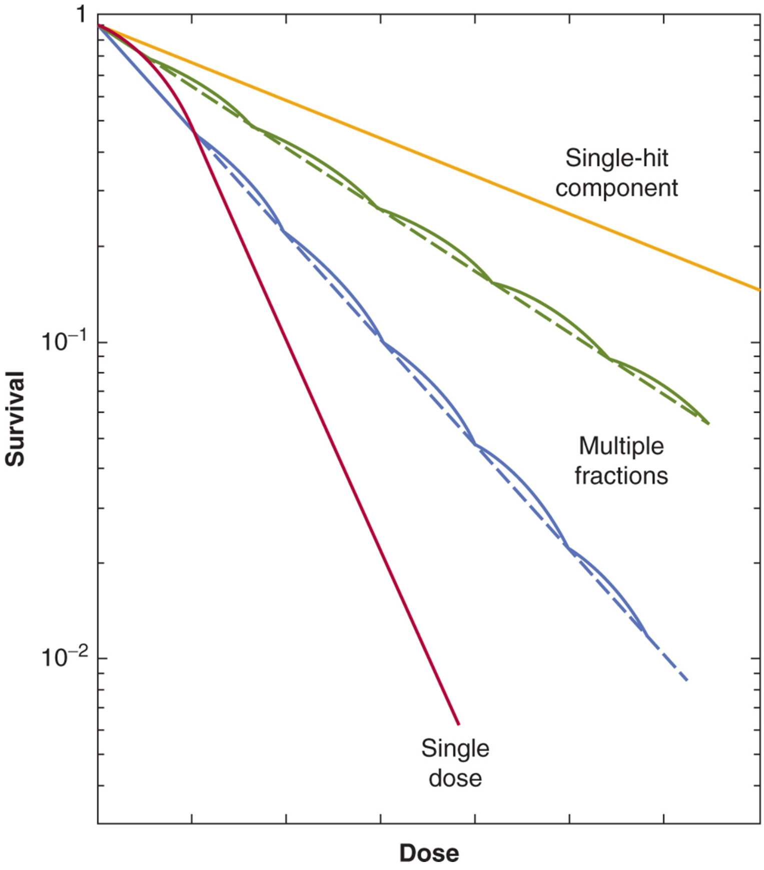

Figure 1.22: The influence of fractionating the radiation treatment on the shape of cell-survival curves. When repair occurs between the fractions, the shoulder of the survival curve is repeated for every fraction resulting in curves that are shallower for smaller fraction sizes (blue vs green curves). The orange curve represents a limit below which further reduction of the fraction size will no longer reduce the effective slope of the survival curve, therefore a low dose rate, and it differs among cell populations.[32]

After each fraction the normal healthy cells are able to repair some of the radiation damage whereas the tumor cells are unable to repair the damage, leading to compounded decimation with each new fraction. The fractionation is optimized when maximum cancer cell death is achieved with minimal damage to normal tissues. Determining the optimal compromise between dose per fraction, time interval between fractions and total treatment dose, in order to avoid that the overall effect is less than the expected one, is the subject of a great deal of current research[33].

1.3.3 Dosimetric Quantities

The dose deposited in tissue is the most important physical quantity in hadrontherapy, it has already been defined by the term absorbed dose in the previous Section 1.2.4. Dose measurements are normally performed with air-filled ionization chambers and have to be converted to the absorbed dose in water[4] by correction factors. For a parallel beam with particle fluence F the dose deposited in a thin slice of an absorber material with mass density ρ can be calculated [34] as follows:

$$D[Gy] = 1.6 \times 10^{-9} \cdot \frac{dE}{dx}\left[\frac{KeV}{\mu m}\right] \times F[cm^{-2}] \times \frac{1}{\rho}\left[\frac{cm^3}{g}\right] \tag{1.21}$$

where dE/dx is the energy loss of the particles per unit path length explained in section 1.2.1. It is measured in *Sievert*(Sv)[5].

However, considering the absorbed dose, we have to specify type and energy of the radiation considered and the target, therefore it is very useful to define two dosimetric quantities. The first one is the *equivalent dose* (Sv)[18], which takes into account the type of radiation for the biological effects:

$$D_{eq} = \sum_R w_R D \tag{1.22}$$

where w_R is the (dimensionless) *quality factor*, which characterizes the type of radiation R, and D, the absorbed dose. The term w_R, in particular, represents a correction parameter by which the absorbed dose is weighted in order to consider the different danger of the ionizing radiations. Moreover it is defined as the ratio of the biological damage produced by the absorption of 1 Gy of that radiation to those produced by 1 Gy of γ (reference radiation). Its values were obtained from results of epidemiological and radiobiological studies (see *Fig.1.23*) and are periodically reviewed.

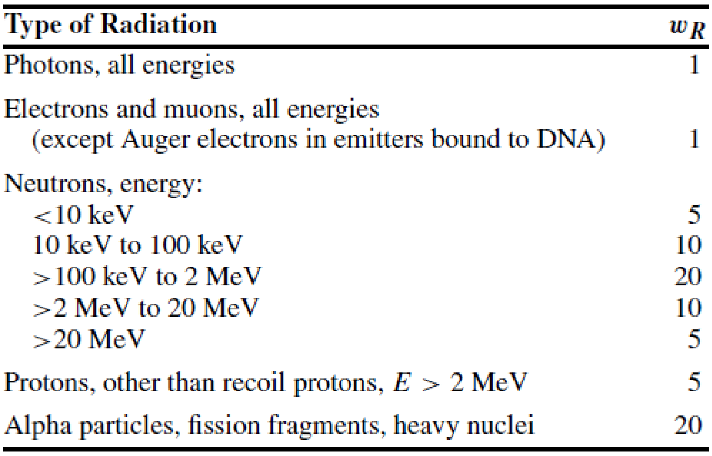

Type of Radiation	w_R
Photons, all energies	1
Electrons and muons, all energies (except Auger electrons in emitters bound to DNA)	1
Neutrons, energy:	
$<$10 keV	5
10 keV to 100 keV	10
$>$100 keV to 2 MeV	20
$>$2 MeV to 20 MeV	10
$>$20 MeV	5
Protons, other than recoil protons, $E > 2$ MeV	5
Alpha particles, fission fragments, heavy nuclei	20

Figure 1.23: Quality factor w_R as a function of energy (MeV) for different types of radiation.[17]

The second one is the *effective dose* (Sv): the exposure of different tissues and organs to the same equivalent dose may involve a different cells response due to their specific radiosensitivity, thus we have also to consider this effect.

---

[4] Water is used as tissue reference medium because human body is $\sim 70\%$ composed by this element.

[5] The Sievert has the same Gray dimension but the latter does not consider biological effects.

The effective dose is defined as the weighted sum of the equivalent doses for various organs and tissues[18]

$$D_{eff} = \sum_T w_T D_{eq} = \sum_T w_T \sum_R w_R D \tag{1.23}$$

where w_T is the *tissue weight* (see *Fig.1.24*), which accounts for the radiosensitivity of the irradiated organs (for istance, radiation destroys the cancer more easily in the very sensitive tissues case).

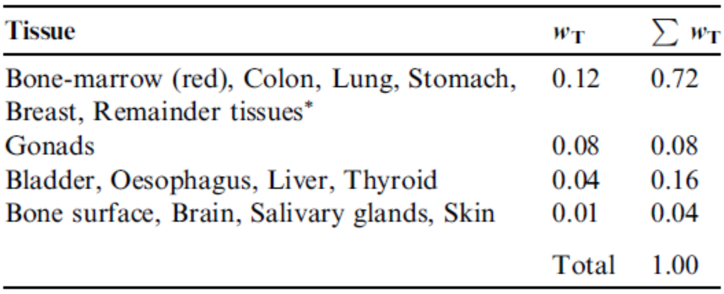

Tissue	w_T	$\sum w_T$
Bone-marrow (red), Colon, Lung, Stomach, Breast, Remainder tissues*	0.12	0.72
Gonads	0.08	0.08
Bladder, Oesophagus, Liver, Thyroid	0.04	0.16
Bone surface, Brain, Salivary glands, Skin	0.01	0.04
	Total	1.00

Figure 1.24: Weight factor values w_T related to each organ and tissue, defined by the ICRP (International Commission on Radiological Protection).[35]

1.3.4 Relative Biological Effectiveness (R.B.E.)

A steeper survival curve implies that heavy charged particles need to deposit a lower dose, with respect to photons, to produce the same amount of tissue damage.
This effect is quantified by the *Relative Biological Effectiveness (RBE)*, which is defined as the ratio between the dose D_X of a reference radiation, typically photons (γ-rays from ^{60}Co or X-rays), and the one provided by the radiation of interest to obtain the same biological effect (i.e to achieve the same survival ratio S)[36]

$$RBE = \left.\frac{D_X}{D}\right|_S \tag{1.24}$$

The RBE is a quite complex quantity, since it depends on many physical and biological parameters (LET, dose, dose rate, fractionation, particle mass, cell radiosensitivity, biological endpoint, oxygen concentration, cell cycle phase, proliferation rate, etc.).

Figure 1.25 shows different survival curves for photons (full line) and for heavy ions (dashed line).

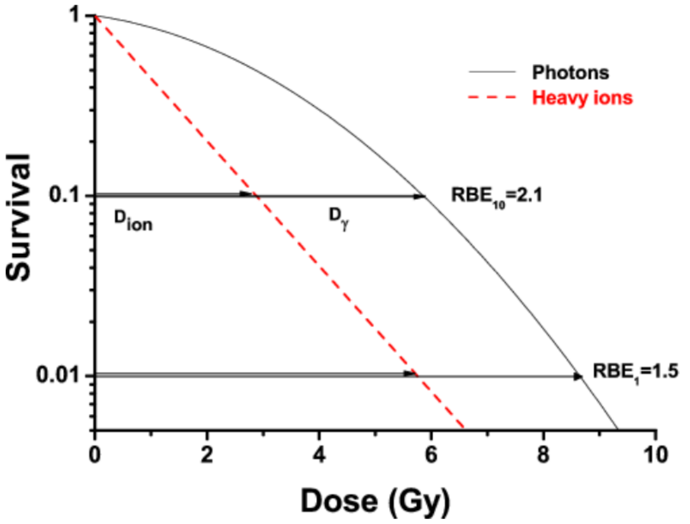

Figure 1.25: Survival curves and determination of RBE for cell inactivation for 10% and 1% survival level for a typical heavy ion irradiation.[37]

As we can see, depending on the survival cells rate, the RBE can range from 1.5 (1% surviving cell) to 2.1 (10% surviving cell). RBE strongly depends on the ion employed and for each ion can range in an interval dependent on the delivered dose. Since due to the high energy deposition density the radiation damage is severe, in case of high LET particles the RBE is high. In clinical practice, proton RBE is considered constant and equal to ~ 1.1 according to ICRU recommendations[38]. Protons are therefore considered 10% more effective than photons ($RBE = 1$). The choice of a fixed value is due to the fact that proton LET along the track does not increase as much as for heavier ions.

For other ions RBE varies significantly (up to values > 3 in case of carbon ions), as shown in *Fig.1.26*. In fact, the RBE increases with LET up to a peak value (with a range between about 100 and 200 $KeV/\mu m$ for $Z > 1$ ions), whose actual position is particle-dependent and usually shifts to higher LETs for heavier ions[6] and it is reached when the distance between two subsequent interactions is comparable to the transversal dimension of DNA ($\sim 2nm$) and decreases as LET increases further. After this peak, the RBE value drops because of overkilling effects, i.e. the damage induced in cells overcomes the amount needed to cause death and tissues receive some unnecessary dose. Thus, the further dose deposited by ions with an even higher LET is "wasted" and the RBE falls.

---

[6] At the LET value corresponding to the protons RBE maximum, heavier ions are faster than protons, thus a reduced ionization density. Therefore, light particles are generally more effective in their peak than heavy at the same LET (see *Fig.1.26*).

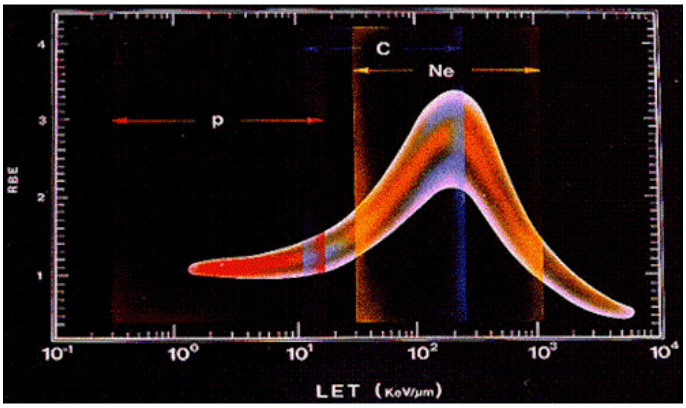

Figure 1.26: The RBE as a function of LET for different particles.[39]

Moreover, the idea of RBE is crucial in hadrontherapy since it introduces the concept of *RBE-weighted dose* or *biological dose*, a key parameter in *Treatment Planning System*(TPS). This quantity is usually measured in Gy-RBE and is obtained multiplying the absorbed *physical dose* D deposited by the RBE of the utilized radiation. It expresses the conventional X-ray dose needed to have the same biological effect as the radiation of interest. Thus, RBE-weighted dose gives an idea of the biological damage caused to each region of the body.

RBE and nuclear cross section

TPS usually include theoretical models that account for RBE variability of heavy ion beams along their path, mainly caused by high LET changes. In fact, the assumed RBE value for ions is almost > 3.

On the other hand, for protons the average value is around 1.1. The rationale for using a fixed value is that their LET does not change as much as for heavy ions. However, different radiobiological studies have highlighted a non negligible increase in RBE both in the entrance channel and in the *SOBP*, with values ranging up to 1.6[36]. This effect could lead to an underestimation of their biological effect. The source of RBE variability in protons is still under investigation at the moment but a viable explanation could be the target nuclei fragmentation. The resulting secondary particles can have very different kinetic energy and LET, depending on projectile and target features. Still, target nuclei are usually heavier than protons, so there is a high chance of producing a short range, high LET (and RBE) fragments that will release their entire energy in few μm.

Thus, these fragments can locally increase the actual RBE of the beam and play a significant role in the total dose distribution. The impact of nuclear fragmentation for a proton beam is simulated in *Fig.1.27*.

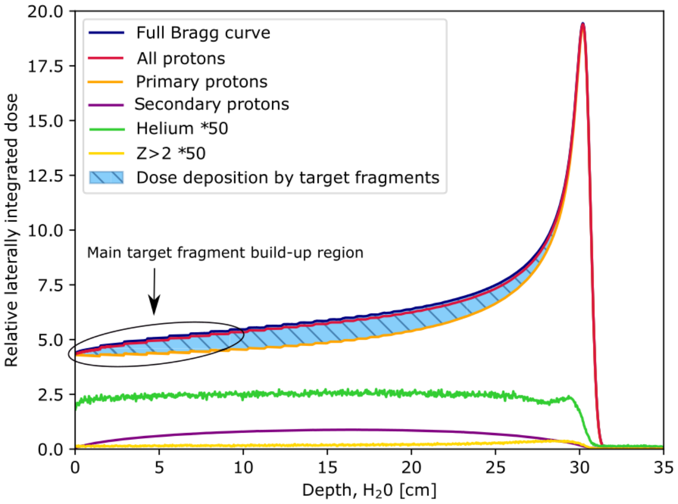

Figure 1.27: MC simulation (FLUKA) of the Bragg curve of a 220 MeV proton beam. The different contributions to the depth-dose profile are highlighted, showing the relevance of target nuclear fragmentation in the entrance channel.[40]

The results show that even though the number of nuclear interaction is higher in the BP, target fragments account for only 2% of the biological effect in this region. Instead, their contribution is much higher in the entrance channel, where nuclear fragments are responsible for 10%.

However, the actual contribution of target fragmentation is currently very difficult to evaluate. The lack of experimental cross section values represents a source of uncertainty, therefore the available models are not accurate enough and a direct comparison with data is still impossible in most cases. To preserve the healthy tissues and improve the treatment planning a more complete proton RBE model, which include the fragmentations effects, must be found.

Moreover, it is important to notice that, while target fragmentations are probably more significant in protontherapy, the impact of these processes needs to be correctly evaluated also for heavy ion beams. This knowledge is essential to be able to predict, with some precision, what happens in the patient's body. For this purpose, the medical field requires an in-depth study of the process of fragmentation of hadron beams on light targets, in general, they are light elements or materials, such as carbon, water or PMMA (polymethylmethacrylate), in order to simulate human tissues as likely as possible. It is important to acquire knowledge on what types of fragments are produced, in what proportion and with which cross sections and their kinematic properties, such as kinetic energy and emission angle, through fragmentation measures for different types of projectile-target pairs , at various energies and thicknesses.

In conclusion, nuclear reactions makes no easy the evaluation of fragments contribution to the overall dose and so the RBE computation.

Therefore, the aim of the **FOOT** (*FragmentatiOn Of Target*) experiment, described in the next chapter, is to perform a set of nuclear cross section measurements at particle-therapy energies in order to cover this lack of data currently unavailable in nuclear physics databases.

1.3.5 Oxigen Enhancement Ratio (O.E.R.)

Another important biological effect to consider is the different oxigen concentration in tissues/organs: cells with a low oxygenation rate (hypoxic cells) are more resistant to radiations than aerobic cells. As a consequence, more dose is needed to destroy hypoxic cells. Unfortunately, when a tumor grows in volume, new blood vessels are created in order to supply oxygen to the cells, but these connections are often not generated fastly enough or they are located too far from the original vessels to be sufficiently oxygenated, thus they might be defective. This implies radioresistant hypoxic regions, especially in the core of large tumors.

This effect is parametrized by the *Oxygen Enhancement Ratio (OER)* which is defined as follows:

$$OER = \frac{D_{hypoxic}}{D_{aerobic}} \tag{1.25}$$

where $D_{hypoxic}$ and $D_{aerobic}$ are the doses resulting in the same biological effect with hypoxic and normoxic cells respectively. Typically, the OER is about 3 for photons, whereas it is greatly reduced to about 1 in the case of higher LET particles, therefore the latters are particularly suited to treat radioresistant tumors at the same dose level. The *Fig.1.28(a)* shows the survival curves for particles with different LET values for aerobic and hypoxic cells. The OER value clearly depends on the LET value, as shown in *Fig.1.28(b)*.

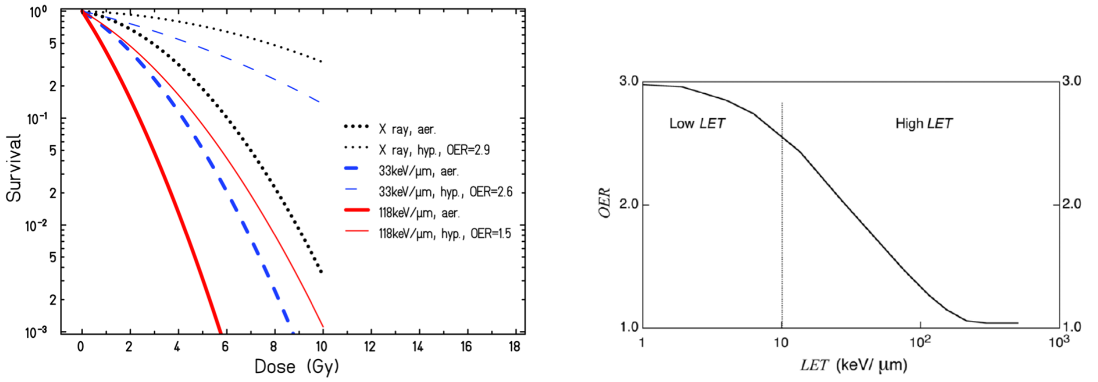

(a) **(b)**

Figure 1.28: (a) Influence of the oxygen level on cell survival for particles, i.e. carbon ions (red line) and X-rays (dashed line), with different LET[37] and (b) OER vs LET, where the vertical line divides the low ($LET < 10\mu m$) and high LET regions.[41]

The oxygen effect is probably related to indirect damage, which is significant for low LET radiations, in fact the presence of the molecular oxigen enhances the concentration of free radicals (H° and OH°) and ions (H^{+} and electrons) with consequent anomalous production of the peroxide of hydrogen (H_2O_2) which is the main responsible for cells damages. In case of high LET particles, the quantity of H_2O_2 produced is already very high, so a greater presence of O_2 is not crucial to generate severe lesions, and a lower dose is sufficient to stop cell replication capability.

Summing up, for heavy ions less dose is necessary to kill cancerous cells and no additional dose is needed to kill hypoxic radioresistant cells. However, this choice implies a significant increase of fragmentation, an effect that for hadrontherapy must be absolutely avoided in order not to incur collateral damage. This means that the right ion must be chosen with a compromise between the right OER-RBE and minimum fragmentation, therefore one can choose ions with $Z \leq 8$, first of all carbon, followed by oxygen and helium (currently under study).

1.4 Radiotherapy and Hadrontherapy

1.4.1 Photon interaction with matter

Photon is a massless particle with no electric charge, thus it is detected in an indirect way because crossing the material it produces a charged particle that is later detected interacting with matter. Moreover, fundamentally when a photon interacts, it is either completely absorbed or scattered through a relatively large angle, therefore this types of process are very different from the one of charged particles.

The attenuation of a photon beam as a function of the crossed thickness x is expressed through the *Lambert-Beer Law* (an exponential which depends on the characteristics of the material)[3], as:

$$\Phi(x) = \Phi_0 e^{-\mu x} \tag{1.26}$$

where Φ_0 is the initial number of particles in the incident beam per unit of surface and of time before the interaction with the target, and $\mu = \frac{\rho_T N_A}{A_T}\sigma_{tot}$ (cm^{-1}) is the attenuation coefficient and it can depend on the initial energy E, the charge Z and the target density ρ. The dependence on E is due to the fact that the cross section σ_{tot} of the processes itself depends on the energy.

Therefore, depending on their initial energy, they can interact at least in three different ways:

- the **photoelectric effect**[3] for low energies ($\sim KeV$ to ionization energy[7]). It is the one with the largest cross section and consists in the absorption of a photon with the right energy from an atom, with the consequent emission of an electron with a certain kinetic energy, which is the difference between the energy of the incoming γ and the binding energy of the atom. Therefore, since a free electron can't absorb a photon and also conserve momentum, this process always occurs on bound electrons, with nucleus absorbing the recoil momentum. Consequently, as shown in *Fig.1.29*, an e^- of the outer (M, L, K) shell fills the free shell emitting X-rays or sometimes the released energy is not emitted but absorbed by another outer electron (emission of Auger e^-).

  The cross section of the photoelectric effect decreases as the photon energy increases and increases as the atomic number of the material Z increases, as

---

[7] Ionization energy is the amount of energy a photon needs to extract an electron from an atom. It depends on the material.

[3]

$$\sigma_{photo} \propto \frac{Z^{4\div5}}{E_\gamma^{7/2}} \tag{1.27}$$

So it has a strong dependence on Z: this gives an explanation on the behavior of the cross section for different materials (see *Fig.1.32*).

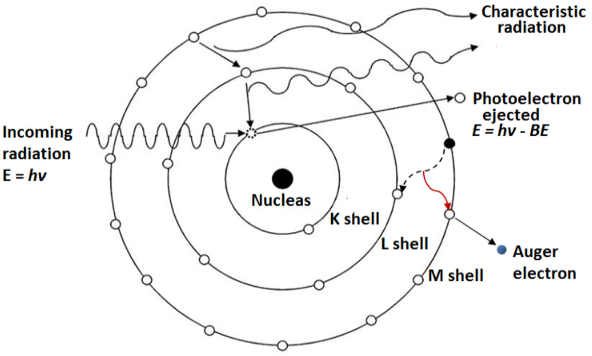

Figure 1.29: Sketch of the photoelectric effect.[42]

- the **Compton effect**[3] at around 1 MeV. A photon scatters with an almost free electron (generally electron lies in the outer shells of the atom, so it is less bound): there is no energy threshold for this process and the γ survives after the interaction (opposite situation compared to the previous case), thus this leads to scattered photon and electron with different energies and emission angles (see *Fig.1.30*). Moreover, considering the difference between the energy of incoming photon and the maximum kinetic energy of the outgoing electron, one can note two limit cases both depending on the photon initial energy: the *forward scattering* ($\theta = 0$) where we have the maximum energy of the photon in the final state, and the *backwards scattering* ($\theta = \pi$) where we have the maximum energy of the electron and minimum of the photon after the scattering event.

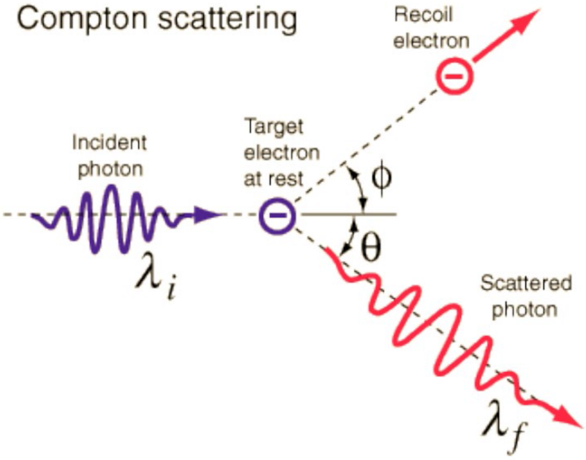

Figure 1.30: Sketch of the Compton effect.[42]

The Compton cross section depends weakly on the atomic number Z and for high energy values ($> 10\ MeV$) the process becomes completely negligible:

$$\sigma_{Compton} \propto \frac{Z}{E}. \tag{1.28}$$

- the **pair production**[3] at energies greater than 1 MeV. It involves the transformation of a photon into an electron-positron pair (see *Fig.1.31*). In order to simultaneously conserve energy and momentum, this can only occur in the presence of a third body, usually a nuclear Coulomb field, in the neighborhood. Moreover, to create the pair, the photon must have at least an energy of 1.022 MeV (i.e. energy threshold equals to $2m_e$).

  The emitted electron is normally absorbed in the material, losing its low energy by collisions, while the positron typically annihilates with an electron, producing a couple of photons.

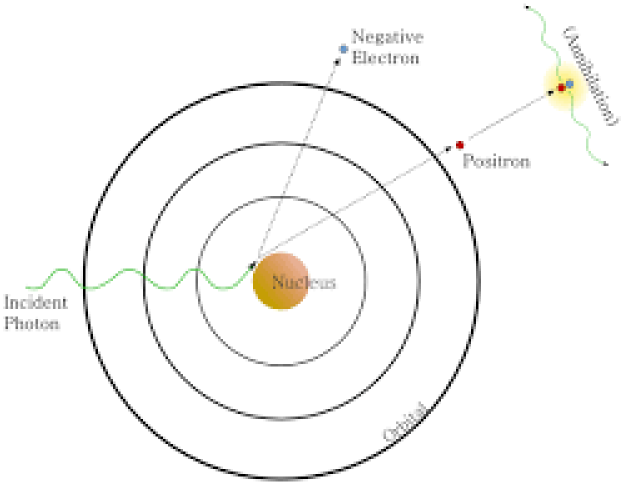

Figure 1.31: Sketch of the pair production.[42]

The pair production cross section is described by the following relation:

$$\sigma_{pair} \propto \frac{Z^2}{lnE} \tag{1.29}$$

thus, depends on Z squared and above an energy of some $GeVs$ it becomes almost constant.

We can summarize the three processes through a plot (see *Fig.1.32*) which shows the different cross sections as a function of the photon energy:

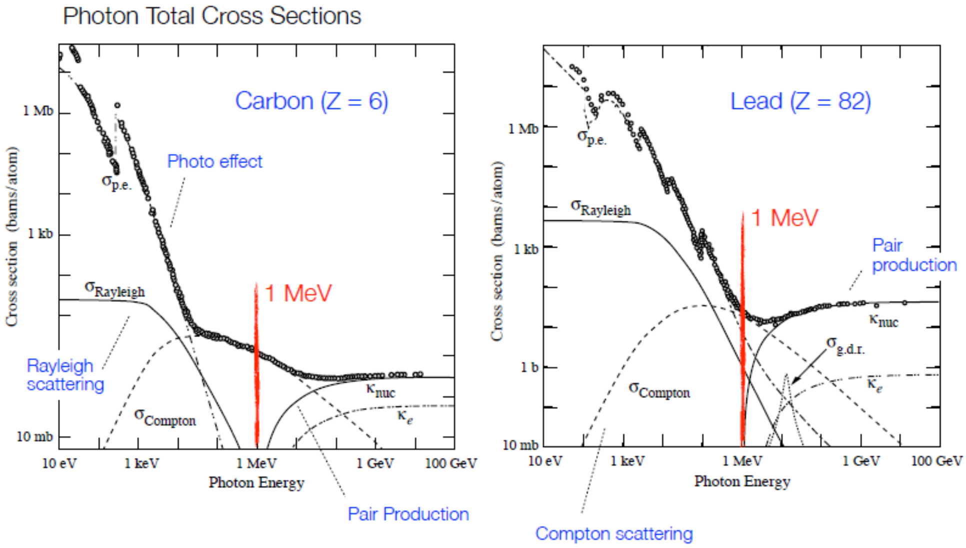

Figure 1.32: Plot of photoelectric, Compton and pair production cross sections for carbon and lead. At the particle therapy energies ($5 - 10\ MeV$) the photonuclear reaction and the Thomson-Rayleigh scattering are negligible. Every reaction has a region where it predominates over the others. For higher Z the photoelectric effect and pair production have higher probabilities to occur. Moreover, the cross section of photoelectric effect has a peculiar behavior: different peaks correspond to electrons extracted from the related shells and obviously, they are more evident in the lead plot.[3]

1.4.2 Advantages and Misadvantages of the Hadrontherapy

In conventional radiation therapy, beams of X-rays are produced by accelerated electrons and then delivered to the patient to destroy tumor cells. Sometimes treatment also involves the use of electrons, or gamma rays to damage or destroy cancer cells genetic material, hindering their ability to grow and multiply. Using a number of beams greater than one and delivering them from many angles, this kind of therapy tries to spare the surrounding healthy tissues (see *Fig.1.33*).

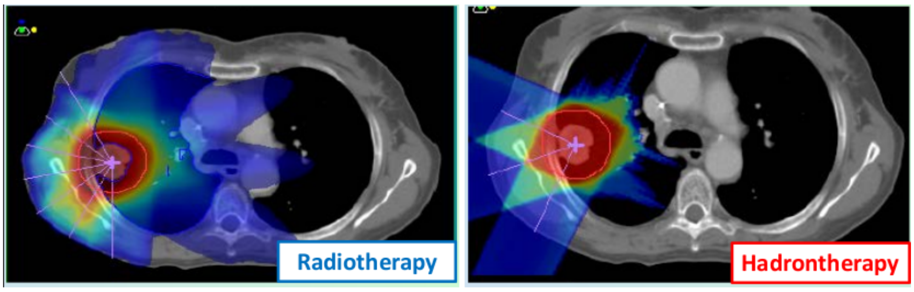

Figure 1.33: A comparison between the 7 fields-IMRT (*Intensity-Modulated Radiation Therapy*) at left and the hadrontherapy case with a proton beam at right. In blue the areas with less energy loss and in red the high dose region, where the tumor has to be placed. As one can note the hadrontherapy preserves healthy tissues better than the radiotherapy.[43]

However, inevitably some radiation dose is always deposited in the normal tissues due to the characteristic X-ray dose profile shown in *Fig.1.34*.

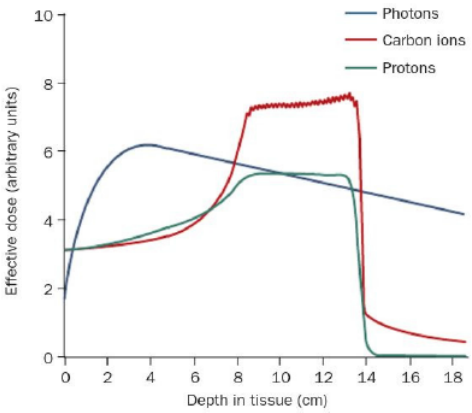

Figure 1.34: Photon beam (blue line) dose profile as a function of depth in tissue. Red and green line are the extended Bragg Peak (SOBP) for carbon ion and proton beams.[44]

As we have already described in Section 1.2.4, hadron beams have a different behaviour crossing the medium, i.e. a low release of energy before the Bragg Peak and the peak itself, where the particle loses almost its whole energy. Usually, it is located in the tumor region in order to hit with higher dose the disease.

Therefore, the main advantage is the possibility to treat deep-seated (sometimes near organ at risk) and mostly radioresistant tumors thanks to this particular mechanism of the energy release. Furthermore, the position of the Bragg peak can be known fixing the initial energy of the beam, so the therapy can be delivered with a higher precision than the radiotherapy in order to preserve the normal tissues.

It is useful to know that in the Treatment Planning Systems (TPS) the right dose range is decided each time on the tumor type, location and stage considering two important curves: the *Tumor Control Probability* (*TCP*) and the *Normal Tissue Complication Probability* (*NTCP)*. The first one is the probability of control the cancer region and the second one is the probability to have complication in the healthy cells. Both increase with the dose, as shown in *Fig.1.35*, thus finding the right dose range means finding the maximization of the TCP-NTCP curve in order to give a chance for the normal tissue to recover the radiation damage.

Unfortunately, in this context an important process has to be considered at the energy of hadrontherapy, i.e. the nuclear fragmentation (exposed in Section 1.2.5); the produced fragments must be taken into account in the planning of the treatment (TPS) because they also release energy in the patient. This problem is not easy to solve because of the lack of data on their cross sections. In conclusion, TPS are not complete for hadrontherapy.

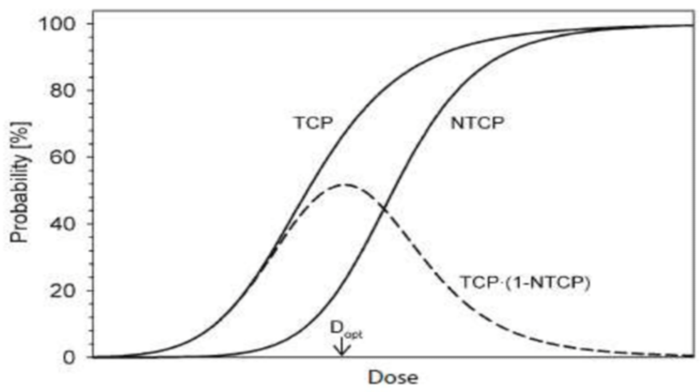

Figure 1.35: Dose-response curve for tumor control probability (TCP) and normal tissue complication probability (NTCP). The maximum probability for tumor control without normal tissue complications (dashed line) is reached at the optimum dose (D_{opt}).[45]

Lastly another misadvantage of hadrontherapy is the cost of cyclotrons and syncrotrons and the space they need (*Fig.1.36*). Infact, a IMRT treatment costs about 10.000 euros, while for the hadrontherapy the cost is almost millions of euros.

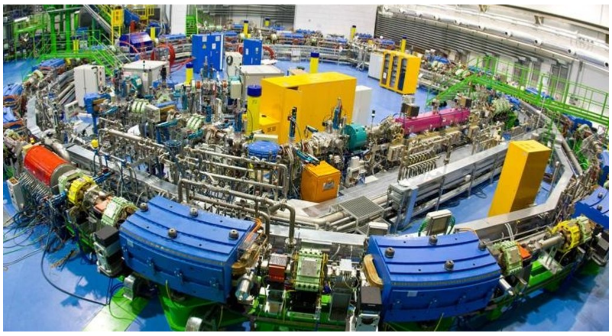

Figure 1.36: The CNAO syncrotrone which is used to accelerate carbon ion/p beams. It has a diameter of 25 m and it is placed in a bunker of 1600 m^2.[2]

Chapter 2

The FOOT Experiment (FragmentatiOn Of Target)

As already said in Chapter 1 particle therapy uses proton and ion beams ($Z \leq 8$) to treat deep-seated solid tumors, exploiting the favorable depth-dose deposition profile and RBE of charged particles. However, nuclear interactions with patient tissues can induce fragments production that must be taken into account in treatment planning. In detail, in proton treatments target fragmentation produces low-energy, short-range fragments depositing a non-negligible dose in the entry channel; in heavy ion beam treatments also long-range fragments due to projectile fragmentation are present releasing dose in tissues surrounding the tumor.

The *FOOT (FragmentatiOn Of Target) experiment* aims to study these processes to improve the nuclear interactions description in the next generation Treatment Planning Systems (TPS) softwares and hence the treatments quality.

2.1 Main goals

The FragmentatiOn Of Target (FOOT) project of INFN (Istituto Nazionale di Fisica Nucleare) is a nuclear physics experiment whose purpose is to experimentally investigate both target and beam fragmentation and measure the differential cross section of these nuclear inelastic reactions in the energy range of charged particle therapy (CPT, up to 250 MeV for protons and 400 MeV/u for ^{16}O and ^{12}C). Another main objective of FOOT is the space radioprotection: this means measuring fragmentation cross sections for helium, carbon and oxygen beams at higher energies (about 700 MeV/u), since these high energy nuclei are commonly present in the Galactic Cosmic Rays (GCR) spectrum[46].

Thus, accurate measurements of fragments production spectra are of great importance both to improve the quality of nuclear models currently implemented in the MC simulations inside TPS and to estimate the astronauts dose exposure in future space missions far from Earth in order to design proper shielding systems. As result, a new generation of biologically oriented TPS (BioTPS), based more on biological effect rather than dose or RBE-weighted dose could eventually be developed.

In this framework, the most challenging goal of the FOOT experiment is the characterization of target fragmentation processes induced by proton beams, which are particularly relevant in protontherapy. Since target fragments produced have a very short range ($\sim$ tens of μm), as in Section 1.2.5, their detection is extremely tricky because they can't escape from the target material. In Section 2.3 the procedure that will be adopted to overcome this difficulty is described in details.

In order to carry out these planned measurements FOOT has been designed to be a fixed target experiment and it consists of 2 different setups related to the identification (i.e. atomic number Z and number of mass A fragments identification) of different nuclear fragments:

- A setup based on electronic detectors and a magnetic spectrometer for heavy fragments ($Z \geq 3$)[1].
- An emulsion spectrometer coupled with the interaction region of FOOT, dedicated to light fragments ($Z \leq 3$).

As further specified, the need for 2 setups is due to the difficulty in reaching a good balance between the angular acceptance[2] and a limited size for the tracking system.

In fact, FOOT aims to be a portable system (capable of performing measurements on both projectile and target nuclear fragmentation events) because the previous cited beam particles and energies are provided by different European facilities, which mainly are:

- CNAO (Centro Nazionale di Adroterapia Oncologica) in Pavia (Italy), where proton and ^{12}C ion beams at CPT energies are available.
- Heidelberg Ion Therapy (HIT) center in Germany, with ^{4}He, ^{12}C and ^{16}O beams for CPT.
- GSI in Darmstadt (Germany), which can provide the same ion beams of the HIT center.
- Proton Therapy center in Trento (Italy).

In the next sections the details of the FOOT experiment will be presented, giving special importance to the experimental requirements needed to measure the fragmentation cross sections.

2.2 Experimental requirements

Since the most strict requirements come from PT, the accuracy of the FOOT measurements is dictated by the PT radiobiologists needs. To improve the RBE evaluation it is essential to measure the fragments production cross sections with a maximum relative uncertainty of the order of 5% through the electronic detector setup. This resolution has been fixed thanks to previous studies with Monte Carlo

---

[1] The heavy fragments setup has been used for the particles identification in my thesis work.

[2] Due to kinematic reason, fragments with $Z > 2$ are forward emitted within a cone of 10° with respect to the beam axis, whereas light fragments are also scattered at larger angles. They are usually emitted up to 70°.

simulations that have shown negligible improvements of TPS for higher uncertainty values on σ_{inel} data. These measurements will be then implemented in treatment planning softwares.

To guarantee the requested accuracy, the detector performances that FOOT needs to achieve in heavy fragments identification are[46]:

- Momentum resolution $\sigma(p)/p$ of about 5%.
- Time-Of-Flight resolution σ_{TOF}/TOF of the order of 100 ps.
- Kinetic energy resolution $\sigma(E_k)/E_k \sim 2\%$.
- Energy deposition resolution $\sigma(\Delta E)/\Delta E$ at the level of 2%.

These results need also to be achieved in a system as compact as possible. Therefore, the final electronic detector setup have a longitudinal dimension of $1.5 - 2$ m, which allows it to be placed in all the treatment rooms of the aforementioned CPT facilities. The isotopic identification of particles can be fulfilled in different ways due to the redundancy of FOOT: the characteristics of the fragments are determined in different ways (as will be shown in the next chapter) to limit as much as possible the systematic errors in the calculations. In particular, for the charge identification, the main goal is to perform an accuracy of 2-3%, whereas for the mass A, it has to be better than 5%.

2.3 Inverse kinematics approach

The experimental detection and measurement of the target fragmentation induced by protons is extremely difficult because of the low energy and short range of the produced fragments. Considering a 180 MeV protons beam impinging on a water target, the range of the predicted fragments is of the order of micrometers (see *Fig.2.1*).

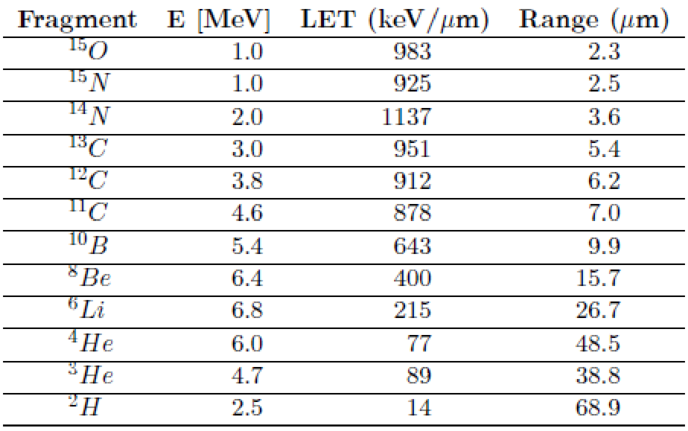

Fragment	E [MeV]	LET (keV/μm)	Range (μm)
^{15}O	1.0	983	2.3
^{15}N	1.0	925	2.5
^{14}N	2.0	1137	3.6
^{13}C	3.0	951	5.4
^{12}C	3.8	912	6.2
^{11}C	4.6	878	7.0
^{10}B	5.4	643	9.9
^{8}Be	6.4	400	15.7
^{6}Li	6.8	215	26.7
^{4}He	6.0	77	48.5
^{3}He	4.7	89	38.8
^{2}H	2.5	14	68.9

Figure 2.1: Expected average physical parameters (E, LET, Range) for different fragments produced by a 180 MeV proton beam in water.[46]

Summing up, a fragment produced by a proton projectile, can leave the target and thus it can be detected only if it has been produced at a distance less than few micrometers from the exit surface of the target material. Otherwise the fragment deposits all its energy locally, being trapped inside the target and invalidating any detection attempt. Furthermore, even a thinner target ($\sim \mu m$) would not solve the issue because it would imply mechanical problems since it is difficult to handle such a fragile target without risking any damage and most of all, the interaction rate would be extremely reduced implying very long data acquisitions.

For this reason an *inverse kinematic approach* is applied in FOOT: instead of shooting a proton beam onto a tissue-like (carbon or oxygen, which are the main constituents of human body) target, tissue-like nuclei will be accelerated to impinge on a hydrogen enriched target. As a result, if the beams have the same kinetic energy per nucleon, the two situations maintain the same interaction probability and they are simply linked by a change of reference frame, i.e. a Lorentz transformation[3]. Consequentially the only difference is that, in inverse kinematics, secondary fragments will have boosted energy and longer range, so that they will be able to easily escape the target and be detected by the FOOT apparatus[47].

Nevertheless this strategy requires an emission angle measurement with a resolution of the order of few *mrad* in order to correctly apply the Lorentz boost. Therefore, a good accuracy in determining the trajectories of both projectile and fragments is required, and also the MCS of any particle inside the beam must be kept well below the *mrad*. In this way, the only constraints on target thickness are determined by MCS and secondary fragmentations. To maintain these effects as low as possible and a high interaction rate, a severe limit on the allowed thickness of the target has to be set of the order of 2-5 mm and a density of the order of 2-5 g/cm^2 (lowering $\sim 10^{-2}$ the probability of secondary fragmentation)[46].

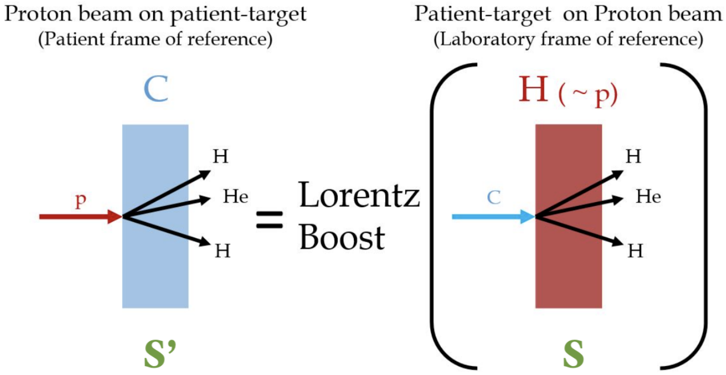

Figure 2.2: Scheme of the Lorentz transformation.

Now, as shown in *Fig.2.2*, if we consider S as the laboratory frame, the incident heavy ions beam is moving along z at a constant velocity β and impinges on the

---

[3] A Lorentz transformation is a linear transformation that converts the coordinates between two reference frames moving at a relative constant velocity to each other. This mathematical tool may also include a rotation of space but in the absence of rotations the transformation is called the Lorentz boost.

stationary hydrogen target while in S' frame, i.e. the "patient frame", the target and the projectile material are switched, meaning that the beam is made of protons and the target is tissue-like. So, the proton 4-momentum components in the S' frame are given in matrix format by the following relation:

$$\mathbf{P'} = \mathbf{\Lambda P} \tag{2.1}$$

where $\mathbf{P'} = (E/c, \mathbf{p'})$ and $\mathbf{P} = (E/c, \mathbf{p})$ are the ions 4-momentum in S' and S respectively, while $\mathbf{\Lambda}$ is a 4×4 matrix, expressed in case of the beam in the z direction, as:

$$\begin{pmatrix} E'/c \\ p'_x \\ p'_y \\ p'_z \end{pmatrix} = \begin{pmatrix} \gamma & 0 & 0 & -\beta\gamma \\ 0 & 1 & 0 & 0 \\ 0 & 0 & 1 & 0 \\ -\beta\gamma & 0 & 0 & \gamma \end{pmatrix} \begin{pmatrix} E/c \\ p_x \\ p_y \\ p_z \end{pmatrix} = \begin{pmatrix} \gamma E/c - \beta\gamma p_z \\ p_x \\ p_y \\ -\beta\gamma E/c + p_z \end{pmatrix} \tag{2.2}$$

Thus, the inverse Lorentz trasformation will be:

$$\mathbf{P} = \mathbf{\Lambda}^{-1}\mathbf{P'} \tag{2.3}$$

where the inverse matrix $\mathbf{\Lambda}^{-1}$ is simply equal to $\mathbf{\Lambda}$ with a change of the β sign:

$$\mathbf{\Lambda}^{-1}(\beta) = \mathbf{\Lambda}(-\beta). \tag{2.4}$$

2.4 Target material

The targets composition has been set according to the human body structure, i.e. carbon, oxygen and hydrogen have been selected as the main targets of interest. The choice of using composite materials is imposed by the large amount of technical difficulties introduced by a pure gaseous hydrogen target, such as the low rate due to the low density and mostly safety reasons. Therefore in the therapy centers where the experiment will be run, the measurements will be performed with two types of target: one made of carbon and the other made of a hydrogenated material, i.e. polyethylene (C_2H_4). The hydrogen cross sections will be then extracted indirectly, using the results obtained from two different acquisitions and subtracting the respective data, as in the following formula[46]:

$$\sigma(H) = \frac{1}{4}(\sigma(C_2H_4) - 2\sigma(C)) \tag{2.5}$$

Then, one can apply the same procedure to the differential cross section:

$$\frac{d\sigma}{dE_k}(H) = \frac{1}{4}\left(\frac{d\sigma}{dE_k}(C_2H_4) - 2\frac{d\sigma}{dE_k}(C)\right) \tag{2.6}$$

$$\frac{d\sigma}{d\theta}(H) = \frac{1}{4}\left(\frac{d\sigma}{d\theta}(C_2H_4) - 2\frac{d\sigma}{d\theta}(C)\right) \tag{2.7}$$

This approach has been validated through simulations on both the direct and the subtraction method. The comparison is reported in *Fig.2.3*, that shows the energy differential cross section of a 200 MeV/u ^{12}C beam on hydrogen target in inverse kinematics obtained from (2.6) relation and with the direct measurements. The results from the two estimations are in good agreements, thus validating the combination method.

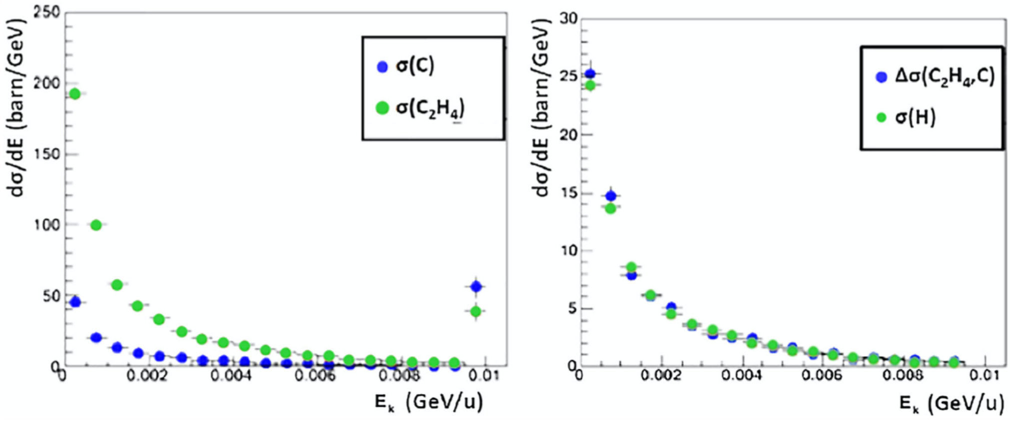

Figure 2.3: FLUKA simulations on the reconstruction of energy differential cross sections of C fragments in inverse kinematics for a ^{12}C beam on C and C_2H_4 target (left panel) and on H obtained either by subtraction or directly on H target (right panel).[48]

Nevertheless, a possible problem with this technique is that the uncertainties on indirect cross sections are calculated as the quadratic sum of the two single target measurements, meaning that they can become quite large.

The same method can be also adopted to study the cross sections on oxygen target. However, in this case a PMMA (PolyMethyl MethAcrylate, $(C_5O_2H_8)_n$) target has to be used, since it is composed of carbon, hydrogen and oxygen.

2.5 Electronic Apparatus for heavy ion particles detection

The FOOT electronic detector setup is used to the identification of nuclear fragments heavier than ^6Li. The geometrical acceptance of the system takes into account the small emission cone of particles with $Z \geq 3$ which are mainly emitted within about 10 degrees from the beam direction. This value was found through a preliminary study with MC codes, leading to the results shown in *Fig.2.4*. As already mentioned, this requirement has to match the wider angular aperture of light fragments and the need to have an apparatus of limited size (longitudinally, the whole setup can be contained in about $\sim 1.5\ m$). Therefore the FOOT experiment is composed by two complementary setups: one based on a *magnetic spectrometer* and the other exploiting the *emulsion chamber* capabilities.

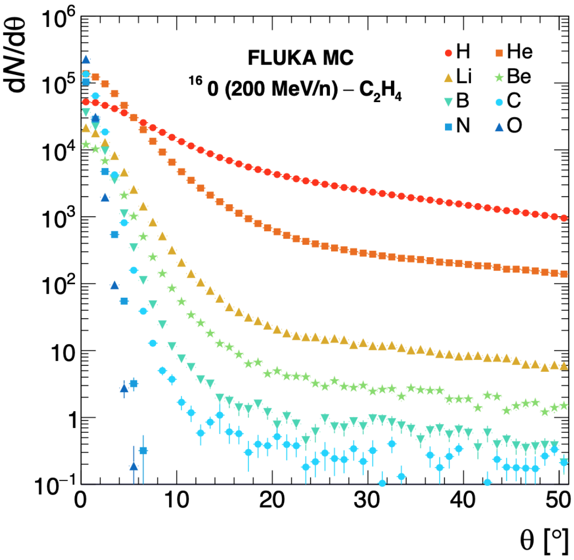

Figure 2.4: MC calculation of the angular distributions of different fragments produced by a 200 MeV/u ^{16}O beam impinging on a 2 mm thick polyethylene target.[49]

Another main factor which affects the detector geometry is the angular separation between two fragments emitted in the same events, it rules the granularity of the system.

Starting from the incident beam direction a schematic view of the electronic setup and the related features are reported in *Fig.2.5* and *2.6*. In detail, the whole apparatus can be divided in 3 main regions: an upstream (pre-target) region, a magnetic spectrometer and a downstream region.

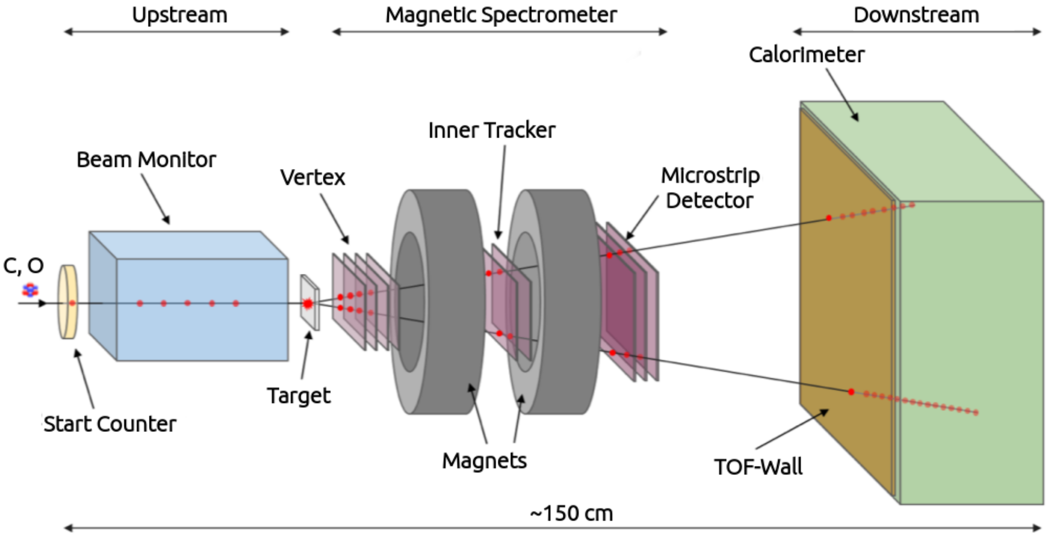

Figure 2.5: Sketch of the FOOT electronic setup (not in scale) for the measurements of heavy ion fragments.[47]

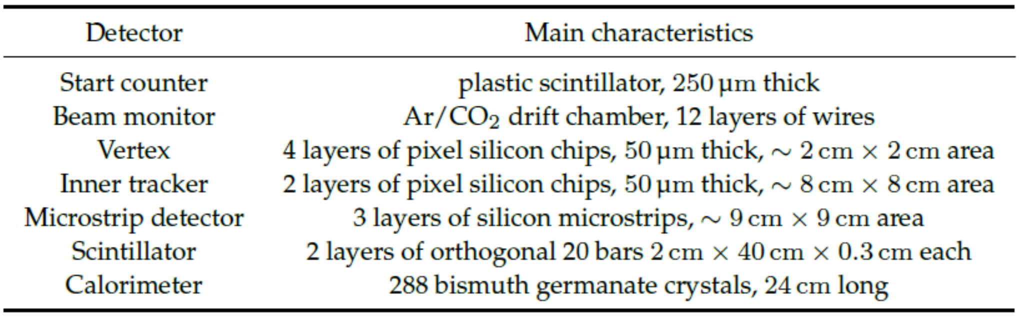

Detector	Main characteristics
Start counter	plastic scintillator, 250 μm thick
Beam monitor	Ar/CO_2 drift chamber, 12 layers of wires
Vertex	4 layers of pixel silicon chips, 50 μm thick, ∼ 2 cm × 2 cm area
Inner tracker	2 layers of pixel silicon chips, 50 μm thick, ∼ 8 cm × 8 cm area
Microstrip detector	3 layers of silicon microstrips, ∼ 9 cm × 9 cm area
Scintillator	2 layers of orthogonal 20 bars 2 cm × 40 cm × 0.3 cm each
Calorimeter	288 bismuth germanate crystals, 24 cm long

Figure 2.6: Main characteristics of the detectors.[47]

2.5.1 Upstream region

The upstream region is designed to monitor the primary beam particles and it is composed by the first two detectors encountered by the beam: the Start Counter and the Beam Monitor.

- **Start Counter**

The Start Counter (STC) is a thin plastic scintillator, characterized by a rise time of 700 *ps* and a light yield of 10000 $photon/MeV$, and it is the first detector encountered by the beam. The STC has an active area of 5×5 cm^2 and it is placed $20 - 30$ cm before the target. The light produced in the scintillator is collected laterally by 48 Silicon Photomultipliers (SiPMs), 12 per side. Its thickness (250 μm) is chosen in order to minimize its impact on the beam avoiding possible fragmentations events within the detector and to maximize the light output while keeping a good time resolution ($60 - 70$ ps). *Fig.2.7* shows a technical drawing of the scintillator foil and its aluminum frame.

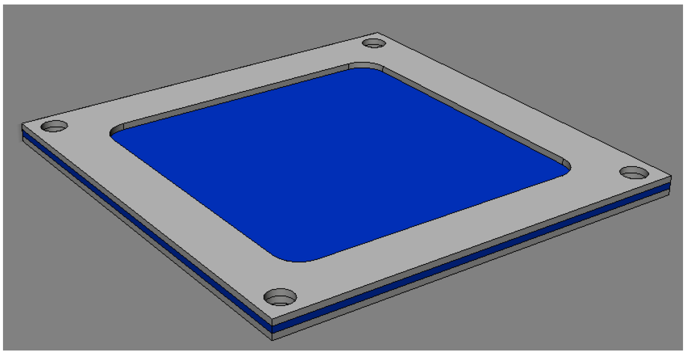

Figure 2.7: Drawing scheme of a Start Counter.[46]

The STC main purposes are to provide the trigger signal for event acquisition, to monitor the primary particles rate and to give the time of flight measurement in combination with another scintillator detector placed downstream the target. Therefore, since the measurement of TOF is crucial to achieve the desired mass identification resolution, the STC time resolution has to match the time resolution of this last scintillator detector.

- **Beam Monitor**

The Beam Monitor (BM) is an Ar/CO_2 (80/20%) gas mixture-drift chamber (see *Fig.2.8*), composed by 12 layers of alternating horizontal and vertical wires. Each plane consists of 3 rectangular drift cells of $16 \times 11\ mm^2$ with the long side perpendicular to the beam direction. Consecutive layers are also staggered by half a cell to avoid left-right ambiguities in track reconstruction. The total dimensions of the BM are $11 \times 11 \times 21\ cm^3$.

The aim of the BM is to accurately measure the initial position and direction of primaries, fundamental for particle tracking and rejection of pre-target fragmentation events in STC. In particular, the knowledge of the impinging point of the ion beam on the target, is a crucial information needed to address the pile-up ambiguity in the slow VTX detector (readout time = 187 μs). In fact the BM read-out time, of the order of 1 μs or less, is fast enough to ensure that tracks belonging to different events cannot be mixed. In addition, since the momentum of primaries is important for the Lorentz boost, the BM should achieve a resolution of about 100 μm for position measurements and about $mrad$ for angular data. Furthermore, since it is placed between the STC and the target, the BM was also designed as a drift chamber in order to minimize the MCS, thus its low impact on the primaries thanks to its low density material.

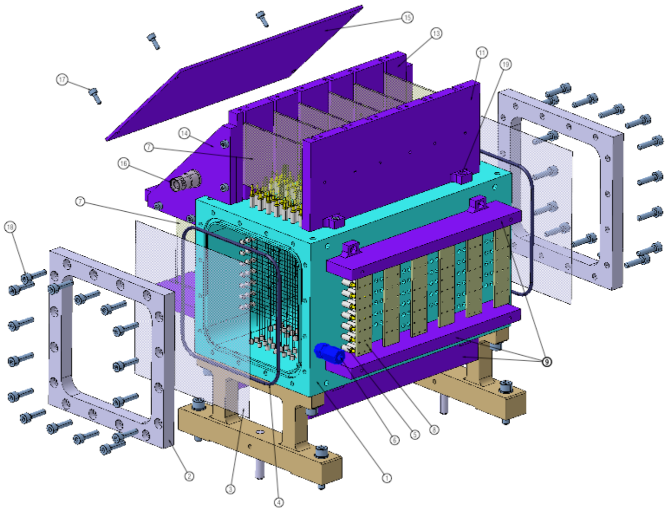

Figure 2.8: Technical drawing of the BM drift chamber.[46]

2.5.2 Magnetic Spectrometer

A key element for the FOOT experiment is its tracking system, represented by the magnetic spectrometer placed right after the vertex detector which includes three measuring stations alternated with two permanent magnets. In detail this device consists of two pixel detectors, a microstrip detector and 2 permanent magnets that provide the required magnetic field. This section of FOOT is dedicated to the evaluation of the particles momentum, obtained by measuring the bending of fragments trajectories inside the magnetic field. Moreover, the spectrometer will also give information about the interaction point of particles inside the target.

The overall design of the spectrometer is mainly constrained by its portability and the requested momentum resolution. Concerning the portability, this requirement forces the choice of permanent magnets in a limited sizes and weight, while momentum resolution has to be at the level of few percent. The accuracy of p measurements increases as transverse momentum variations Δp_T become larger (thus, particles deflection). For a particle of charge q moving in a magnetic field B of length L, Δp_T is given by[8]:

$$\Delta p_T = q \int_0^L B dl \tag{2.8}$$

This means that p resolution depends mainly on B and L parameters.
In *Fig.2.9* a schematic view of the magnetic spectrometer is shown.

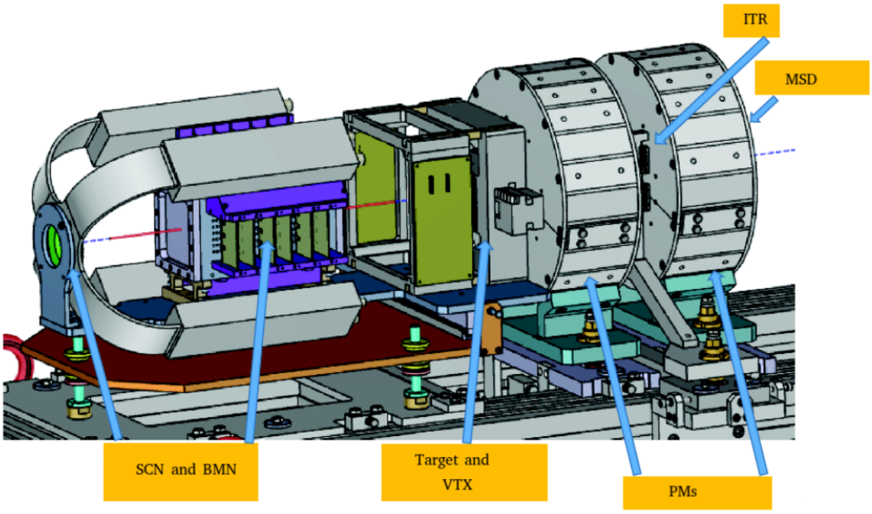

Figure 2.9: Design of the FOOT Magnetic Spectrometer.[47]

- **Permanent Magnet**

The magnetic field is provided by two Permanent Magnets (PMs) in *Halbach configuration* (*Fig.2.10*): in each of them twelve blocks of magnets (Sm_2Co_{17}, Samarium-Cobalt) are arranged in a annular configuration. An external aluminum case preserves the blocks arrangement. The particular PM blocks material has been chosen by considering the radiation resistance capability, in fact, in the FOOT setup the PMs are severely exposed to various radiations, in particular neutrons and light ions (mainly protons and He ions). Radiation exposure can degrade and damage the PM material, thus altering the produced field.

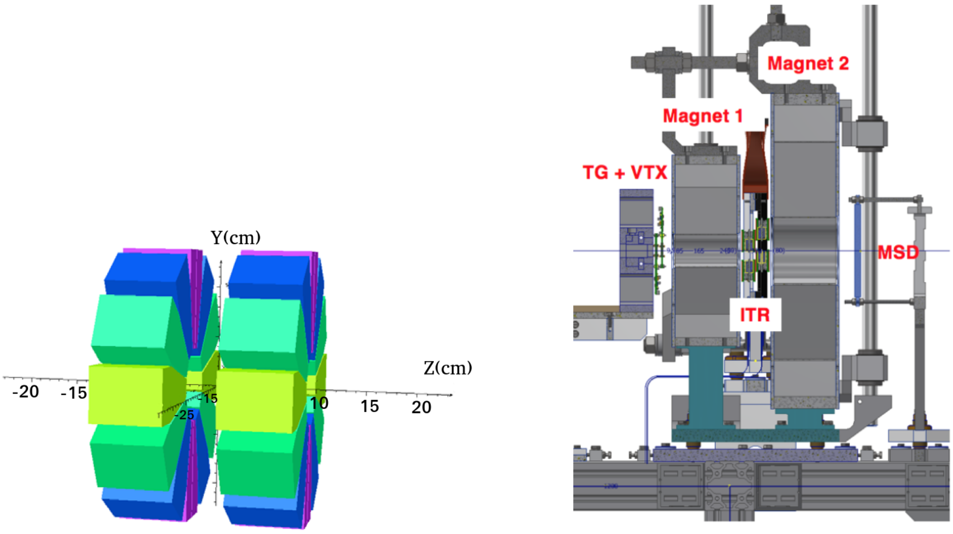

(a) **(b)**

Figure 2.10: Technical design of the two magnets in Halbach configuration. The center of the magnetic system coincides with the center of the reference frame[46],[49].

The Halbach configuration has the advantage of a nearly uniform magnetic field in the internal hole (see *Fig.2.11(a)*). Furthermore, in order to perform an additional momentum measurement the solution with two permanent magnets with inside an intermediated station has been preferred but this geometry causes a double Gaussian trend (see *Fig.2.11(c)*) of the magnetic field along the z axis.

Precisely, the magnetic field increases with the external cylinder radius while decreases with the gap radius, as:

$$B \propto ln\left(\frac{R_{out}}{R_{in}}\right) \tag{2.9}$$

At present, the permanent magnets are still being optimized. Using an internal and external radius equal to $\sim 4\ cm$ and $\sim 14\ cm$ respectively, the obtained B field has an expected intensity of the order of $0.8 - 0.9\ T$ that is compatible with the requirements sets for FOOT. In fact, the two different magnet dimensions have been mostly chosen in order to match the final momentum resolution producing the needed $(B \times L)$ and at the same time have an angular acceptance of 10° for the emitted fragments. Moreover, also the design of the three measuring stations has been selected in order to minimize

MCS and secondary fragmentations, while keeping a good p resolution and geometrical acceptance.

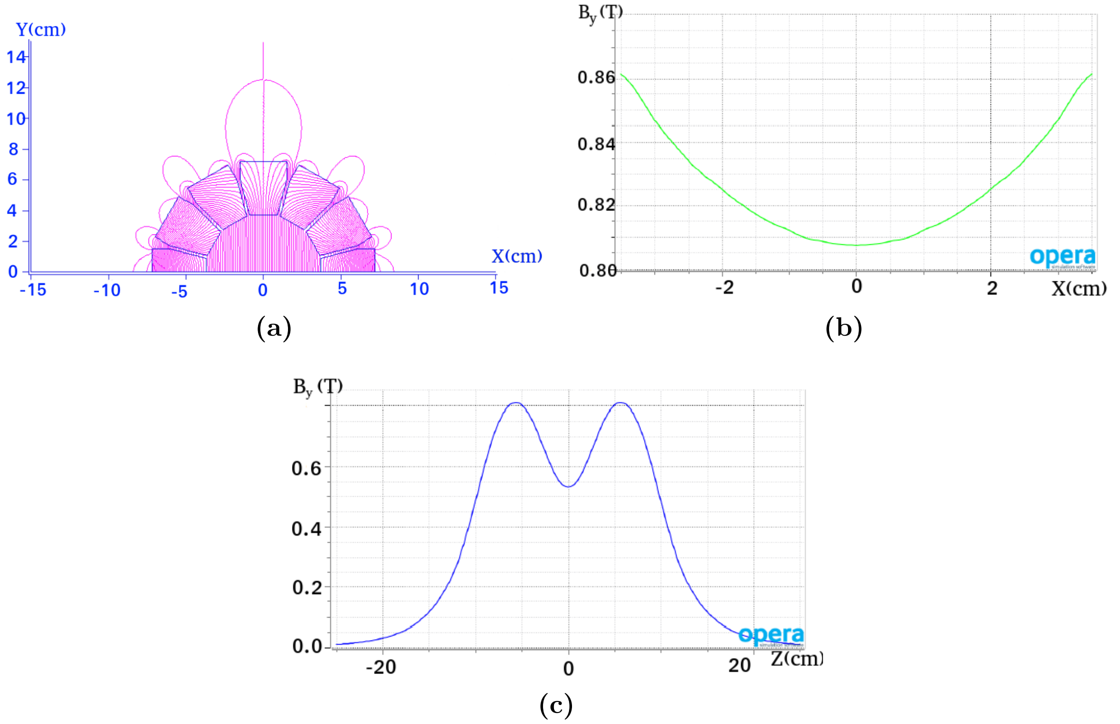

(a) **(b)**

(c)

Figure 2.11: (a) Simulation of the magnetic field lines in $x - y$ plane, which is comparable to the one achievable with a dipole magnet. (b) B_y as a function of x (at $y = 0$ and z equals to the center of one of the PMs), it is significantly higher than the other two components, which are approximately negligible inside the PMs hole. (c) The double gaussian trend, due to the presence of the inner tracker between the two PMs, can be seen in figure[46].

- **Vertex detector**

The Vertex (VTX) is the first detector of the tracking system (*Fig.2.12(b)*), placed at ~ 0.5 cm from the target and it is divided in two substations at a distance of 10 mm from each other. Each substation is made of two planes at a distance of 2 mm, made of MIMOSA28 (M28) chips (*Fig.2.12(a)*), developed by the Strasbourg CNRS PICSEL group. The M28 comes from the family of CMOS Monolithic Active Pixel Sensors (MAPS), already in use in X-ray imaging and charged particle detection. Each sensor includes 928 (rows) $\times$ 960(columns) pixels of 20.7 μm pitch, corresponding to a total active area of 20.22×22.71 mm^2, and it is 50 μm thick. With this setup, the VTX has a geometrical acceptance of ~ 40 degrees with respect to the target.

The main goal of the VTX is to identify the vertices of the particles trajectories, i.e. the point where primaries interacted with the target. Particles passing through this detector produce a signal inside different pixels, whose number is proportional to their energy loss, so their hit positions on the planes can be reconstructed through dedicated reconstruction clusterization algorithms. The accuracy required for these values is at the level of few μm. In addition, it also contributes to the measurement of the particles momentum in the magnetic field in combination with the other devices of the magnetic spectrometer.

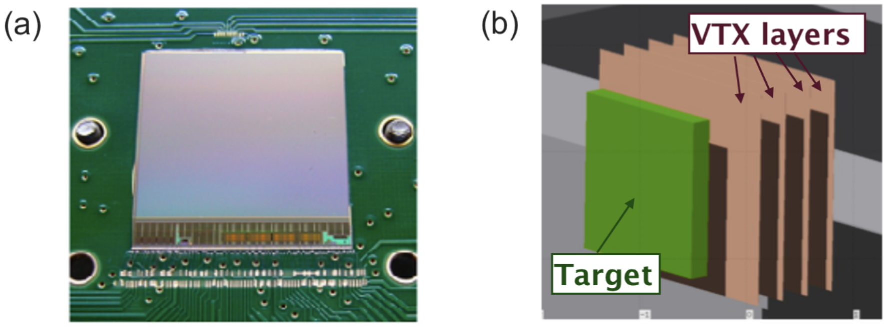

Figure 2.12: (a) Picture of a M28 chip, where the gray box in the middle represents the sensor. (b) Scheme of a Vertex detector.[46]

- **Inner Tracker**

The FOOT Inner Tracking (IT) system is placed between the two permanent magnets, at a distance of $\sim 20\ cm$ from the target, as in *Fig.2.13*. It covers an area of about $8\ cm \times 8\ cm$ according to the emission angle distribution that is broader here than in the VTX. The detector is composed by two planes of 8 M28 sensors (50 μm thick) each. The latters are glued in modules and bonded on a kapton FPC (Flexible Printed Cable) and they have a total thickness of $\sim 100\ \mu m$. To maximize the active surface, the two planes are also staggered laterally to avoid the superposition of dead areas between chips. Note that, even if the IT is placed inside the magnetic field (see *Fig.2.10(b)*), the performance of M28 chips should not be significantly affected. The IT purpose is to measure the direction and transverse position of particle tracks.

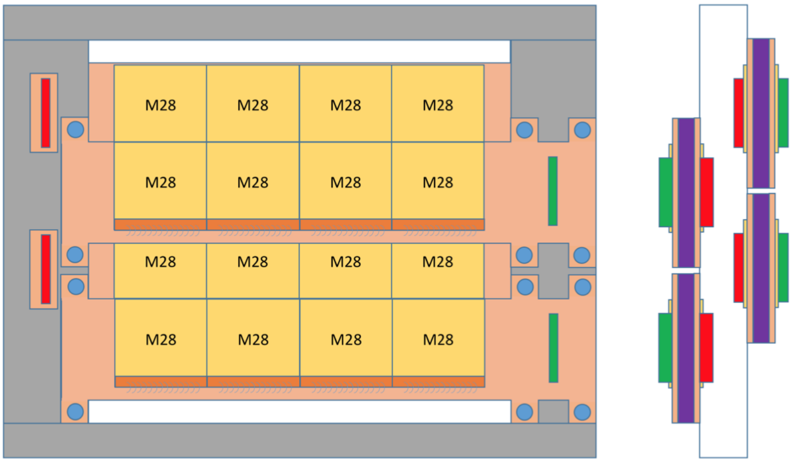

Figure 2.13: Schematic view of the Inner Tracker.[46]

- **MicroStrip Silicon Detector**

  The MicroStrip Silicon Detector (MSD) represents the final section of the tracking system (*Fig.2.14*), placed at about 35 cm from the target. Tracking of fragments downstream the magnetic volumes is essential for the measurement of momentum and it is also fundamental to match the reconstructed tracks with the hits in the TOF scintillator and calorimeter. It can also provide a measure of the energy released dE/dx, which can be used to obtain a redundant measure of the charge of impinging particles (the main detector employed for charge identification is obviously the TOF scintillator).

  Concerning its features, the detector consists of three 150 μm thick layers of alternatively orthogonal silicon microstrips. Each layer has an active area of $9 \times 9\ cm^2$, enough to cover the 10° of the acceptance, and a microstrip pitch of 125 μm. Thus, a spatial resolution of $< 35\ \mu m$ can be achieved.

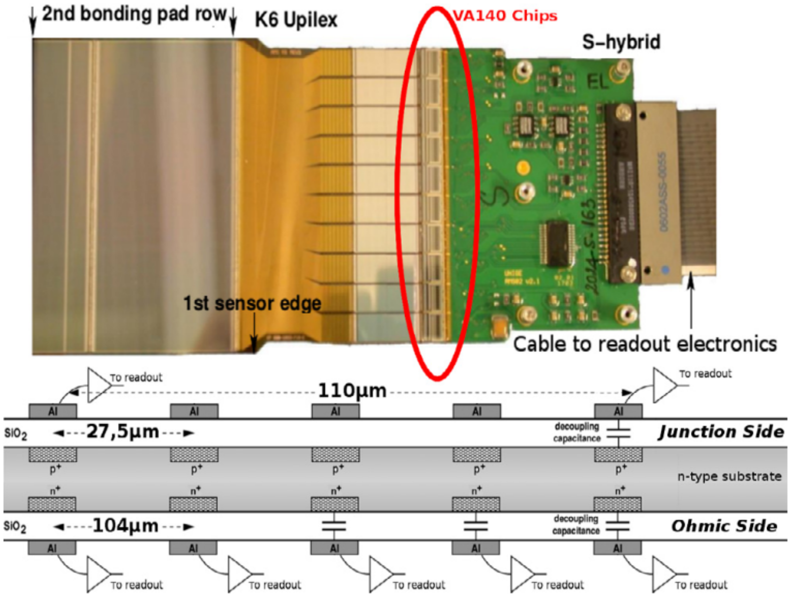

Figure 2.14: The sensor used in the experiment (top) and its readout scheme (bottom)[50].

Furthermore, when the FOOT apparatus is set for higher beam energy (700 MeV/u), the system ITR-PM and the MSD are shifted forward ($\sim$ 30 cm and $\sim$ 60 cm respectively), in order to maintain the same angular acceptance. Since the detectors and PMs transversal dimensions do not change, the longitudinal expansion of the magnetic spectrometer implies a decrease of the angular aperture. However, this is not an issue because, at high energy, heavy fragments are even more forward peaked, therefore they are emitted at smaller solid angles.

2.5.3 Downstream region

The last part of the FOOT electronic setup is composed by a plastic scintillator wall (ΔE-TOF detector) and a calorimeter. As for the previous detectors, their distance with respect to the target position is moved more forward when the experiment is set in the space radioprotection energy range, in order to improve the resolution on the fragments velocity β.

- **Plastic scintillator wall (TOF-Wall (TW) detector)**

The TOF-Wall (TW) detector is composed of two layers of plastic scintillator bars arranged orthogonally and wrapped with a thin layer of aluminum that minimize the light loss, with a covered total active area of 40 × 40 cm^2, placed at approximately 1 m from the target-VTX region. Each layer consists of 20 bars in order to match the angular aperture ($< 10^{\circ}$) of the heavier fragments at the distance of the detector from the target. Each bar, coupled to 4 silicon photomultipliers (SiPM) at the two edges, is 0.3 *cm* thick, 2 *cm* wide[4] and 40 *cm* long. Moreover, the thickness of the bars is chosen as a trade-off between the amount of scintillation light produced in the bar (resulting in a better timing $\sim$ 50 *ps* and energy resolution $\sim 3-5\%$), which increases with the deposited energy and therefore with the bar thickness, and the systematic uncertainty induced on the ΔE-TOF measurement by secondary fragmentation that would affect the particle identification and tracking. *Fig.2.15* shows a schematic view of the ΔE-TOF detector.

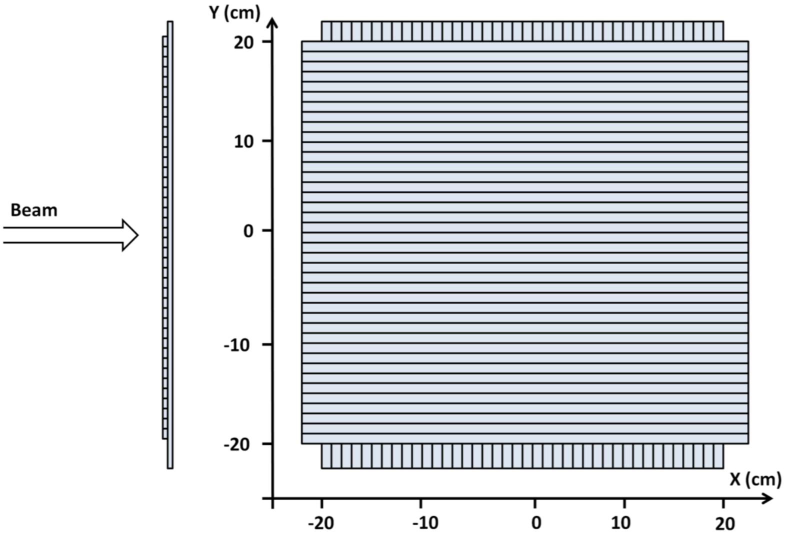

Figure 2.15: Schematic view of the TOF wall scintillator detector[46].

These kind of devices are particularly advantageous because they are fast and can be easily shaped based on custom requirements.

The TW main purposes are to measure the fragments energy loss (ΔE) and to provide the stop of the time of flight measurements. Since the TOF is inversely proportional to the particles velocity β, it is possible to evaluate the fragments atomic number Z from the Bethe-Bloch formula (Eq.1.1) using the ΔE and β measurements.

- **Calorimeter (CALO)**

The FOOT calorimeter is the most downstream detector. It is composed by 288 BGO (Bismuth Germanate) crystals, chosen for their high density and light yield, with a truncated pyramid shape (see *Fig.2.16(a)*), and a length of 24 *cm* with a front and outer face area of about 2×2 cm^2 and 2.9×2.9 cm^2 respectively. These crystals are arranged in a pointing geometry (see

---

[4] A bar width of 2 *cm* limits the double fragments events in the same bar below a few percent level. This choice is also useful because the width matches the transversal dimension of the cells of the calorimeter, which the TW detector is mechanically coupled to.

Fig.2.16(b)) and they are then read-out by 8 *mm* × 8 *mm* Silicon PhotoMultipliers (SiPMs). The segmentation of the calorimeter is determined by the average angular separation of the traces and the distance of the CALO from the target. In fact the fragments angular separation increases as the distance from the target increases. The expected energy resolution ranges between $1-3\%$ depending on the fragment type and overall energy.

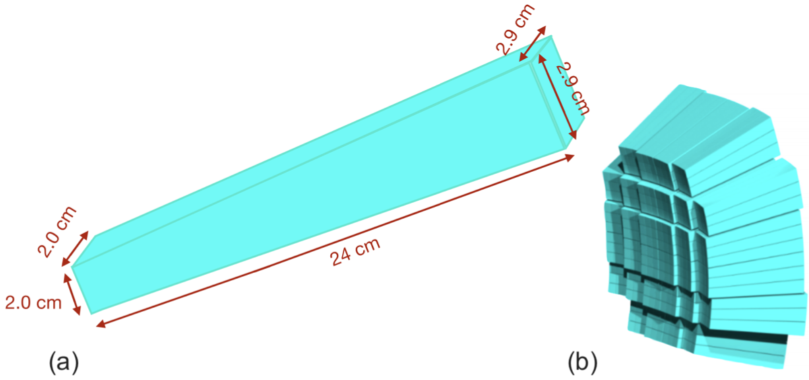

Figure 2.16: (a) The structure of a BGO crystal. (b) The fully assembled FOOT calorimeter detector.[46]

The CALO is designed to measure the kinetic energy of fragments produced in the target. The upper bound of the fragments energy range is defined by the beam energy, while the lower bound is set by the intensity of the magnetic field. Moreover, FOOT operates in a range in which fragments are below the energy threshold that triggers a shower in a calorimeter. Therefore, the mechanisms for energy loss will be driven by the electromagnetic interaction and nuclear interactions. However, a possible problem is the significant production of neutrons, which can then escape the calorimeter. BGO can partially limit this effect since it has also a high neutron capture cross section ($\sigma = 1.47$ *barn*)[51], but a systematic underestimation of the measured kinetic energy, as will be shown in the next chapter, has to be taken into account in the particles identification process.

2.6 Emulsion Spectrometer for light particles detection

To detect low Z fragments (i.e. $Z \leq 3$, mainly protons, deuterons, tritium, Helium and Lithium ions), an emulsion spectrometer (ES) has been included in the FOOT setup. In *Fig.2.17* the arrangement of the ES inside the FOOT apparatus is shown: it is placed behind the Start Counter and the Beam Monitor, since it extends the angular acceptance up to about 70° with respect to the beam axis. Precisely, the whole system integrates the target and the ES detector in a compact setup, providing a very accurate reconstruction of the interactions occurring inside the target with a high spatial resolution of the order of sub-micrometer and an angular resolution of 0.4-2 $mrad$.

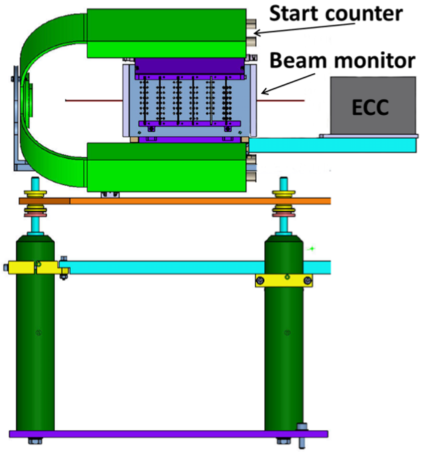

Figure 2.17: Scheme of the FOOT apparatus for light particles detection[46].

In detail, the ES for the FOOT experiment is designed with passive materials (as Carbon or C_2H_4) acting as a target, alternated to nuclear emulsions films behaving as both high-resolution tracking devices and ionization detectors. In fact, it can be divided in three sections: vertex and tracking detector, ionization detector for charge identification and tracking detector for momentum measurements, as shown in *Fig.2.18*.

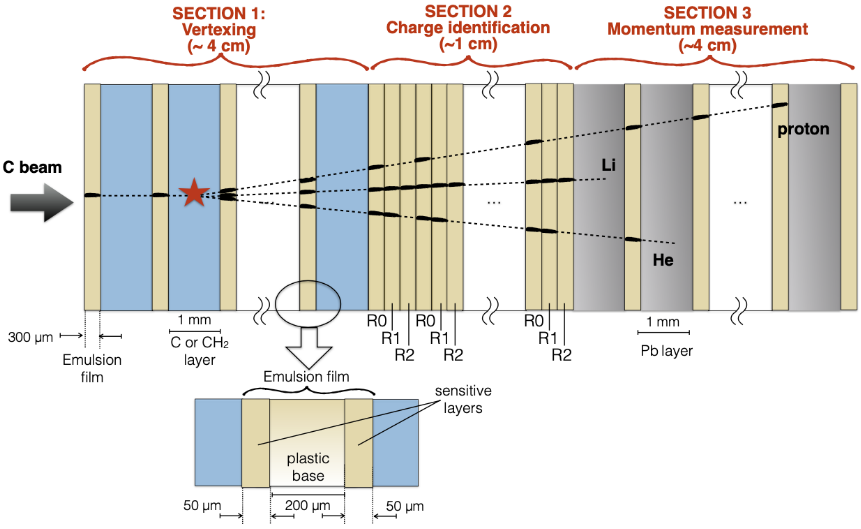

Figure 2.18: Scheme of the emulsion spectrometer composition for the FOOT experiment[46].

The nuclear emulsion films consist of two 50 μm thick sensitive layers deposited on both sides of a 200 μm plastic base, resulting in a total thickness of 300 μm. The sensitive regions are made of $AgBr$ crystals of 0.2 μm diameter scattered in a gelatine binder, able to detect Minimum Ionizing Particles (MIPs). The MIP trajectory is recorded by all AgBr crystals along the particles path, which act as latent image centers. A chemical process, known as development, enhances the latent images inducing the growth of silver clusters (grains) with a diameter of 0.6 μm, which can be seen with an optical microscope. The grains density is proportional to the ionizations caused by the passage of the charged particle, thus the energy loss can be retrieved from it.

Summing up, in the first section emulsion films, interleaved with carbon or C_2H_4 layers, reconstruct the particles vertex position. The thickness of the layers is defined by the interaction length, in order to obtain a sufficiently high number of interactions fully contained in the detector. The charge measurement region (the second one) is composed by emulsion films, aiming to the atomic number identification for low charged fragments. In this case, the elementary cell is made of three emulsion films. The last region, dedicated to the momentum measurement, consists of several alternated emulsion films (300 μm thick) and absorber layers (1 mm of Pb). By measuring the entire particle track length, the kinetic energy is evaluated taking into account the correlation between range and momentum. The latter can be also estimated through the Multiple Coulomb Scattering (MCS) process measuring the $x - y$ spatial coordinates and the deviation of the track slope along the particles path.

Chapter 3

Isotopic identification of fragments

The FOOT experiment has been designed to firstly identify the fragments produced in inelastic interactions. To this purpose, it is necessary to specify that a nuclear fragment is uniquely identified when its atomic number Z and mass number A are correctly determined. The latters make it possible, subsequently, to achieve the measurements of the nuclear cross sections of fragmentation (Eq. 2.6).

In particular, the produced hydrogen, carbon and helium isotopes for istance, which for a given kinetic energy per nucleon have different ranges, cause different biological damages, as shown in the first chapter, thus in order to properly identify the particles and to account for the different impacts on the RBE, it is essential to reach a high accuracy on the TOF, momentum, β, kinetic energy measurements and energy loss. In fact, these quantities are fundamental to identify the fragments, as will be better explained in the following sections. Therefore, my thesis work focuses mainly on this specific question exploiting the FOOT experimental electronic apparatus (see chapter 2).

3.1 FLUKA Monte Carlo simulation code

Software components concerning simulation and data reconstruction play a key role in FOOT. At present, the full reconstruction chain for both data and simulated events is performed by a ROOT based framework, developed at the beginning in the GSI laboratory within the FIRST collaboration[1].
Regarding simulation, it is carried out by the FLUKA Monte Carlo code. In detail, FLUKA is a tool developed from the collaboration of INFN and CERN, which provides simulations of particles interactions with matter (for istance graphite and polyethylene targets) and transport of hadrons, heavy ions and electromagnetic particles in the energy range between keV and TeV, therefore it can be used both in space radioprotection studies and medical physics (i.e. in charged particle therapy)[46].

---

[1] The FIRST (*Fragmentation of Ions Relevant for Space and Therapy*) project was an experiment performed at the SIS accelerator of GSI laboratory in Darmstadt which has been designed for the measurement of ion fragmentation cross sections at different angles and energies (between 100 and 1000 $MeV/nucleon$) on a thin (8 mm) graphite target[52].

In addition, during the planning stage the complete simulation of the entire FOOT experimental setup is a powerful tool to optimise the design, the detectors performances and to identify possible critical points in the layout in order to improve the experimental accuracy.

Thus, the MC simulations produced using the FLUKA code have been exploited to design the whole FOOT electronic setup aiming to enhance the fragments reconstruction and identification performances. *Figure 3.1* shows the complete geometry of the apparatus described in the previous chapter, implemented in FLUKA.

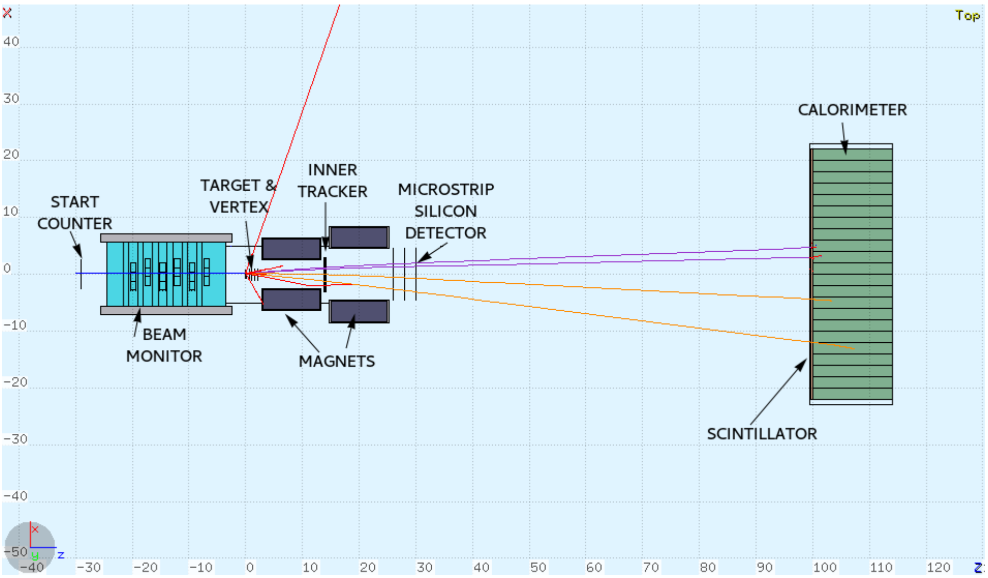

Figure 3.1: 2D view of the FOOT geometry in FLUKA, showing an example of a simulated interaction of a primary ^{16}O ion with a polyethylene target. The MC code manages the transport of all primary and secondary particles throughout the experimental volume and scores the quantities of interest[46].

The simulation of each detector response is stored in a ROOT file, then the data analysis is performed. However, in order to obtain results, FLUKA requires some physical specifications about the setup, the target and the beam, which have to be included in input and geometry files of the code[46]. To run the simulation, the user must provide:

- GEOMETRY: dimensions and distances between the geometry regions, i.e. targets and detectors, magnetic fields description;
- MATERIAL: definition of the materials and their assignment to the different regions;
- BEAM: source position, beam particle type, energy, spatial and/or momentum spread;
- PHYSICAL OPTIONS: production and transport energy cutoffs, δ-rays production thresholds and activation of heavy fragments evaporation to achieve accurate results for residual nuclei production.

In particular, concerning the beam and the secondary fragments, FLUKA calculates the stopping power on the basis of the Bethe-Block formalism (Eq. 1.1) and charged particles are transported through a MCS (*Multiple Coulomb Scattering*) algorithm, based on the Moliere theory[54]. In *Figure 3.2* the electromagnetic interactions are briefly summarized.

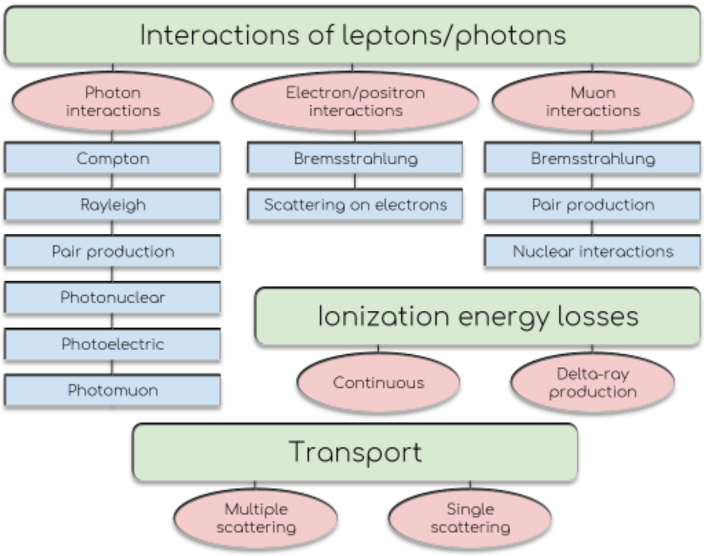

Figure 3.2: Scheme of all the electromagnetic interactions and the transport processes considered in FLUKA[53].

Furthermore the related transport algorithm, allows to accurately handle even some challenging problems, such as electron back scattering and energy deposition in thin layers, even at energies of the order of few keV.

However since the goal of the FOOT experiment is to study the nuclear interactions of therapeutic ion beams, it is very important to show the FLUKA models, already implemented:

- *The hadron-nucleus model*: hadron-nucleus inelastic collisions in FLUKA are described in terms of resonance and decay production, up to a few tens of GeV and, in terms of the *Dual Parton Model*[2] (DPM) coupled to a hadronization scheme, up to tens of TeV. Thus, these kinds of interaction can be represented by three steps: the *Glauber-Gribov cascade*[55] (for energies >5 GeV) or *Generalized Intra-Nuclear cascade GINC*[3] (for energies <5 GeV) which corresponds to the abrasion phase, a pre equilibrium emission in which the nucleus reaches a balance through a chain of nucleon-nucleon collisions and at the end an evaporation, fission, fragmentation or γ de-excitation event as long as the energy is insufficient for any other process.

---

[2] The *Dual Parton Model* is a phenomenological model of multiparticle production in hadronic and nuclear collisions, based on a quark/parton description.

[3] The *Glauber-Gribov* and the *GINC* models are some of the most common tools used in the variant representation of the *Abrasion-Ablation mechanism*, already explained in Section 1.2.5.

- *The nucleus-nucleus model*: for the description of nucleus-nucleus interactions, that are extremely important in the PT field, the last two stages reported for the hadron-nucleon interaction, are essentially the same, whereas for the initial cascade stage the nucleus-nucleus reactions are simulated with two main methods, depending on the energy range: the *relativistic Quantum Molecular Dynamics (rQMD)* approach[56], applied in FLUKA for projectile energies in the range between 100 MeV/n and 5 GeV/n, and at lower energies, the *Boltzmann Master Equation(BME)* theory[57]. The first one predicts the dynamical evolution of particles, the formation of heavy and light fragments and secondary nucleons, while the BME model describes the de-excitation evolution of the system composed by two interacting nuclei during the pre-equilibrium phase.

  The inelastic interaction probability for nucleus-nucleus interaction is given by the total reaction cross section $\sigma_R \propto E_{proj}$. FLUKA uses this value in addition to the particle decay time in order to determine the mean free path of a transported particle. For energy below a few GeV down to the Coulomb barrier, FLUKA uses a parametrization of the total reaction cross section based on the Tripathi semi-empirical formula[58] while for higher energies the Glauber model predictions is used. As an example, *Figure 3.3* shows the predicted nuclear reaction cross section of carbon ions for the most common elements in the human body as a function of the energy.

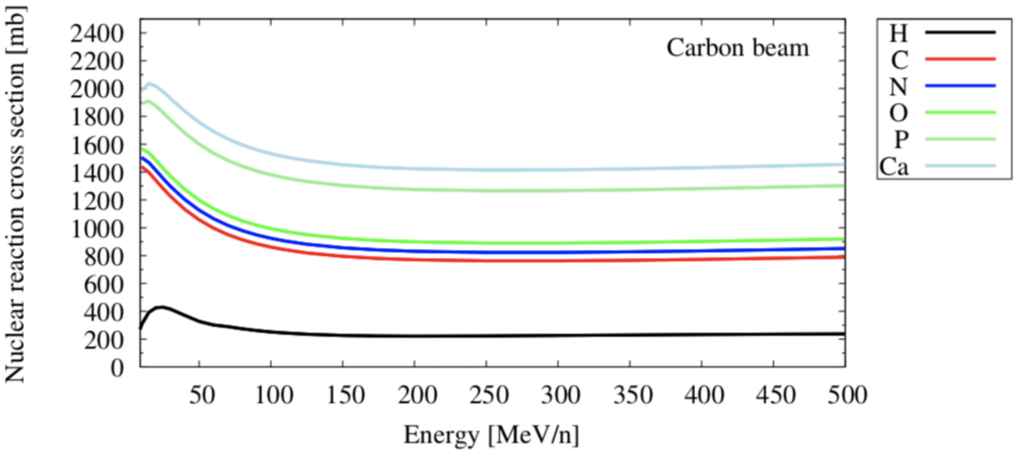

Figure 3.3: Reaction cross section of carbon ions at therapeutic energies as predicted by FLUKA for the most frequent elements present in the human body. A strong dependence on energy at values lower than 20 MeV/n and a constant behavior at energies greater than 100−500 MeV/n can be observed[59].

Concerning this topic, it is very important to underline that the agreement between the experimental data and the FLUKA nuclear fragmentation models is reasonable but not enough for all the cases of medical applications. As reported in Section 1.3.4, to achieve the required PT accuracy, the double differential cross sections measurements, missing at present, are crucial. Nevertheless FLUKA nuclear models are appropriate to optimize the FOOT experimental apparatus and the related performances and, thus at present allow us to obtain an accurate calculation of the dose released in the patient body.

3.2 Resolution of detectors

In order to test the proper identification of particles charge and mass, in this thesis work analysis has been carried out on FLUKA simulated data, setting the complete geometry of the electronic apparatus in the simulation. Specifically, an incident ^{16}O ions beam has been used on a C_2H_4 target of 2 mm thickness, with a kinetic energy of 200 MeV/n. To simulate the same influence on measurements of the finite resolution of the actual FOOT detectors, a *Gaussian smearing*[4] has been applied on FLUKA generated quantities of interest, which are the momentum p, the Time of Flight TOF, the deposited energy ΔE_{SCN} in the TW scintillator and the kinetic energy $E_{k_{CAL}}$ released in the calorimeter, exploiting the detectors resolution reference values already mentioned in Section 2.2. The applied resolutions reflect the performance of each subdetector measured in various test beam.

In detail, the momentum resolution is about $\sim 3.7\%$ and it is obtained by studying the data of a tracks reconstruction program; its value depends on few factors: the MCS scattering, the magnetic spectrometer detectors resolution and the magnetic field intensity and spatial extension. Whereas the TOF, i.e. the time taken by particles to travel the distance between the VTX and the TW detector as will be shown in the next section, has a resolution which scales with the inverse of the energy released in the SCN, and according to Eq. 1.1 the latter increases with the charge of the particle. Therefore for light particles (for istance protons, Helium), due to their lower energy loss in the scintillator, time resolution has been estimated in a range between 100 and 140 ps, depending on the energy, on the contrary heavier fragments have an almost independently trend, with a resolution mean value of $\sim$ 70 ps, as shown in *Figure 3.4*.

---

[4] The *Gaussian smearing* is a method used to make the ideal measurements obtained in FLUKA more real. It is applied in order to worsen the generated quantities values and achieve experimental-like data sample because the actual detectors response has to be simulated.

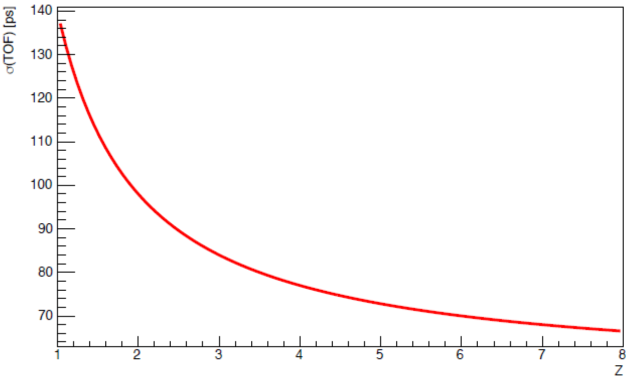

Figure 3.4: Time of flight resolution applied to simulated data, depending on the atomic number of fragments. This parametrization will be used to set the TOF resolution in my MC analysis code in the next section[46].

The resolution of the energy loss in the TW subdetector, gets better as the energy released in the detector material increases, thus for heavier ions case particularly. From the parametrized resolution curve, shown in *Figure 3.5*, its value is considered at level of 4.5%.

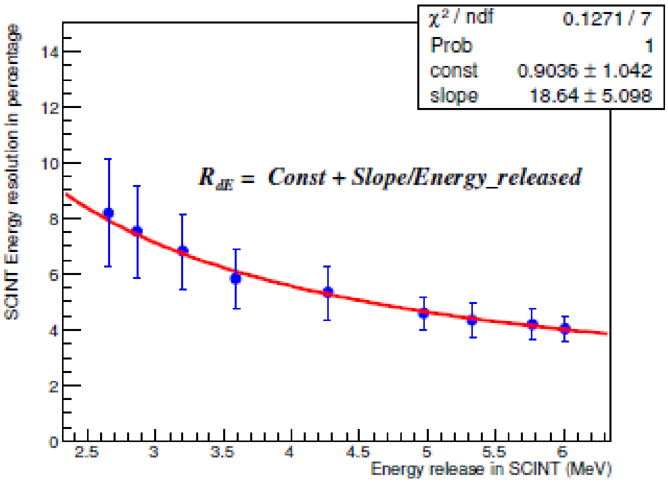

Figure 3.5: Resolution (%) of the energy released in the the plastic scintillators depending on the deposited energy in the material[46].

Lastly, for the energy detected in the calorimeter, the related resolution is fixed at 1.5% because experimental tests have shown that $\sigma(E_{k_{CAL}})$ is linearly proportional to the particle energy with good approximation, meaning that the resolution is dominated by the constant term.

All the aforementioned resolutions, which will be described in detail in the next section, have been estimated through several test beam and they are summarized in the following table (*Table 3.1*).

Quantity	Resolution (%)
p	3.7%
TOF	1-2%
ΔE_{SCN}	4.5%
$E_{k_{CAL}}$	1.5%

Table 3.1: Resolutions (%) of p, TOF, ΔE_{SCN} and $E_{k_{CAL}}$, which have been applied as a gaussian smearing to these quantities measurements in my thesis analysis code.

In addition to the previous resolution values, it is very important to take into account the neutrons issue, already outlined in the FOOT calorimeter description (Section 2.5.3): the performance of the apparatus on the Z and A measurements/reconstructions also strongly depends on the production of these secondary neutral fragments whose only a small fraction of their kinetic energy is recovered, therefore there is a not negligible leakage inside the CALO, mostly due to neutron emission in the spallation process with the calorimeter material. As will be shown in Section 3.4, mainly for this reason it is necessary to have a redundant detector capable to give more than one measurement of A, in order to identify particles reducing the related uncertainty.

In *Figure 3.6* simulation results are reported and they show the percentage of events with energy deposited, highlighting for each kind of fragment (i.e. the most frequent isotope from $Z = 1$ to $Z = 8$), the distribution of the ratio between the "reconstructed" deposited energy in the TW and in the CALO with respect to the "generated" (MC) kinetic energy: $\frac{E_{k,CALO} + \Delta E_{SCN}}{E_{k,gen}}$. In particular, the underestimation of particles energy is evident in the left tails of the graphs below, mostly due to neutrons emission.

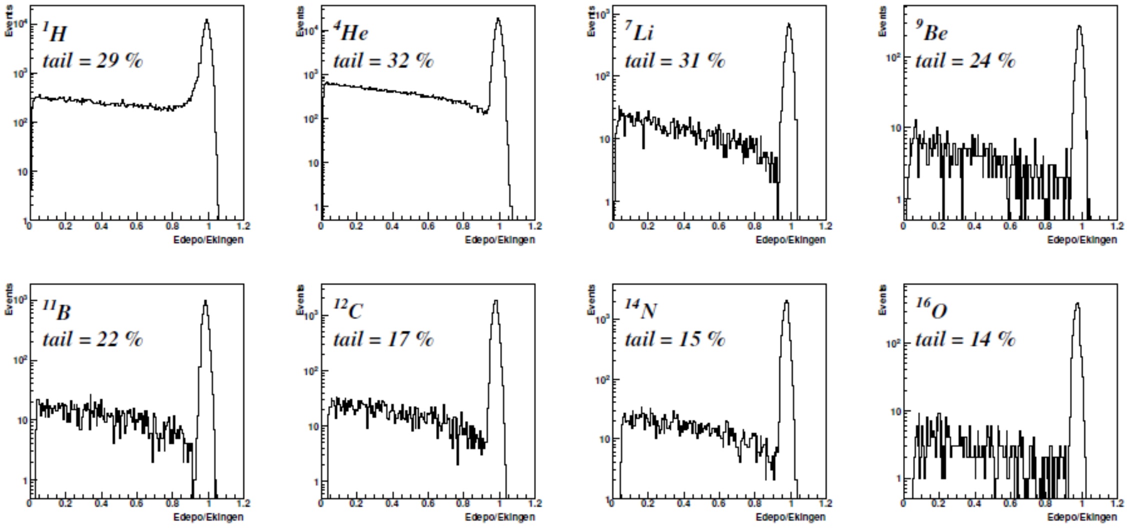

Figure 3.6: Distributions of the ratio $\frac{E_{k,CALO} + \Delta E_{SCN}}{E_{k,gen}}$. The Gaussian trend of the peaks ($\sim$ 1) is due to the applied detectors resolutions (see *Table 3.1*). The events with a kinetic energy deposition less than 90% of the generated one are considered to belong to the tail, thus this means that a fraction of the particles energy is not released, some fragments escape from calorimeter[46].

3.3 Charge Identification

The fragments charge is evaluated using both the energy loss and the time of flight measurements. These two quantities are related to the particle charge according to the Bethe-Bloch equation (1.1). As already said in the previous chapter, ΔE_{SCN} can be evaluated using the TW (Section 2.5.3), while TOF data by the start counter (Section 2.5.1) and TW.

Part of my thesis work has consisted in the development and in the implementation of an algorithm for the measurement of the fragment atomic number Z.

In particular, the particles of interest, which have been considered, are: ^{1}H, ^{4}He, ^{7}Li, ^{9}Be, ^{11}B, ^{12}C, ^{14}N, ^{16}O.

3.3.1 Time Of Flight and β measurements

In FLUKA simulations, in each event the start time is given by the STC detector when the primary beam is injected in the simulated geometry, whereas the stop signal is provided by the plastic scintillators (TW) in the downstream region. Therefore, the TOF value is calculated by subtracting t_{STC}, to the stop time, t_{TW}. However, it is necessary to include also the time it takes the primary to travel from the STC to the VTX, $t_{primary}$ (or *offset*, as in *Fig.3.7*), that has to be subtracted as well, because it has to also reconstruct the fragments time of flight. Therefore, the TOF has been obtained as follows:

$$TOF = t_{TW} - t_{STC} - t_{primary} = t_{TW} - t_{VTX}. \tag{3.1}$$

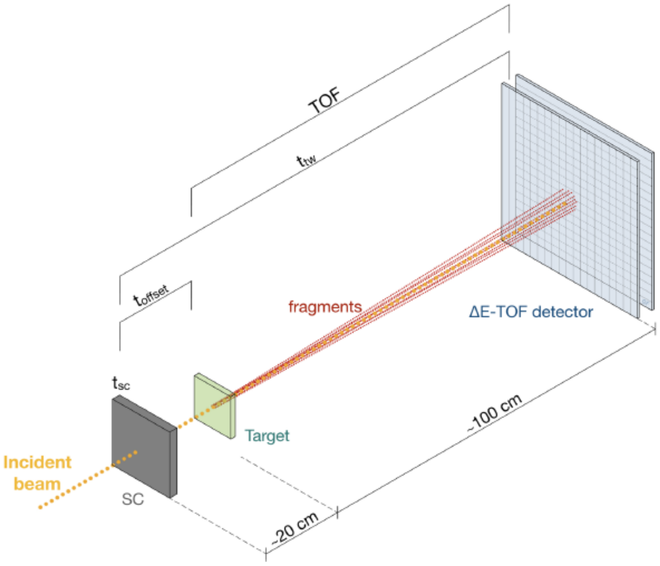

Figure 3.7: A simplified schematic view of the fragments TOF measurement.

The FOOT electronic setup main goal is to measure heavier fragments (see Section 2.5), for which, according to experimental findings, the time resolution would not strongly depend on the energy loss. Therefore, to reproduce this experimental trend, in this work the time measurement resolution, has been empirically parametrised as a function of the particle charge (as in *Fig.3.4*):

$$\sigma_{TOF} = a_1 + \frac{a_2}{Z} \tag{3.2}$$

where $a_1 = 56\ ps$, $a_2 = 84\ ps$ are parameters determined to fit experimental results, and Z the particles atomic number. Consequently, for istance, concerning C ions the time of flight resolution is $\sigma_{TOF} \simeq 70\ ps$, while for H ions $\sigma_{TOF} \simeq 140\ ps$, more precisely.

Afterwards, it has been applied a Gaussian smearing to the values obtained from relation (3.1), using the TOF resolutions, in order to correctly simulate the real detectors behaviour. In *Figure 3.8*, all the results are shown for all the most frequent isotopes.

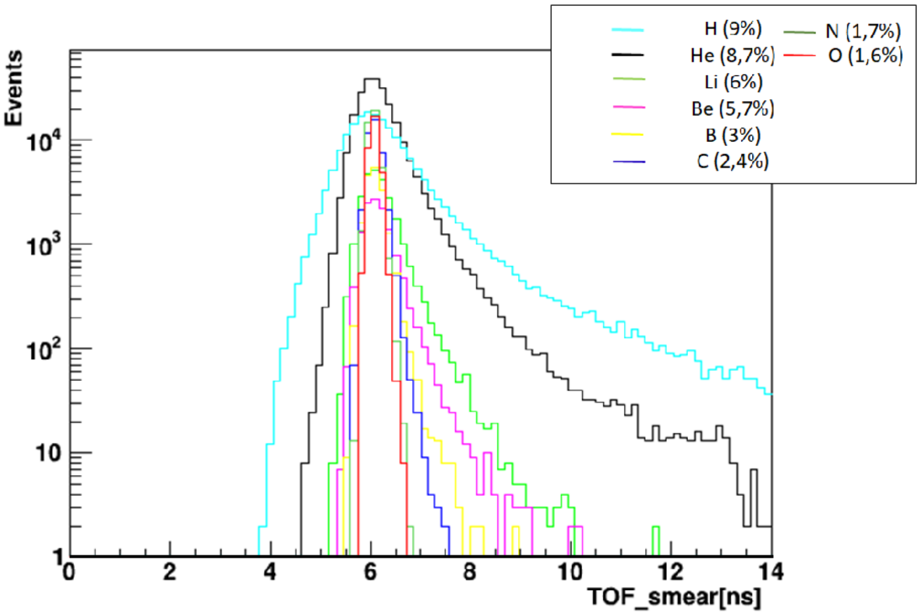

(a)

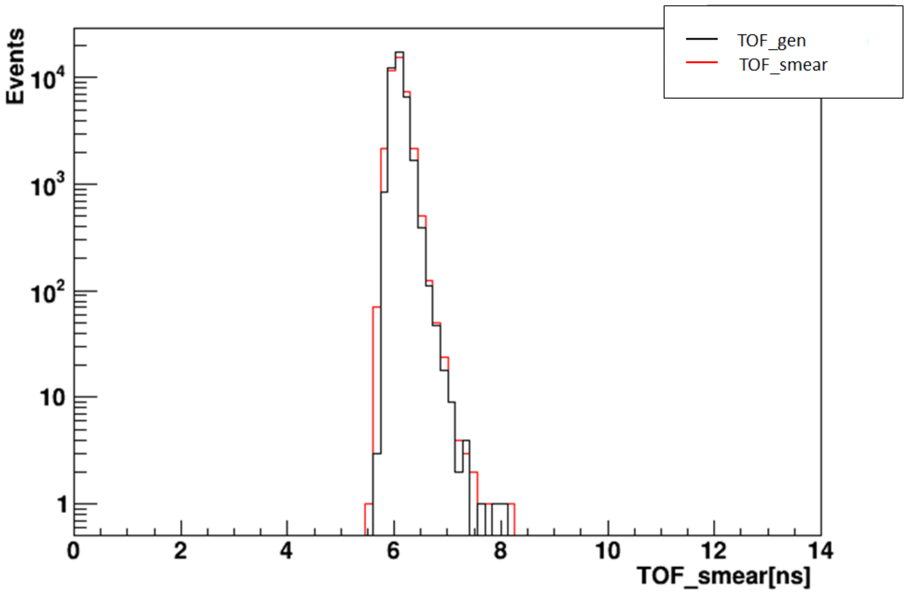

(b)

Figure 3.8: (a) Time of flight distributions in log scale for different ions produced by a ^{16}O beam at 200 MeV/n on a polyethylene target. It is evident that for light particles the TOF resolution have greater values, thus a wider peak can be observed with respect to the heavier particles case. (b) TOF distributions in log scale of ^{12}C with the Gaussian smearing (red line) and without it (black line).

Now, it is fundamental to evaluate the β value, which represents the particle velocity in c units, as:

$$\beta = \frac{1}{c}\frac{L_{TOF}}{TOF} \tag{3.3}$$

with L_{TOF} the total distance traveled by the particle from the VTX to the entrance face of the scintillator. Nevertheless, one can note that the particle trajectories are not straight lines, beacause of both MCS and the magnetic field effect, thus in this study, L_{TOF} has been obtained by approximating the actual trajectory to the sum of several consecutive segments, exploiting all the points coordinates (x, y, z) extracted by the simulated tracker system.

Concerning the corresponding resolution, it is expected to be:

$$\sigma_\beta = \frac{\partial\beta}{\partial TOF}\sigma_{TOF} = -\frac{1}{c}\frac{L_{TOF}}{TOF^2}\sigma_{TOF} \tag{3.4}$$

where one can consider distance resolution to be negligible with respect to the other quantities.

3.3.2 Energy loss in the TW

The energy loss ΔE, which will be used for the Bethe-Bloch formula, has been reconstructed as the sum of the energy deposited by the same particle in the TW scintillator (*Fig.3.9*), before fragments reaches the calorimeter region, thus $\Delta E = \Delta E_{SCN}$. Furthermore, its resolution, applied as Guassian smearing, has been empirically parametrized as a function of the deposited energy according to the results obtained in experimental tests, as already mentioned in Section 3.2, through the following relation:

$$\sigma_{\Delta E_{SCN}} = b_1 + \frac{b_2}{\Delta E_{SCN}} \tag{3.5}$$

where $b_1 = 4.65\ MeV$, $b_2 = 4.0\ MeV^2$ are experimental fit parameters and ΔE_{SCN} (MeV)[5] represents the energy loss in the plastic scintillator.

---

[5] FLUKA code provides the energy data in GeV, the time values in ns and the distance in cm.

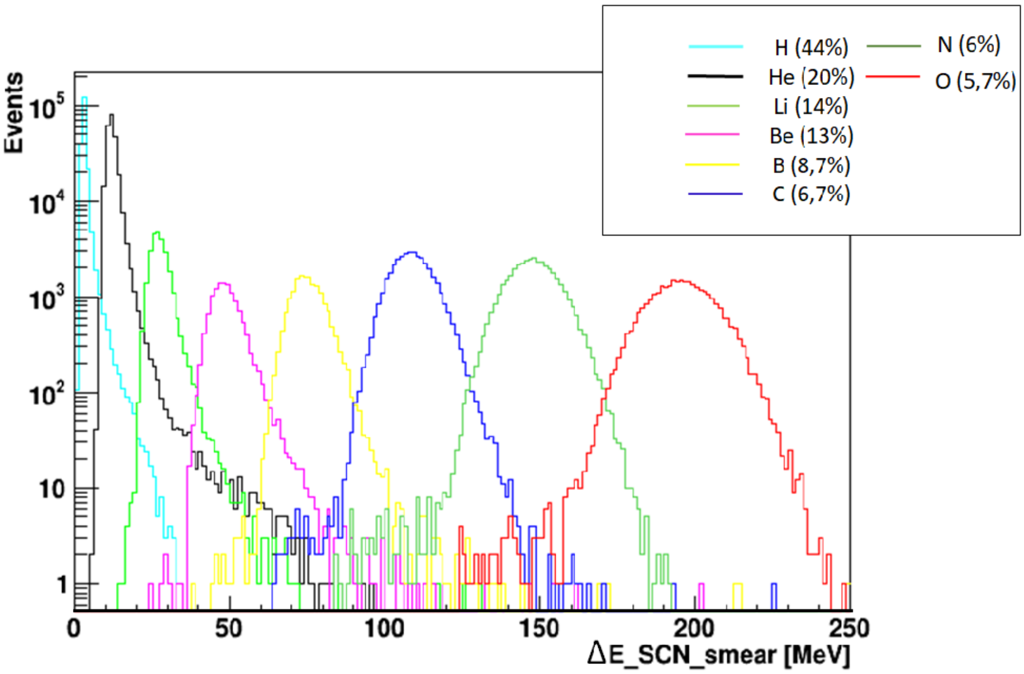

(a)

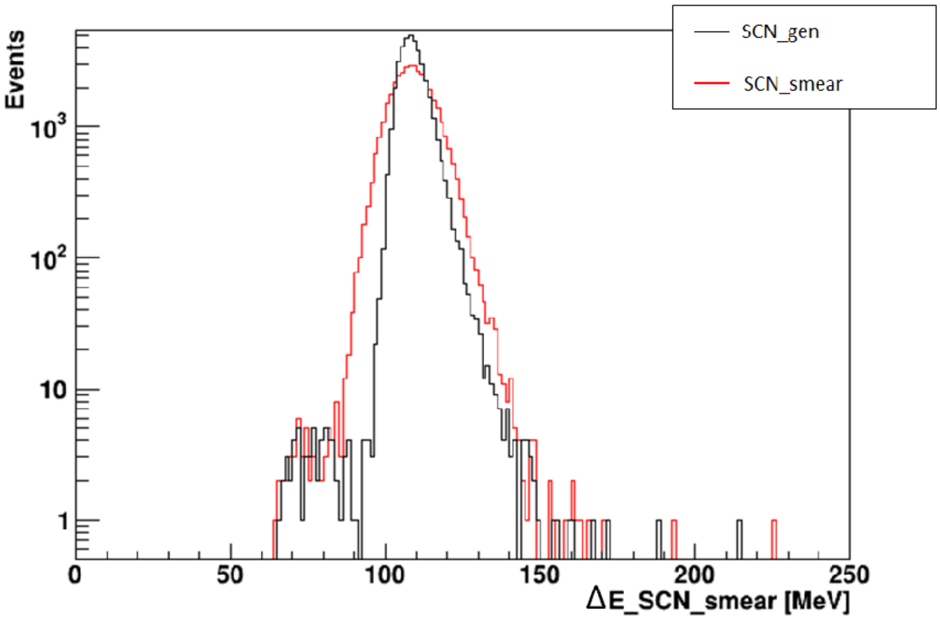

(b)

Figure 3.9: (a) ΔE_{SCN} (MeV) distributions in log scale for different ions produced by a ^{16}O beam at 200 MeV/n impinging on a polyethylene target. (b) ΔE_{SCN} (MeV) distributions in log scale of ^{12}C with the Gaussian smearing (red line) and without it (black line).

3.3.3 Results

The charge identification is performed using both the ΔE_{SCN} and the time of flight measurements; these latters are related to the fragments atomic number Z through the Bethe-Bloch expression (1.1), therefore, by inverting it, the following formula can be achieved:

$$Z_p = \sqrt{\frac{\Delta E_{SCN} A_{SCN} \beta_p^2}{K Z_{SCN} \Delta x_{SCN} \rho_{SCN} n_{layer} log(\beta)}} \tag{3.6}$$

where the energy loss per unit path length, dE/dx, can be obtained as the ratio between ΔE_{SCN} and the total thickness $\Delta x_{SCN} = 0.3\ cm$ of the two TW scintillator layers (n_{layer}). The Z_{SCN}, A_{SCN} and $\rho_{SCN} = 1.023\ g/cm^3$ are the scintillator atomic number, mass number and density, respectively and in particular, the ratio Z/A value is equals to 0.54157. Lastly, the "$log(\beta)$"[6] and K represent the log term and the constant of the Bethe-Bloch (see eq.(1.1) for the symbol meaning) respectively.

The reconstructed Z values for the studied fragments are displayed below in Table 3.2. As one can note, the related resolution improves with increasing particles charge, passing from 5.5% for the hydrogen to 2.7% for the oxigen.

Fragment	Z	$\sigma(Z)[\%]$
H	1.01 ± 0.06	5.5
He	2.02 ± 0.07	3.6
Li	3.04 ± 0.09	3.1
Be	4.07 ± 0.12	3.0
B	5.09 ± 0.14	2.9
C	6.13 ± 0.17	2.8
N	7.14 ± 0.20	2.8
O	8.19 ± 0.22	2.7

Table 3.2: Reconstructed Z for fragments generated by a ^{16}O beam impinging on a C_2H_4 target at 200 MeV/n, where $\sigma(Z)$ is the gaussian fit error associated to the mean value.

In *Figure 3.10* the charge distributions of the most frequent isotopes are reported, where each peak is well separeted from the others and easily distinguishable allowing a more precise identification of Z.

---

[6] $log(\beta) \equiv log\left(\frac{2m_e c^2 \beta_p^2 \gamma_p^2}{I_{SCN}^2}\right) - \beta_p^2$, with $I_{SCN} = 64.684 \times 10^{-9}\ GeV$.

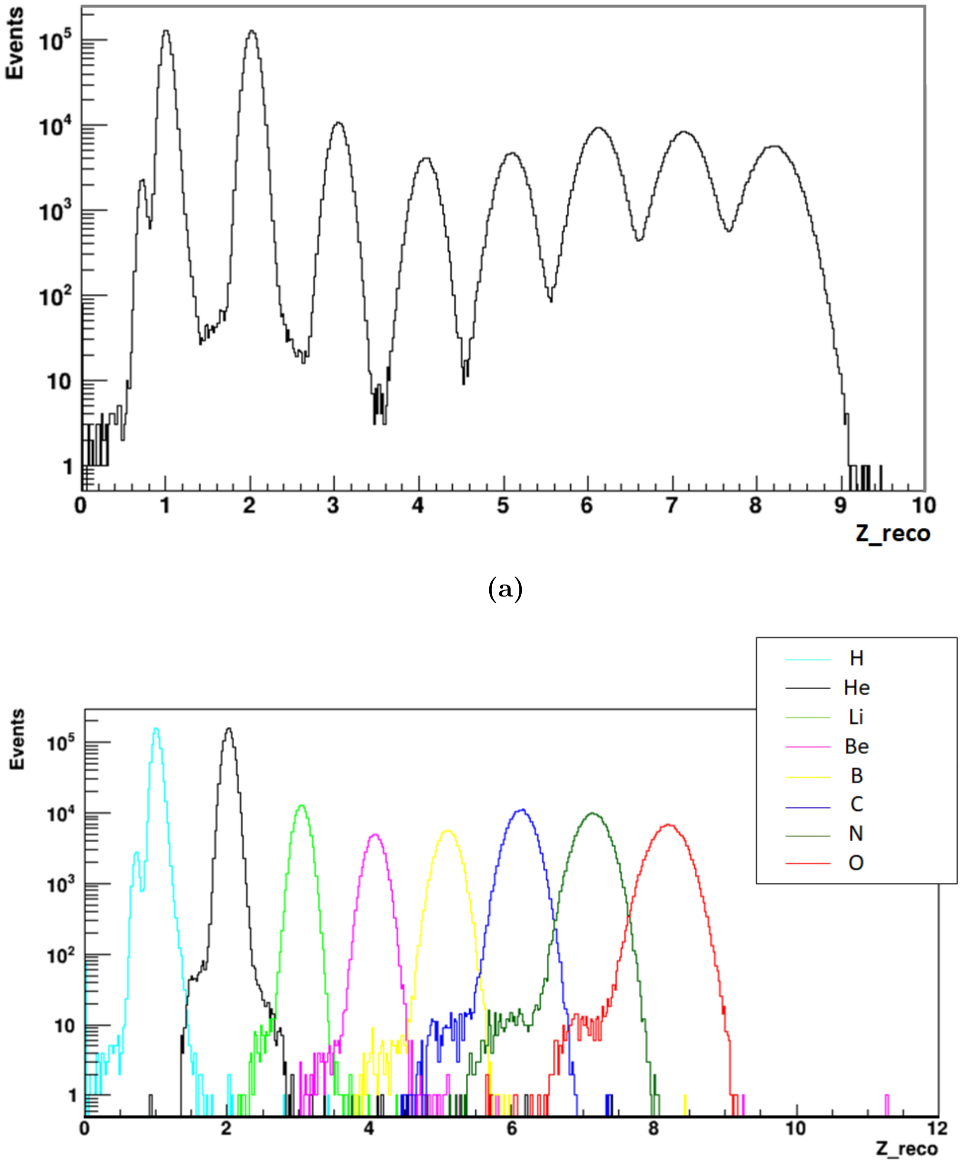

(a)

(b)

Figure 3.10: (a) The total fragments charge distributon (in log scale) with the atomic number Z ranging from 1 to 8. (b) The single fragment charge distribution (in log scale) is shown, where each isotope is depicted with a different color.

In the region of hydrogen an unexspected double peak is present, currently under investigation. The atomic number of each element results overestimated due to a not perfect calibration of the energy loss in TW.

3.4 Mass and Mass number identification

The mass number estimation, merged to the Z values, allows to achieve uniquely the fragments identification. To this purpose, the FOOT setup has been designed to provide redundancy in the isotopic determination, in fact it is possible to obtain three different but correlated evaluations of A by means of combination of the TOF, momentum and $E_{k,CALO}$ measurements.

3.4.1 Particle momentum measurement

The particles momentum has been retrieved from the "generated" momentum, to which a proper resolution has been applied through a Gaussian smearing.
In general, the fragments momentum is derived from the particle deflection inside the magnetic field; due to the Lorentz force a charged particle inside an homogeneous **B** (generated by a L long magnet) has a circular orbit of curvature radius R (see *Fig.3.11(a)*) which depends on the particle momentum p as follows:

$$R = \frac{p}{qB} \tag{3.7}$$

where q is the particle charge. However, $R >> L$, thus the deflection angle θ can be approximated to $\frac{L}{R}$ and, assuming B = (0, By, 0), the particle momentum can be written as:

$$p = \frac{LqB_y}{\theta} \tag{3.8}$$

Consequentially, it is possible to evaluate p, measuring its direction before (θ_{in}) and after (θ_{out}) the magnetic field by means of the tracking system, as shown in *Figure 3.11(b)*.

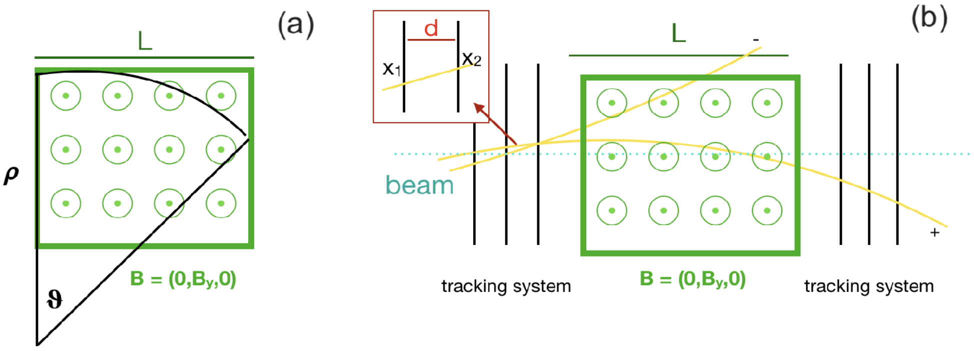

Figure 3.11: (a) Track deflection of a positive/negative charged particle in a magnetic spectrometer, where ρ is the curvature radius. (b) Measurement strategy of the particle incident angle $\theta_{in} \simeq tg\theta = \frac{x_2 - x_1}{d}$.

In *Figure 3.12* the fragments momenta results of this study are shown, which have been determined by applying a gaussian smearing, as mentioned before, to the production momenta obtained from FLUKA simulations. The *Figure 3.12(b)* indicates that the momentum resolution is currently not enough alone to disentangle the momentum of the different isotopes, for this reason, the mass is reconstructed with redundant methods to overcome this problem.

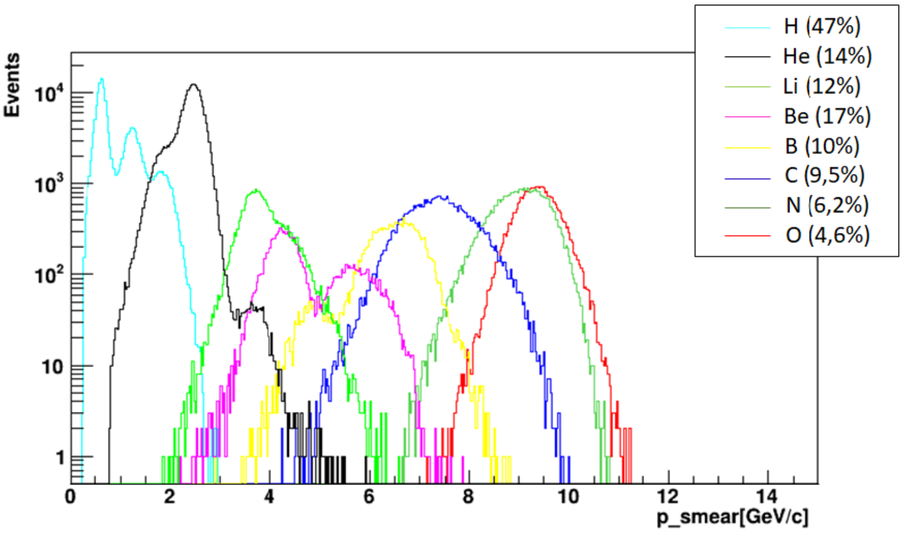

(a)

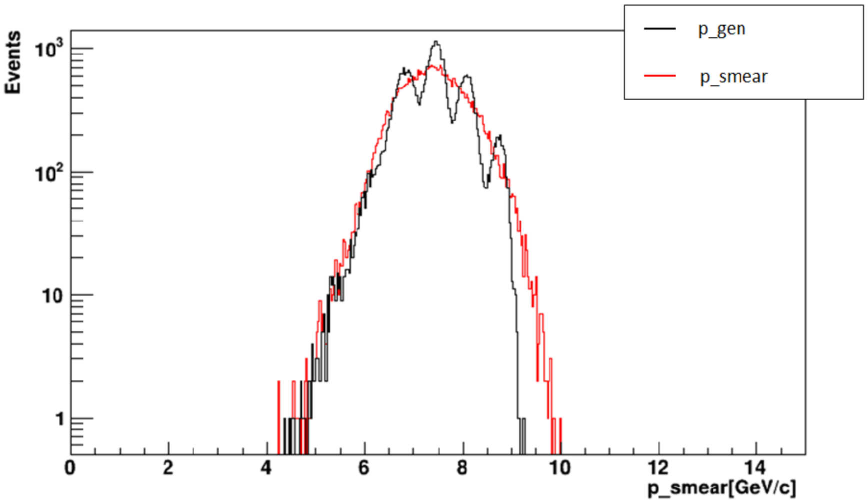

(b)

Figure 3.12: (a) Total momentum distributions (log scale) for different ions produced by a ^{16}O beam at 200 MeV/n impinging on a polyethylene target. (b) Momentum distributions (log scale) of ^{12}C with the Gaussian smearing (red line) and without it (black line).

3.4.2 Particle energy measurement

The total kinetic energy for the determination of A is the sum of the energy deposition in three detectors, i.e. MSD, SCN and CALO.

In particular, concerning the calorimeter region, particles can undergo fragmentation inside the CALO crystals, thus, to take into account background contribution from other fragments the related kinetic energy (*Fig.3.13*), $E_{k,CALO}$ is obtained not only from the released energy associated to the original fragment but from the sum of all the energy releases in the hit crystal (or crystals, if more than one), also deposited by different particles. As in the experimental data-taking, in the simulation crystals are individually ”read” and all contributions are considered (for istance, also charged fragments produced in re-fragmentation processes)[46].

However, in inelastic interactions also neutrons are produced and they may deposit the energy far from the original fragment track or even escape the detector, thus leading to a systematic underestimation of the kinetic energy. In future, more sophisticated crystal clustering algorithm could recover part of this not-collected energy.

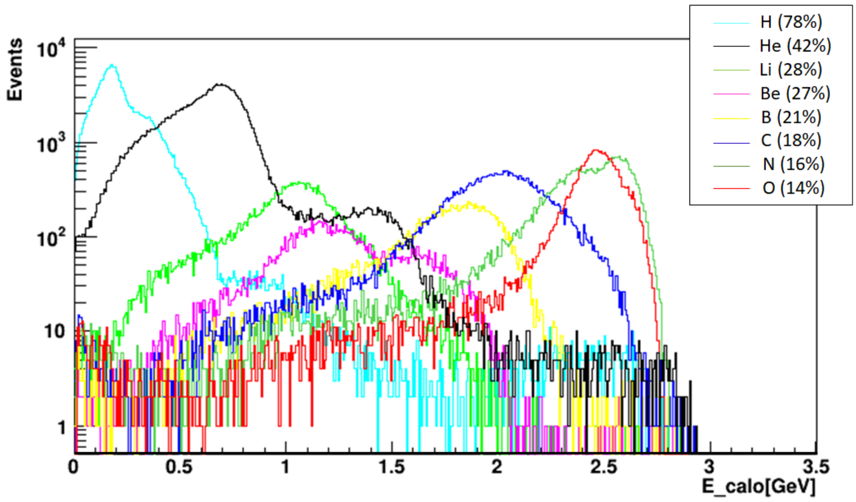

(a)

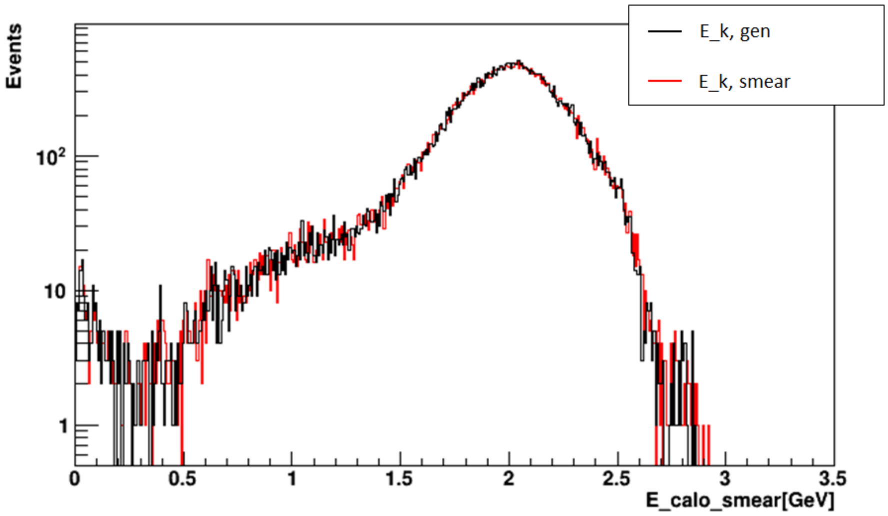

(b)

Figure 3.13: (a) The kinetic energy E_{CALO} distributions (log scale) for different ions produced by a ^{16}O beam at 200 MeV/n impinging on a polyethylene target. (b) E_{CALO} distributions (log scale) of ^{12}C with the Gaussian smearing (red line) and without it (black line).

Therefore, the final resolution on E_k measurements is:

$$\sigma(E_k) = \sqrt{\sigma(\Delta E_{k,SCN})^2 + \sigma(E_{k,CALO})^2} \tag{3.9}$$

where, according to the results obtained in experimental test, the MSD resolution is only given by the stochastic nature of the energy loss process (the electric noise can be neglected).

3.4.3 Measurement of the mass number A of the fragments

Starting from the TOF, p and E_k, it is possible to define three different methods, in order to estimate the fragments mass number; each method depends on only two of these kinematic quantities, thus there is an obvious correlation between these methods because of the presence of a common detector for each couple of A definition.

1. **Combination of p and TOF measurements**

The fragment mass m_0 is related to its momentum and velocity according to the definition of the relativistic momentum:

$$p = m_0 \beta \gamma c = \frac{m_0 \beta c}{\sqrt{1-\beta^2}} \rightarrow m_0 = \frac{p\sqrt{1-\beta^2}}{\beta c} \tag{3.10}$$

where β is obtained through the TOF measurement, according to (3.3) relation. Hence, the mass number can be calculated as follows:

$$A_1 = \frac{m_0}{U} = \frac{1}{U}\frac{p}{\gamma \beta c} \tag{3.11}$$

with $U = 931.494\ MeV/c^2$, the atomic mass unit. Consequently its corresponding uncertainty is:

$$\sigma(A_1) = \sqrt{\left(\frac{\partial A_1}{\partial p}\sigma(p)\right)^2 + \left(\frac{\partial A_1}{\partial \beta}\frac{\partial \beta}{\partial TOF}\sigma(TOF)\right)^2}. \tag{3.12}$$

As it can be concluded looking at (3.12), the A_1 uncertainty depends strongly on the resolution of the momentum and β, hence on the TOF measurements accuracy.

In *Figure 3.14* the distributions of the obtained A_1 values for some selected fragments are depicted.

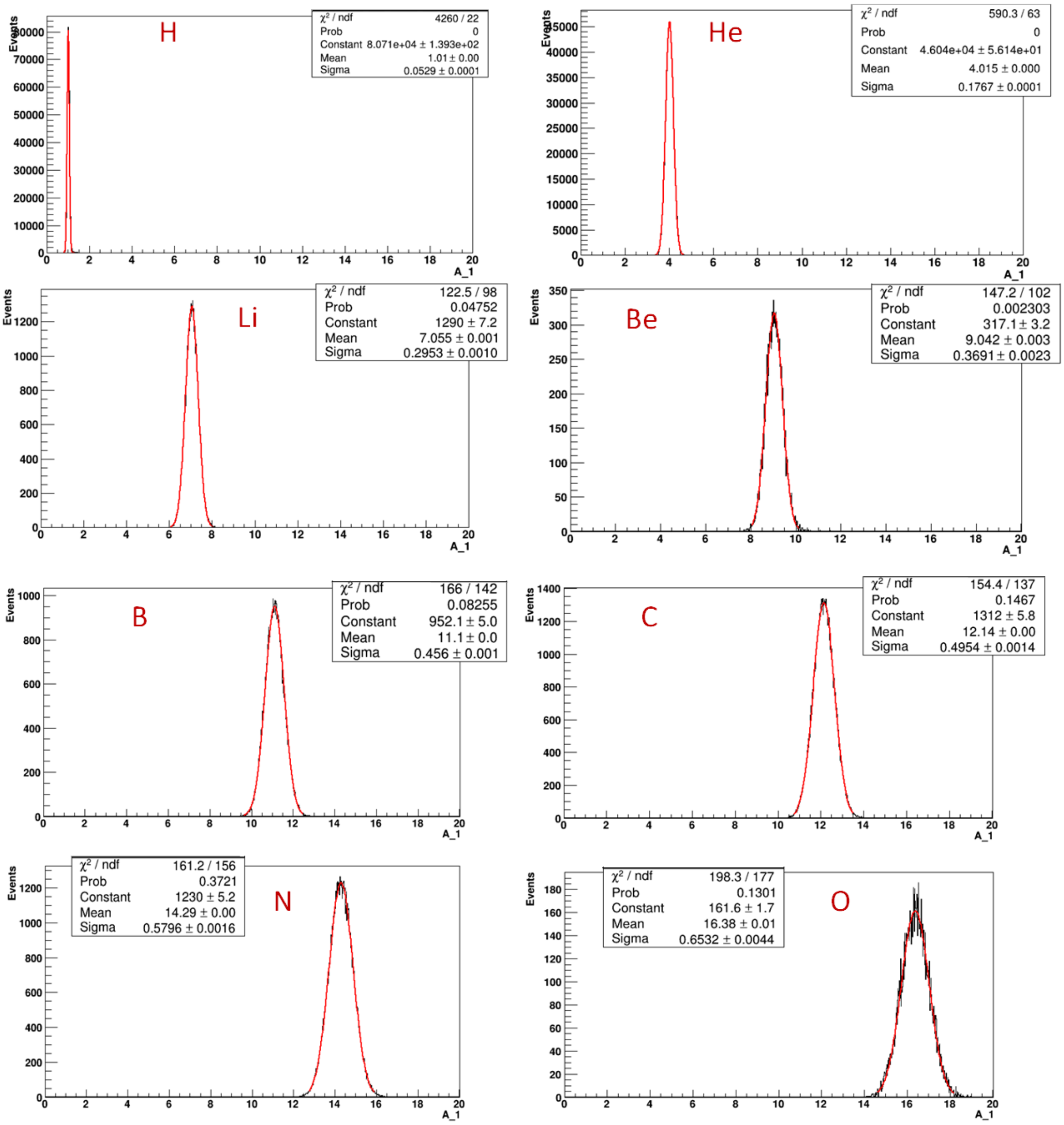

Figure 3.14: Reconstructed A_1 distributions for the most abundant isotopes of fragments by means of the TOF and p measurements (see eq.(3.11)).

2. Combination of TOF and E_k measurements

The second method depends on the simultaneous determination of β and E_k, respectively from the TOF measurement and the calorimeter (considering also the contributions of the energy released in the TW and MSD detectors); in detail, exploiting the definition of the relativistic kinetic energy, i.e. the difference between the total and the rest energy of the fragment, the following relation can be used:

$$E_k = E_{tot} - m_0 c^2 = (\gamma - 1) m_0 c^2 \tag{3.13}$$

Through eq.(3.13), it is possible to express the particles mass, as:

$$m_0 = \frac{E_k}{c^2(\gamma - 1)} \tag{3.14}$$

hence, consequentially, the mass number can be obtained as follows:

$$A_2 = \frac{m_0}{U} = \frac{E_k}{U(\gamma - 1)c^2} \tag{3.15}$$

The related uncertainty is:

$$\sigma(A_2) = \sqrt{\left(\frac{\partial A_2}{\partial E_k}\sigma(E_k)\right)^2 + \left(\frac{\partial A_2}{\partial \beta}\frac{\partial \beta}{\partial TOF}\sigma(TOF)\right)^2} \tag{3.16}$$

In *Figure 3.15* the distributions of the reconstructed A_2 values for some selected fragments are shown. A tail, corresponding to A_2 underestimations, is visible in all the reported plot and it is due, as previously discussed, to an underestimation of the fragment kinetic energy. As before for the first method, the distributions width depends on the resolutions applied to the time of flight and kinetic energy measurements, as expressed in eq.(3.16).

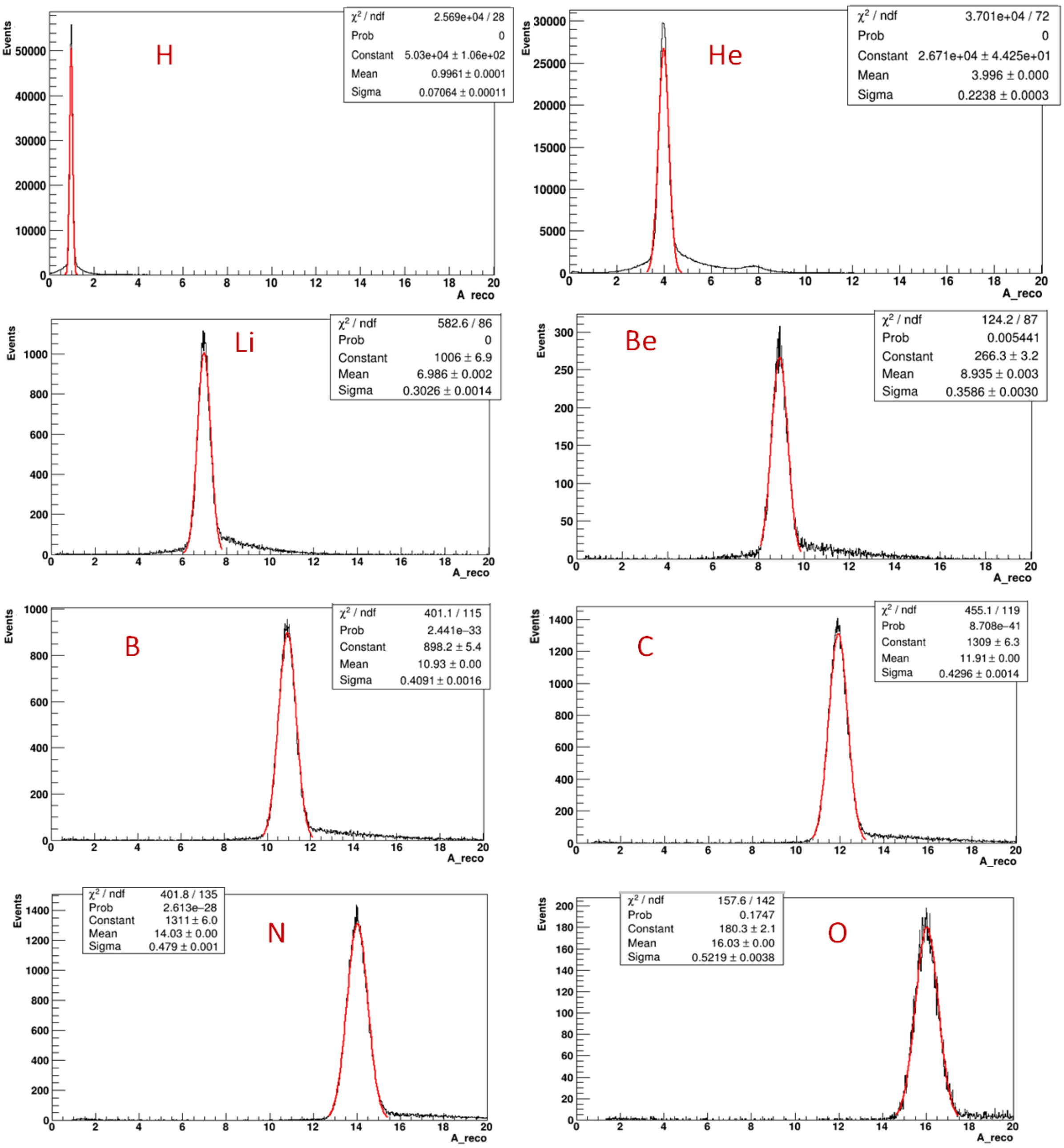

Figure 3.15: Reconstructed A_2 distributions for the most abundant isotopes of fragments by means of the TOF and E_k measurements (see eq.(3.15)).

3. Combination of p and E_k measurements

The particle total energy can be defined by the sum of the kinetic and rest energies or by the energy momentum relation, as:

$$E_{tot} = E_k + m_0c^2 = \sqrt{p^2c^2 + m_0^2c^4} \qquad (3.17)$$

Therefore, by combining the previous relation the mass can be evaluated as follows:

$$m_0 = \frac{p^2c^2 - E_k^2}{2c^2E_k} \tag{3.18}$$

while the mass number:

$$A_3 = \frac{m_0}{U} = \frac{p^2c^2 - E_k^2}{2c^2E_kU} \tag{3.19}$$

The resolution on the mass number determination is expressed as:

$$\sigma(A_3) = \sqrt{\left(\frac{\partial A_3}{\partial E_k}\sigma(E_k)\right)^2 + \left(\frac{\partial A_3}{\partial p}\sigma(p)\right)^2} \tag{3.20}$$

In *Figure 3.16* the A_3 distributions for some fragments of interest are depicted, where the related widths depend on the momentum and kinetic energy measurements resolutions. Also in this case tails due to a not accurate estimate of the kinetic energy are present.

Summing up all the results, the reconstructed A_1, A_2 and A_3 are displayed in Table 3.3, with the gaussian fit errors associated to the corresponding mean values. Moreover in some cases, there is a shift, but it is completely included in the resolution.

However, it is necessary to take into account that the required precision on the mass number measurements, coming from the requirements imposed by particle therapy applications, should be better than 5%. This can be fulfilled if TOF, momentum and energy measurements resolutions are the ones already reported in Section 2.2.

Therefore, for the first method, one can note that the peaks positions are centered around the expected values (see *Fig.3.14*). As far as concern the second and the third reconstruction modes, the distributions present a correleted tail at low and high A values respectively; this is due to the calorimeter, which is the detector that mostly suffers for the energy leakage (especially from neutrons emission). The resolution is slightly worse for the A_2 method than the first one, while it is a bit larger ($\sim$ 10%) in the A_3 case, because, as visible in the formula (3.19), the mass number depends on the square of both the momentum and kinetic energy that increases the applied smearing. In particular, for the last method, the reconstruction is the least precise because of a quadratic dependence on the measurement of the kinetic energy released in the calorimeter in the A_3 relation (see eq.(3.19)). Thus, this involves a factor of 2 in the error propagation.

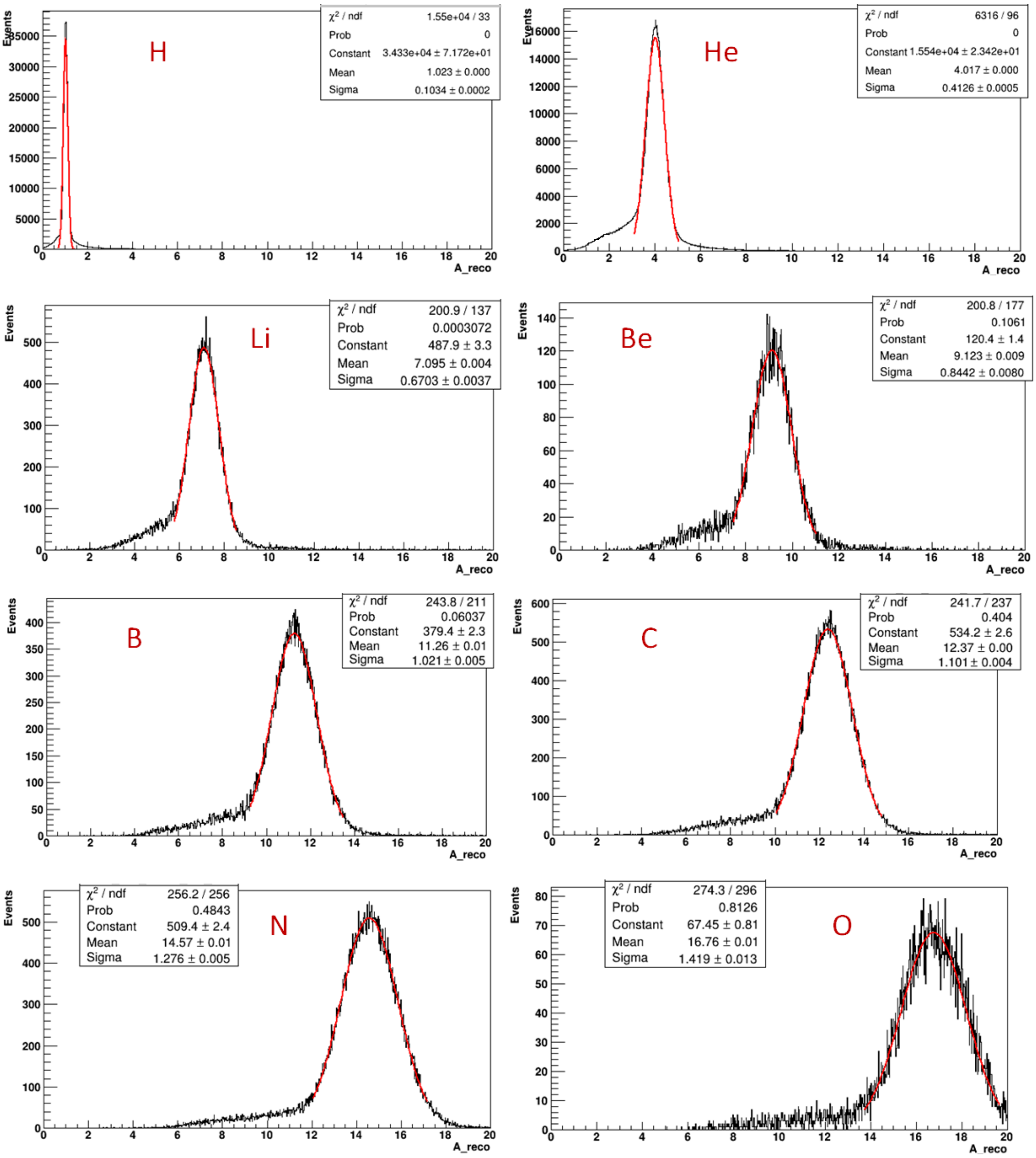

Figure 3.16: Reconstructed A_3 distributions for the most abundant isotopes of fragments by means of the p and E_k measurements (see eq.(3.19)).

	^1H	^4He	^7Li	^9Be
A_1	1.01 ± 0.05	4.01 ± 0.18	7.05 ± 0.29	9.04 ± 0.37
A_2	1.00 ± 0.07	4.0 ± 0.2	6.99 ± 0.30	8.94 ± 0.36
A_3	1.02 ± 0.10	4.02 ± 0.41	7.1 ± 0.7	9.12 ± 0.84
$\sigma(A_1)[\%]$	5%	4%	4%	4%
$\sigma(A_2)[\%]$	7%	6%	4%	4%
$\sigma(A_3)[\%]$	10%	10%	9%	9%

	^{11}B	^{12}C	^{14}N	^{16}O
A_1	11.1 ± 0.5	12.1 ± 0.5	14.29 ± 0.58	16.38 ± 0.65
A_2	10.93 ± 0.41	11.91 ± 0.43	14.03 ± 0.48	16.03 ± 0.52
A_3	11.26 ± 1.02	12.37 ± 1.10	14.57 ± 1.28	16.76 ± 1.42
$\sigma(A_1)[\%]$	4%	4%	4%	4%
$\sigma(A_2)[\%]$	4%	4%	3%	3%
$\sigma(A_3)[\%]$	9%	9%	9%	8%

Table 3.3: Peak values and the related gaussian fit errors on A measurements for each method.

3.5 Fit Methods on A measurements

In order to combine all the three measurements (TOF, p, E_k) and, thus to achieve a better identification of A, the strategy used in this study considers two different fit procedures:

- the Augmented Lagrangian Method (ALM);
- the standard χ^2 minimization.

3.5.1 The Augmented Lagrangian Method

The *Augmented Lagrangian Method (ALM)*[60] is one of the algorithms in a class of methods for constrained optimization which seeks a solution by replacing the original constrained problem by a sequence of unconstrained subproblems; in detail the original objective[7] function $f(\vec{x})$ in the parameter space is modified by the addition of a *penalty term*, preserving the expression derived from the "*Quadratic Penalty Method*[8]" (QPM):

$$\vec{P}(\vec{x};\mu) \equiv f(\vec{x}) + \frac{1}{2\mu}\sum_a c_a^2(\vec{x}) \tag{3.21}$$

where $f(\vec{x})$ is the objective function (see below), c_a are the constraints and μ is the penalty parameter. In particular $\vec{P}(\vec{x};\mu)$ is a function of the constraints weighted by μ and it disappears when the c_a are null, whereas it becomes large if $c_a \neq 0$ in the $\mu \longrightarrow 0$ limit, thus the lower is μ the greater is the effect of the constraints. In fact in the QPM case, unfortunately, when $\mu \longrightarrow 0$ numerical instabilities may prevent convergence to the solution of the minimization process. Therefore, it is necessary to further modify the QPM, exploiting the ALM approach in order to preserve its success but to also overcome the difficulties encountered for $\mu \longrightarrow 0$.

---

[7] An objective function is a mathematical function to be optimized, i.e. the ultimate goal of optimization is to find the value for $\vec{x}$ in a way that this function is maximized or minimized.

[8] More details of the method can be find in [60]

One approach is to introduce the *augmented Lagrange multiplier* terms, leading to the following modified objective function:

$$\vec{L}(\vec{x};\lambda,\mu) \equiv f(\vec{x}) - \sum_a \lambda_a c_a(\vec{x}) + \frac{1}{2\mu}\sum_a c_a^2(\vec{x}) \tag{3.22}$$

with $\vec{\lambda}$ a m-dimension vector of Lagrange multipliers λ_a.

One can note that $\vec{\lambda}$ is no longer determined numerically by the optimization procedure, as in the QPM, but it is instead a fixed vector, just like the penalty parameter. However, as in the case of the QPM, (3.22) is used iteratively; unconstrained minimization of $\vec{L}(\vec{x};\lambda,\mu)$ is performed for the chosen values of λ and μ in each step of the procedure. After optimizing $\vec{L}(\vec{x};\lambda,\mu)$ to within some tolerance, new values of λ and μ are chosen; the process is repeated until the desired levels of optimality is satisfied.

Nevertheless, one must verify that the ALM indeed avoids the problems of the QPM in the μ limit. To this aim, one can note that the gradient of the relation (3.22) recovers the expression for the method of Lagrange multipliers with the substitution:

$$\lambda_a \to \lambda_a - \frac{c_a(\vec{x})}{\mu} \tag{3.23}$$

Thus, in the asymptotic limit:

$$\lambda_a^* \to \lambda_a - \frac{c_a(\vec{x^*})}{\mu} \tag{3.24}$$

but thanks to the ALM, it is possible to freely choose both λ_a and μ, selecting the λ_a value in the $(k+1)^{st}$ iteration (without taking the $\mu \longrightarrow 0$ limit), as follows:

$$\lambda_a^{k+1} = \lambda_a^k - \frac{c_a(\vec{x_k})}{\mu_k}. \tag{3.25}$$

Now, in the application of the ALM to the mass identification procedure in FOOT, μ has been set to 0.1, in order to strengthen the constraint. The first term of eq.(3.22) in this case is represented by:

$$f(T,P,K) = \left(\frac{TOF - T}{\sigma_{TOF}}\right)^2 + \left(\frac{p - P}{\sigma_p}\right)^2 + \left(\frac{E_k - K}{\sigma_{E_k}}\right)^2 \tag{3.26}$$

where (T, P, K) are the set of the fit output paramters, while the TOF, p and E_k are the reconstructed quantities during simulation events and σ the corresponding uncertainties.

The last two terms of (3.22) are expressed as:

$$\begin{aligned}\sum_{a=1}^{m} \lambda_a c_a(\vec{x}) + \frac{1}{2\mu}\sum_{a=1}^{m} c_a^2(\vec{x}) &= \lambda_1(A_1 - A) + \lambda_2(A_2 - A) + \lambda_3(A_3 - A) + \\ &+ \frac{1}{2\mu}\Big((A_1 - A)^2 + (A_2 - A)^2 + (A_3 - A)^2\Big)\end{aligned} \tag{3.27}$$

where the set of (A_1, A_2, A_3) represents the reconstructed mass numbers, retrieved by the previous three methods, while A is the fit output parameter.

As far as concern the analysis of the simulated data, the ALM approach has been implemented by means of the ROOT MINUIT class (in particular Minuit2, written in C++) which is a popular function minimization library, often used for data analysis, as the minimization of χ^2 functions and likelihoods. Generally, this ROOT class contains various minimization algorithms; in this case MIGRAD and SIMPLEX have been chosen to solve the problem (see *Fig.3.17*).

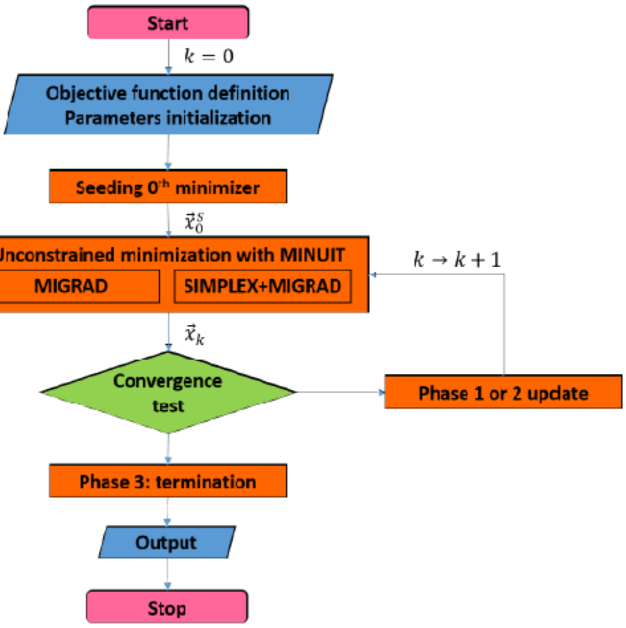

Figure 3.17: Flowchart of the minimization procedure.

At first the penalty parameter is fixed as $\mu = 0.1$ and Lagrange multiplier parameter vector, which are updated in each iteration, have starting values: $\lambda_a^0 = 0$ $(a = 1, ...m)$. Once the initial parameters have been selected, one can perform the minimization with Minuit. In the process, an appropriate adjustment of parameters in each step of the algorithm is implemented, through MIGRAD and/or SIMPLEX, as follows:

- MIGRAD: using as a starting value the minimizer, $\vec{x_{k-1}}$, obtained in the previous iteration, it searches for a minimizer, $\vec{x_k}$;
- MIGRAD and SIMPLEX: using as a starting value the minimizer, $\vec{x_{k-1}}$, obtained in the previous iteration, SIMPLEX first finds a minimizer, $\vec{x_{k,S}}$, and then MIGRAD uses $\vec{x_{k,S}}$ as a starting value to find the final minimizer, $\vec{x_{k,2}}$.

Among the two possible answers, $\vec{x_k}_{,1}$ and $\vec{x_k}_{,2}$, one can choose as minimizer, $\vec{x_k}$, i.e. the one which gives a lower value for the objective function. One could repeat either algorithm 1 or algorithm 2 (or other minimization procedures) with various starting points, $\vec{x_0}$, to find a global minimum more accurately. However, the combination of algorithms 1 and 2, described above, is adequate to obtain accurate values, while keeping the computational effort to a minimum.

Moreover, the optimality condition is checked at each iteration process whether the calculated value for the "estimated vertical distance to minimum[9]" exceeds a certain, previously fixed, tolerance parameter (its default value is set to be 0.1).

3.5.2 The Minimum χ^2 Method

The *standard χ^2 approach* is based on the minimization of the chi-squared function, as follows:

$$f_{\chi^2} = \sum_{i=1}^{N} \frac{(y_i - f(x_i))^2}{\sigma_i^2} \tag{3.28}$$

where y_i represent the set of the reconstructed quantities (i.e. TOF, p, E_k, A_1, A_2 and A_3) with the corresponding standard deviations σ_i, whereas the functions $f(x_i)$ are the expected values of the time of flight, momentum, kinetic energy and mass number; in detail, the latter are precisely the fit output parameters (T, P, K, A).

Therefore, replacing these data in the definition of f_{χ^2}, one can obtain the expression which has to be minimized[46]:

$$\begin{aligned} f_{\chi^2} = &\left(\frac{TOF - T}{\sigma_{TOF}}\right)^2 + \left(\frac{p - P}{\sigma_p}\right)^2 + \left(\frac{E_k - K}{\sigma_{E_k}}\right)^2 + \\ &+ (A_1 - A, \quad A_2 - A, \quad A_3 - A)(CC^T)^{-1} \begin{pmatrix} A_1 - A \\ A_2 - A \\ A_3 - A \end{pmatrix} \end{aligned} \tag{3.29}$$

with C the correlation matrix, which represents the link between the uncertainties associated to A_1, A_2 and A_3, as:

$$C = \begin{pmatrix} \frac{\partial A_1}{\partial T} dT & \frac{\partial A_1}{\partial P} dP & 0 \\ \frac{\partial A_2}{\partial T} dT & 0 & \frac{\partial A_2}{\partial K} dK \\ 0 & \frac{\partial A_3}{\partial P} dP & \frac{\partial A_3}{\partial K} dK \end{pmatrix} \tag{3.30}$$

In order to compute the correlation, it is necessary to start with an infinitesimal variation dy_i (for instance one can consider the TOF), which involves two variations in the corresponding parameters (A_1 and A_2 in this case), expressed by:

---

[9] More details are described in [60]

$$dA_1 = \frac{\partial A_1}{\partial T} dT \tag{3.31}$$

$$dA_2 = \frac{\partial A_2}{\partial T} dT \tag{3.32}$$

Then, the covariance of these two quantities, $cov(A_1, A_2)$, is obtained multiplying the previous relations (3.24) and (3.25); nevertheless, since these three mass number expressions depend two by two on one common measure (TOF or p or E_k), one has to take into account their correlations, thus it is more useful to get the (CC^T) covariance matrix[10], as:

$$CC^T =$$

$$= \begin{pmatrix} \left(\frac{\partial A_1}{\partial T} dT\right)^2 + \left(\frac{\partial A_1}{\partial P} dP\right)^2 & \frac{\partial A_1 \partial A_2}{\partial T^2} dT^2 & \frac{\partial A_1 \partial A_3}{\partial P^2} dP^2 \\ \frac{\partial A_2 \partial A_1}{\partial T^2} dT^2 & \left(\frac{\partial A_2}{\partial T} dT\right)^2 + \left(\frac{\partial A_2}{\partial K} dK\right)^2 & \frac{\partial A_2 \partial A_3}{\partial K^2} dK^2 \\ \frac{\partial A_3 \partial A_1}{\partial P^2} dP^2 & \frac{\partial A_3 \partial A_2}{\partial K^2} dK^2 & \left(\frac{\partial A_3}{\partial P} dP\right)^2 + \left(\frac{\partial A_3}{\partial K} dK\right)^2 \end{pmatrix} \tag{3.33}$$

The output parameters (T, P, K, A) can be considered as coordinates of a 4-dimensional space. Consequentially the point in this space, where the χ^2 function has a minimum, corresponds to the output set closest to the expected values. This occurs at the global minimum point of the 4-dimensional space of the parameters. Obviously some local minima in the function could be mistaken for the best fit, so it is important to make sure that the accurate minimum value has been retrieved. In the analysis framework, the ROOT MINUIT class is usually used in order to minimize the chi-squared function; each minimum in the parameters space has to be subjected to a decision algorithm procedure so that it can be accepted as a global minimum or rejected.

3.5.3 Fit Results

The results obtained with both the ALM and the standard χ^2 minimization are reported for some selected fragments of interest in *Figure 3.18* and *3.19* respectively.

---

[10] The (CC^T) covariance matrix is an invertible matrix as it is the product of two invertible matrices, in fact the transpose of an invertible matrix is also invertible.

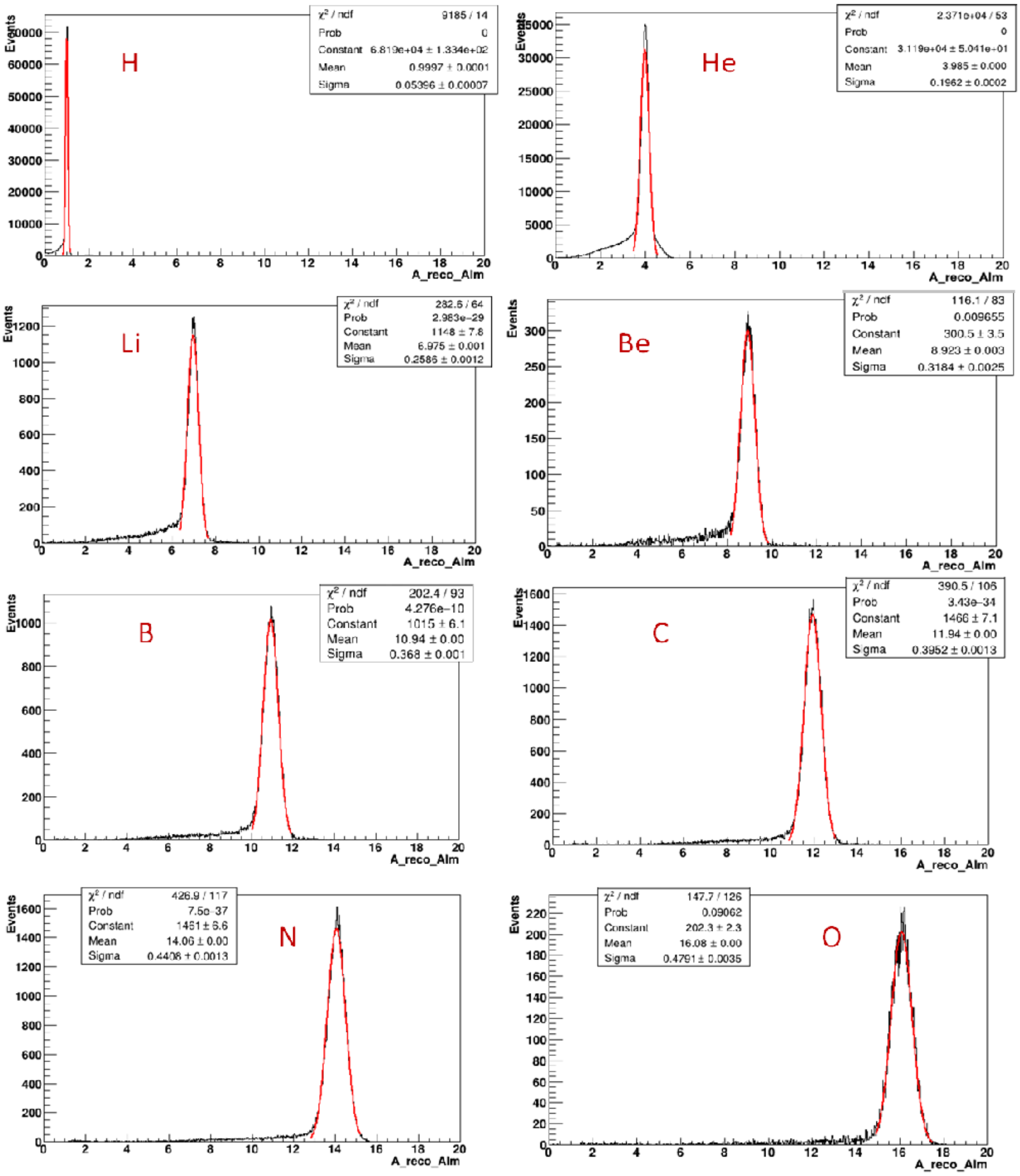

Figure 3.18: Reconstructed mass number A by means of the Augmented Lagrangian Method fit.

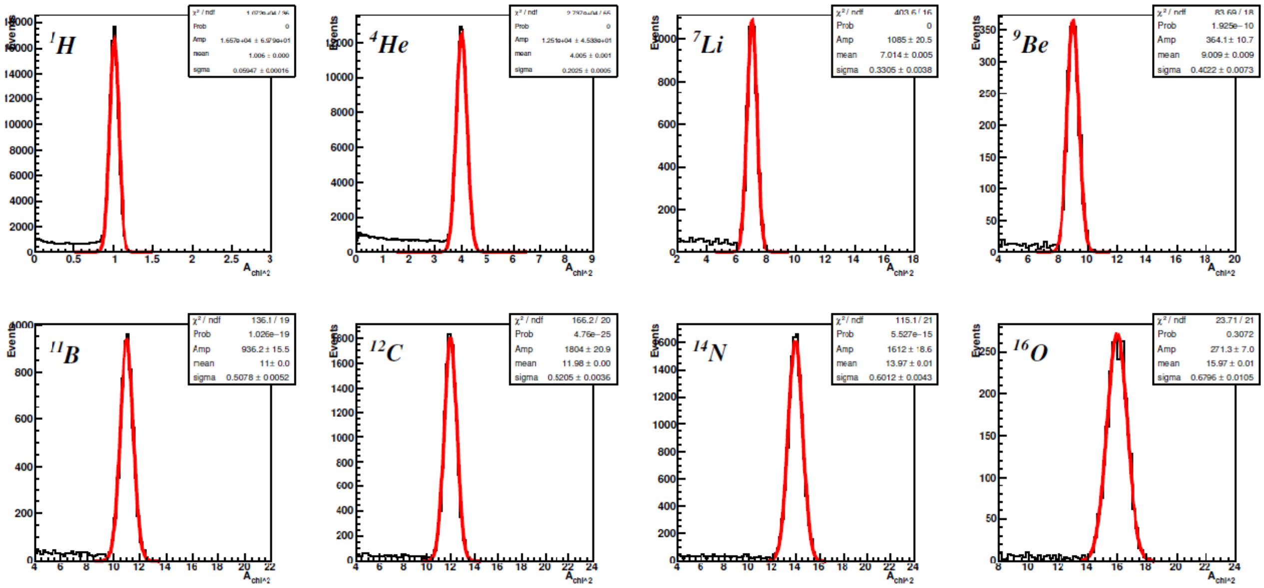

Figure 3.19: Reconstructed mass number A by means of the Standard χ^2 Method fit[46].

	^1H	^4He	^7Li	^9Be
A_{Alm}	1.0 ± 0.1	3.99 ± 0.16	6.98 ± 0.26	8.92 ± 0.32
A_{χ^2}	1.01 ± 0.06	4.01 ± 0.20	7.01 ± 0.33	9.01 ± 0.40
$\sigma(A_{Alm})[\%]$	5%	4%	3.7%	3.6%
$\sigma(A_{\chi^2})[\%]$	5.9%	5%	4.7%	4.4%

	^{11}B	^{12}C	^{14}N	^{16}O
A_{Alm}	10.94 ± 0.37	11.94 ± 0.40	14.06 ± 0.44	16.08 ± 0.48
A_{χ^2}	11.00 ± 0.51	11.98 ± 0.52	13.97 ± 0.60	15.97 ± 0.68
$\sigma(A_{Alm})[\%]$	3.4%	3.4%	3.1%	3%
$\sigma(A_{\chi^2})[\%]$	4.6%	4.3%	4.3%	4.3%

Table 3.4: Peak values and the related resolutions of the A_{Alm} and A_{χ^2} mass number from the ALM and χ^2 fit, respectively.

In *Table 3.4* the mean values and the corresponding fit Gaussian errors on A distribution, which has been reconstructed using the two fit method, previously described in Section 3.5.1 and 3.5.2. One can observe that the two fit give similar results and the resolution obtained for heavy fragments is about $3-4\%$, thus slightly better than the direct measurements A_1, A_2 and A_3, seen in Section 3.4.3. Nevertheless, as shown in *Figure 3.18* and *3.19*, the tails, due to, as already explained, fragments whose kinetic energy has been underestimated, therefore badly reconstructed events, are still visible.

In fact, it is possible to apply the χ^2 to these two fit methods in order to highlight some events related to its high values, as depicted in *Figure 3.20* (for istance, the

χ^2 applied to the A_{Alm} measurements of the ^{12}C), which represent the failure level of the fit.

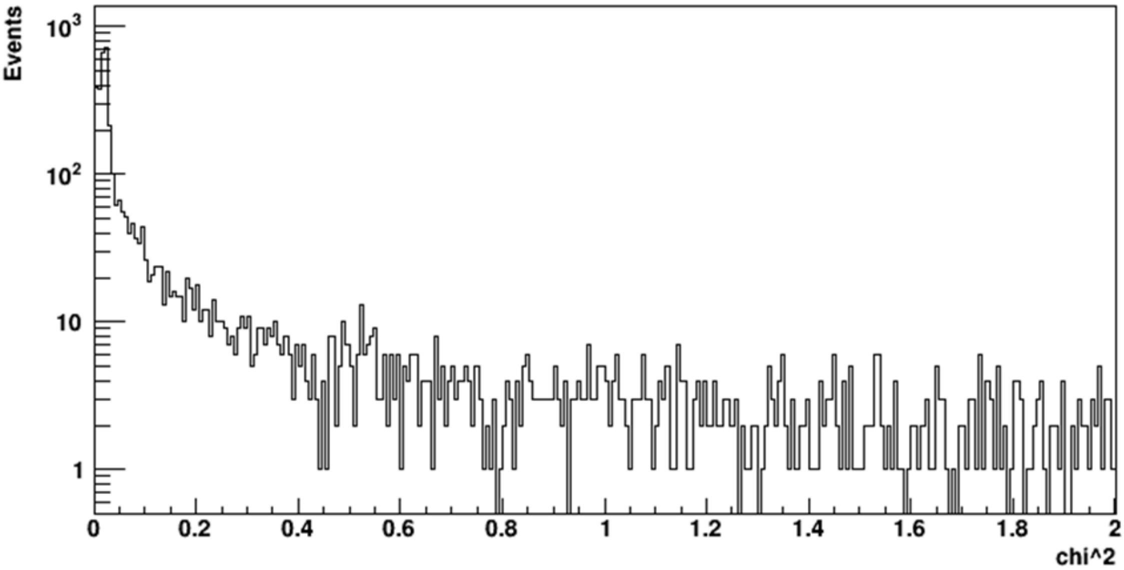

Figure 3.20: Example of the χ^2 distribution of the ALM fit for the ^{12}C.

To improve the relative resolution on A determination and reject the events with mass number value very different from the exspected one, a χ^2 cut can be useful, thus the application of a $\chi^2 < 5$ cut on both the standard χ^2 fit and the ALM fit allows to clean up the obtained distributions (*Fig.3.21* and *Fig.3.22*), while good statistics is preserved. This is particularly convenient when it is necessary to separate the different isotopes of the same element (*Fig.3.23*), as happens in the real experiment.

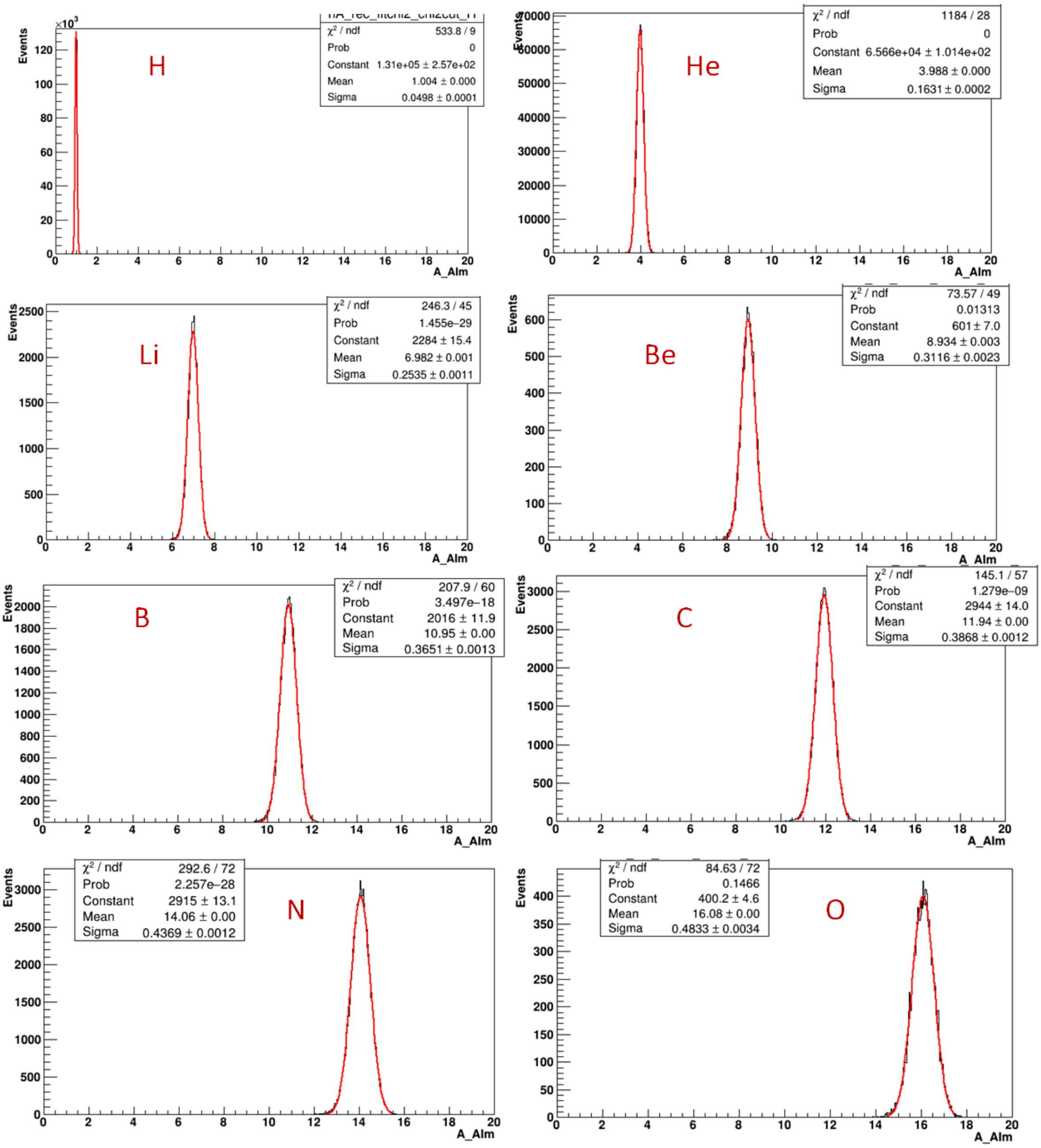

Figure 3.21: A^{cut}_{Alm} distributions for different isotopes, where a $\chi^2 < 5$ cut has been applied.

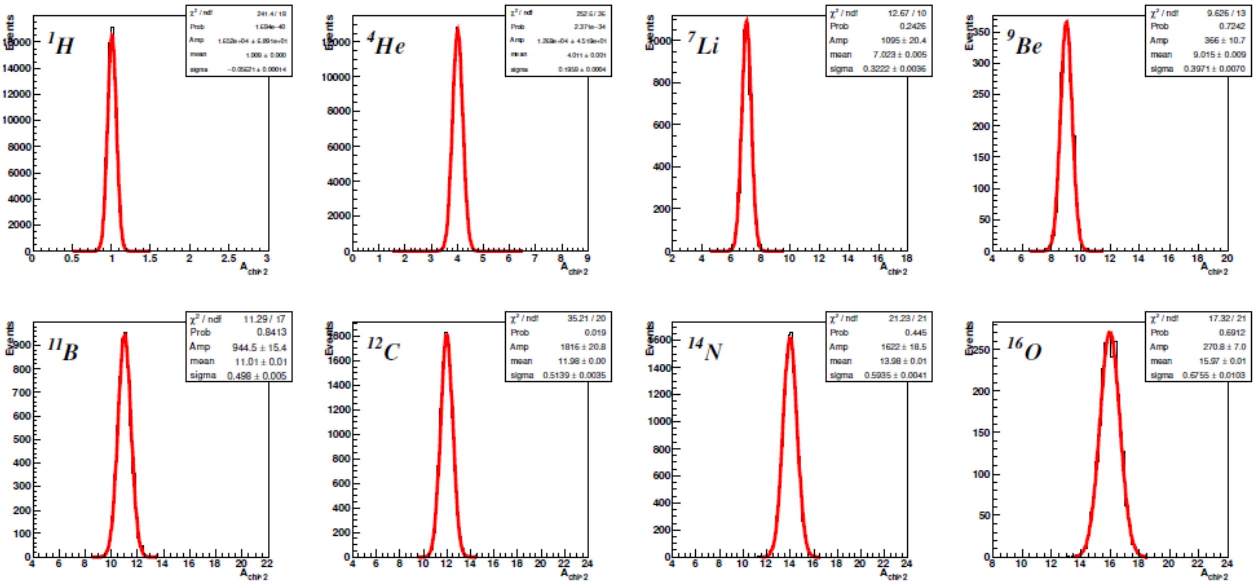

Figure 3.22: $A^{cut}_{\chi^2}$ distributions for different isotopes, where a $\chi^2 < 5$ cut has been applied[46].

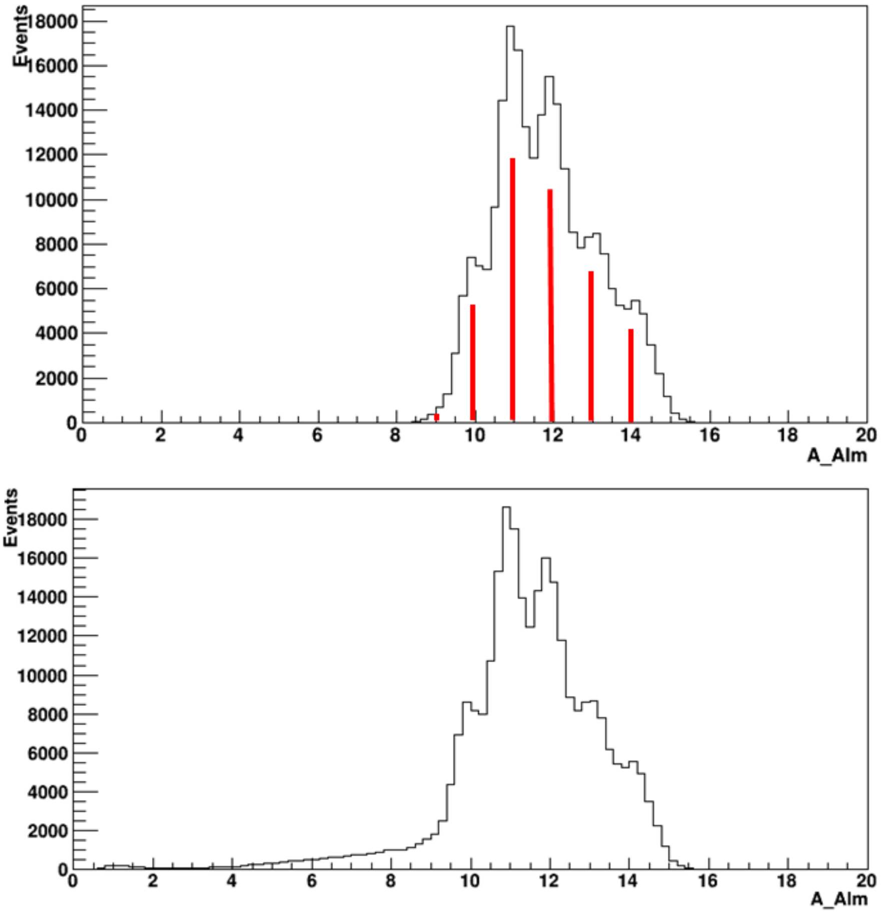

Figure 3.23: A_{Alm}^{cut} (top) for all the carbon isotopes (^9C, ^{10}C, ^{11}C, ^{12}C, ^{13}C, ^{14}C) produced by 200 MeV/n ^{16}O beam impinging on a polyethylene target and A_{Alm} (bottom), without the $\chi^2_{cut} < 5$, are depicted.

Summing up, in *Table 3.5*, the mean values and the corresponding errors, obtained by means of a Gaussian fit on the A_{χ^2} and A_{Alm} distributions with a $\chi^2_{cut} < 5$.

	^1H	^4He	^7Li	^9Be
A_{Alm}^{cut}	1.01 ± 0.05	3.99 ± 0.20	6.98 ± 0.25	8.9 ± 0.3
$A_{\chi^2}^{cut}$	1.01 ± 0.06	4.01 ± 0.20	7.02 ± 0.32	9.01 ± 0.40
$\sigma(A_{Alm}^{cut})[\%]$	5%	4%	3.7%	3.6%
$\sigma(A_{\chi^2}^{cut})[\%]$	5.9%	5%	4.7%	4.4%

	^{11}B	^{12}C	^{14}N	^{16}O
A^{cut}_{Alm}	10.95 ± 0.37	11.94 ± 0.39	14.06 ± 0.44	16.08 ± 0.48
$A^{cut}_{\chi^2}$	11.01 ± 0.50	11.98 ± 0.51	13.98 ± 0.59	15.97 ± 0.67
$\sigma(A^{cut}_{Alm})[\%]$	3.4%	3.4%	3.1%	3%
$\sigma(A^{cut}_{\chi^2})[\%]$	4.6%	4.3%	4.3%	4.3%

Table 3.5: Peak values and the related resolutions of the A^{cut}_{Alm} and $A^{cut}_{\chi^2}$ mass number from the ALM and χ^2 fit respectively, where a $\chi^2 < 5$ cut has been applied.

Conclusion

Main topic of this thesis is the identification of nuclear fragments produced in the fragmentations in the interactions of an incoming beam with at rest target. In particular, the beam and the target studied, are the ^{16}O and C_2H_4 that well simulate the interaction between a beam used in a hadrontherapy treatment with the human body. The results are obtained with simulated data applying the resolution of each part of the FOOT detector evaluated in various test beam.

The unequivocal way to identify a nuclear fragment is to measure its atomic and mass number. The charge has been evaluated measuring the time of flight and the energy loss of the fragments through the Bethe-Bloch formula. The performance obtained is a precision in the range: $2.7 - 5.5\%$, depending on the fragment, that allows a complete separation of the elements. About the number of mass identification, it has been implemented a direct method by means of relativistic formulas that allows three correlated ways of evaluation and, then two different fit approaches. All these different methods are possible because of the redundant subdetectors in the FOOT apparatus.

The two fit approaches show in general better results with respect to the direct one because they use all the FOOT subdetectors. In detail, the perfomance of the two fit is very similar; the improvement on the A resolution with a $\chi^2 < 5$ cut is negligible, however it allows to reject events that would increment the yields of background due to a wrong A value determination. The achievable resolution ranges between 3% and 4% for heavy ions, whereas for light fragments is about $5 - 6\%$, thus a better performance than the direct measurements. Moreover, through the fit tecniques, the kinetic quantities of the reconstructed fragments have been better estimated allowing a more accurate study of the kinematic of all the events which is essential for the differential cross sections measurements. These measurements are crucial in the hadrontherapy treatment because the fragments produced by nuclear interactions release different dose in the human body varying the foreseen biological effect, which implies a different RBE. Thus, it is necessary to include these effects in Treatment Planning System (TPS) in order to evaluate each risk factor.

In conclusion, the results show that the system is capable of reconstructing the charge and the mass number of heavy charged particles with acceptable accuracy ($\sim 3 - 4\%$), which matches with the resolutions required by radiobiologists. Nevertheless, some aspects of the analysis still need to be studied to further improve the identification of fragments, for istance the optimization of the reconstruction algorithms, the detectors performances, but most of all the total kinetic energy issue due to neutrons emission. In particular, to this purpose in future, an update of the FOOT detector can be planned: the evaluation of the neutron production together with the charged fragments can constrain even more strongly Monte Carlo nuclear production models that are relevant both for Particle Therapy and space radioprotection. Thus, different studies on providing neutron detection capability to the FOOT experiment are currently under investigation.

Bibliography

[1] https://enlight.web.cern.ch/what-is-hadron-therapy

[2] https://fondazionecnao.it/en/hadrontherapy/what-is-hadrontherapy

[3] William R. Leo *Techniques for Nuclear and Particle Physics Experiments*, 2nd ed. Springer-Verlag Berlin Heidelberg, 1994.

[4] Particle data group. Passage of particles through matter. 2009. : http://pdg.lbl.gov/2009/reviews/rpp2009-rev-passage-particles-matter.pdf.

[5] M. Testa. *Physical measurements for ion range verification in charged particle therapy.* Université Claude Bernar, 2010.

[6] M. J. Berger, M. Inokuti, H. H. Andersen, H. Bichsel, D. Powers, S . M. Seltzer, D . Thwaites, D. E. Watt. *Energy-loss Straggling*, Journal of the International Commission on Radiation Units and Measurements, Volume os25, Issue 2, 1993.

[7] L. Landau. *On the Energy Loss of Fast Particles by Ionization*, J. Phys. USSR 8 (1944) 201.

[8] Glenn F. Knoll. *Radiation Detection and Measurement*, Fourth Edition. John Wiley & Sons, Inc. (1989).

[9] Thilo Elsässer Dieter Schardt and Daniela Schulz-Ertner. *Heavy-ion tumor therapy: Physical and radiobiological benefits.* Rev. Mod. Phys, 82(383), 2010.

[10] Antony J. Lomax. *Charged particle therapy: the physics of interaction.* The cancer journal (Sudbury, Mass.), 2009.

[11] Highland V. L. 1975. *Some practical remarks on multiple scattering.* Nucl. Instrum. Meth., 129(2), 497–499.

[12] Dieter Schardt, Thilo Elsässer, and Daniela Schulz-Ertner. *Heavy-ion tumor therapy: Physical and radiobiological benefits.* Rev. Mod. Phys., 2010.

[13] Böhlen T. et al. 2010. *Benchmarking nuclear models of FLUKA and GEANT4 for carbon ion therapy.* Phys. Med. Biol., 55(19), 5833.

[14] M. Durante and H. Paganetti. *Nuclear Physics in Particle Therapy: a review.* In: Reports on Progress in Physics 79 (2016). Ed. by IOP Publishing.

[15] Harald Paganetti. *Proton Therapy Physics. Series in Medical Physics and Biomedical Engineering.* CRC Press, 2011.

[16] E. Haettner, H. Iwase, and D. Schardt. *Experimental fragmentation studies with 12C therapy beams*, Radiat. Prot. Dosim. 122 (2006) 485–487.

[17] Michael G. Stabin. *Radiation Protection and Dosimetry*, Springer-Verlag New York (2007).

[18] R.F.Laitano, *Fondamenti di dosimetria delle radiazioni ionizzanti-IV Edizione*, ENEA.

[19] A. C. Kraan. *Range Verification Methods in Particle Therapy: Underlying Physics and Monte Carlo Modeling.* In: Frontiers in Oncology 150.5 (2015).

[20] C K Ying et al. *Contributions of secondary fragmentation by carbon ion beams in water phantom: Monte Carlo simulation.* In: Journal of Physics: Conference Series 851 (May 2017).

[21] J. Hüfner, K. Schäfer, and B. Schürmann. *Abrasion-ablation in reactions between relativistic heavy ions.* In: Phys. Rev. C 12 (6 Dec. 1975), pp. 1888–1898.

[22] H. L. Bradt and B. Peters. *The Heavy Nuclei of the Primary Cosmic Radiation.* In: Phys. Rev. 77 (1 Jan. 1950), pp. 54–70.

[23] `https://geant4.web.cern.ch/node/1`

[24] V.N Ivanchenko. *Geant4 toolkit for simulation of HEP experiments Nuclear Instruments and Methods in Physics Research Section A: Accelerators, Spectrometers, Detectors and Associated Equipment.* Volume 502, Issues 2–3, 21 April 2003, Pages 666-668

[25] Daniel Cussol. *Nuclear Physics and Hadrontherapy.* LPC Caen, ENSICAEN, Université de Caen Basee-Normanide, IN2P3/CNRS, 2000.

[26] P. Dendy & B. Heaton, *Physics for Diagnostic Radiology*, 2nd Edition, 2012.

[27] Vincenzo Patera and Ilaria Mattei. *Nuclear interactions and medicine.* The European Physical Journal Plus, 2019.

[28] M- E. Lomax et al. *Biological Consequences of Radiation-induced DNA Damage: Relevance to Radiotherapy.* Clinical Oncology 25 (10 Oct. 2013).

[29] Ugo Amaldi and Gerhard Kraft. *Radiotherapy with beams of carbon ions.* Reports on Progress in Physics, 2005.

[30] Friedland W. et al. 1999. *Simulation of DNA fragment distributions after irradiation with photons.* Radiat. Environ. Bioph.

[31] Eric J. Hall and Amato J. Giaccia. *Introduction to Radiological Physics and Radiation Dosimetry.* Wiley-VCH, 2019.

[32] `https://doctorlib.info/oncology/basic-science-oncology/16.html`

[33] Mark Oldham. *Radiation physics and applications in therapeutic medicine.* Vol.36, Physics Education. William Beaumont Hospital, Royal Oak, Michigan, USA.

[34] ICRU, 2007, ICRU Report 78, *Prescribing, Recording and Reporting Proton Beam Therapy*, J. ICRU 7 (2).

[35] ICRP Publication 103, *The 2007 Recommendations of the International Commission on Radiological Protection.*

[36] J. S. Loeffler and M. Durante. *Charged particle therapy–optimization, challenges and future directions.* In: Nat Rev Clin Oncol 10 (7 May 2013).

[37] D. Shardt, T. Elsasser and D. Schulz-Ertner. *Reviews of Modern Physics*, Volume 82 (2010).

[38] ICRU. 2007. *Prescribing, Recording, and Reporting Proton-Beam Therapy* (Report 78).

[39] `https://eli-laser.eu/science-applications/hadron-therapy/`.

[40] T Pfuhl et al. *Dose build-up effects induced by delta electrons and target fragments in proton Bragg curves—measurements and simulations.* In: Physics in Medicine & Biology 63.17 (Aug. 2018).

[41] E.B. Podgorsak. *Radiation Oncology Physics: A Handbook for Teachers and Students*, INTERNATIONAL ATOMIC ENERGY AGENCY VIENNA, 2005.

[42] A.-L. Manninen. *Clinical applications of radiophotoluminescence (RPL) dosimetry in evaluation of patient radiation exposure in radiology : determination of absorbed and effective dose*, 2014.

[43] *Results of a Multicentric In Silico Clinical Trial (ROCOCO): Comparing Radiotherapy with Photons and Protons for Non-small Cell Lung Cancer* (2012). URL:`https://doi.org/10.1097/JTO.0b013e31823529fc`

[44] Marco Durante, Jay S Loeffler. *Charged particles in radiation oncology.* J. S. Nat. Rev. Clin. Oncol. 7, (2010).

[45] `https://www.researchgate.net/figure/Fig-1-Dose-response-curve-for-tumour-\control-probability-TCP-and-normal-tissue_fig1_336902812`.

[46] A. Alexandrov, G. Ambrosi, S. Argirò, G. Battistoni et al. *FOOT (CDR) Conceptual Design Report*, 2018.

[47] S. M. Valle. *Design, simulation and performances study of the FOOT experiment.* PhD Thesis. Università degli studi di Milano, 2019.

[48] S.M. Valle, A. Alexandrov et al. *FOOT: a new experiment to measure nuclear fragmentation at intermediate energies*, Prospectives in Science (2019) 12, 100415. Elsevier.

[49] G.Battistoni, M.Toppi et al. *Measuring the impact of Nuclear Interaction in Particle Therapy and in Radio Protection in Space: the FOOT experiment.*, submitted to Frontiers in Physics, section Medical Physics and Imaging.

[50] G. Silvestre. *Evaluation of double-sided silicon microstrip sensor for the FOOT experiment.* Nuclear Inst. and Methods in Physics Research, A 936 (2019) 36-38.

[51] https://www.crystals.saint-gobain.com/sites/imdf.crystals.com/files/documents/bgo-material-data-sheet.pdf

[52] R.Pleskac, Z. Abou-Haidar et al. *The FIRST experiment at GSI.* Research Section A: Accelerators, Spectrometers, Detectors and Associated Equipment Volume 678, 21 June 2012, Pages 130-138. https://doi.org/10.1016/j.nima.2012.02.020

[53] www.fluka.org

[54] Ferrari A. et al. 1992. *An improved multiple scattering model for charged particle transport.* Nucl. Instrum. Meth. B, 71(4), 412–426.

[55] Glauber R. J., Matthiae G. *High-energy scattering of protons by nuclei.* Nucl. Phys. B12, 135 (1970).

[56] Aichelin J. *Quantum molecular dynamics. a dynamical microscopic n-body approach to investigate fragment formation and the nuclear equation of state in heavy ion collisions.* Phys. Rep., 202.

[57] Gadioli E. and et al. *Boltzmann master equation theory of angular distributions in heavy-ion reactions.* Nuclear Physics, A643, 1998.

[58] F. Luoni, F. Horst et al. *Total nuclear reaction cross-section database for radiation protection in space and heavy-ion therapy applications*, 6 Sep. 2021. Url: https://arxiv.org/pdf/2105.11981.pdf.

[59] Toppi M. et al. *Measurements of 12C ion fragmentation on thin carbon target from the FIRST collaboration at GSI.* Journal of Physics: Conference Series, 590, 2015.

[60] Won Sang Cho,1a James S. Gainer et al. *OPTIMASS: A Package for the Minimization of Kinematic Mass Functions with Constraints*, 12 Jan 2016. DOI: 10.1007/JHEP01(2016)026.